

2017-02

# Magnetic Resonance Imaging of Demyelination and Remyelination in the Lysolecithin Model of Multiple Sclerosis

Dhaliwal, Raveena

---

Dhaliwal, R. (2017). Magnetic Resonance Imaging of Demyelination and Remyelination in the Lysolecithin Model of Multiple Sclerosis (Master's thesis, University of Calgary, Calgary, Canada). Retrieved from <https://prism.ucalgary.ca>. doi:10.11575/PRISM/26811

<http://hdl.handle.net/11023/3647>

*Downloaded from PRISM Repository, University of Calgary*

UNIVERSITY OF CALGARY

Magnetic Resonance Imaging of Demyelination and Remyelination in the  
Lysolecithin Model of Multiple Sclerosis

by

Raveena Dhaliwal

A THESIS

SUBMITTED TO THE FACULTY OF GRADUATE STUDIES  
IN PARTIAL FULFILMENT OF THE REQUIREMENTS FOR THE  
DEGREE OF MASTER OF SCIENCE

GRADUATE PROGRAM IN NEUROSCIENCE

CALGARY, ALBERTA

FEBRUARY, 2017

© Raveena Dhaliwal 2017

## Abstract

We require magnetic resonance imaging methods sensitive to remyelination for evaluation of remyelinating therapies for multiple sclerosis (MS). The goal of this thesis was to characterize the sensitivity of quantitative magnetization transfer (qMT) and diffusion tensor imaging (DTI) to myelin and axonal loss and remyelination in the lysolecithin model. This model is being used to develop remyelinating therapies for MS. We found that the qMT parameters of bound pool fraction ( $f$ ),  $T_1$  and several DTI parameters were able to detect demyelination in the lysolecithin model. The qMT parameters did not change with remyelination but several DTI parameters did recover slightly.  $f$  had the strongest correlation to the histological measure of myelin and  $T_1$  had the strongest correlation to the histological measure of axon content. Overall, the findings from this thesis support the inclusion of DTI and qMT as an outcome measure in future studies of potential MS therapeutics in the lysolecithin model.

## Acknowledgements

To begin, I would like to thank my supervisor, **Dr. Jeff Dunn**. This journey has been long and populated with unexpected twists, turns, and even some U-turns. Without the support and infrastructure provided by you and the **Dunn Lab Team**, it would not have been possible to reach the end. I thank you for your patience and understanding over these years of work.

I would also like to thank my co-supervisor, **Dr. V. Wee Yong**, for opening your lab to me. Thank you for allowing me to join in your lab meetings where I was able to learn a substantial amount about multiple sclerosis and neuroimmunology.

Thank you to my thesis committee members, **Drs. Shalina Ousman and Bruce Pike**, for your support and guidance. I appreciate the thoughtful advice and insights you gave to me.

Thank you to my internal examiner, **Dr. Catherine Lebel**, for taking the time to serve as an examiner for my thesis defense.

I would like to thank the **Dunn Lab** – for the fun times. Especially thank you to **Dr. Ying Wu** for always being available when I needed assistance.

I would also like to thank the **Yong Lab** for their support. I would specifically like to thank **Michael Keough** and **Sam Jensen** for taking time out of their busy schedule to perform lysolecithin surgeries for this thesis. I would also like to thank **Khalil Rawji** for always being available to answer my endless questions.

Thank you to **Dave Rushforth** and **Tad Foniok** for your sharing your expertise with me.

I would like to thank **Gary Dobko, Julie Tran, Leanne Robichaud, Sultana Majid, Shefali Pandey and Diane Dleikan**, for always believing in me even when I did not believe in myself.

Last, but not least, I would like to thank **my large and crazy family**. Thank you to my parents, **Mark and Gurdeep Dhaliwal**, for your love. Thank you to my older brother, **Raj Dhaliwal**, for making me who I am today. Finally, thank you to my sisters, **Anita Kalia Assi, Menca Kalia, and Arvind Dhaliwal**, for keeping me sane – mostly.

## **Dedication**

*To my wonderful family and friends—for your faith, support  
and unfaltering love.*

## Table of Contents

Abstract .....	ii
Acknowledgements .....	iii
Dedication .....	v
Table of Contents.....	vi
List of Tables .....	ix
List of Figures and Illustrations .....	x
List of Abbreviations.....	xii
CHAPTER ONE: INTRODUCTION.....	1
1.1 Multiple Sclerosis: General Overview .....	1
1.2 Magnetic Resonance Imaging .....	3
1.2.1 Physics of Magnetic Resonance Imaging .....	4
1.2.1.1 Nuclear Magnetic Resonance.....	4
1.2.1.2 Relaxation .....	6
1.2.1.3 Spin Echo vs. Gradient Echo .....	7
1.2.1.4 Quantitative Magnetization Transfer Imaging .....	8
1.2.1.5 Diffusion Tensor Imaging.....	11
1.2.1.6 Parameters affecting MR Signal.....	15
1.3 Multiple Sclerosis: Pathophysiology .....	16
1.3.1 Pathogenesis of Multiple Sclerosis.....	16
1.3.2 Multiple Sclerosis Lesions .....	18
1.3.2.1 White Matter Lesions.....	18
1.3.2.2 Gray Matter Lesions.....	21
1.3.3 Glial and Neuronal Damage.....	21
1.3.3.1 White Matter .....	21
1.3.3.2 Gray Matter .....	23
1.3.4 Remyelination .....	24
1.3.5 Multiple Sclerosis: Treatments .....	25
1.3.5.1 Current Treatments .....	25
1.3.5.2 Developing Treatments.....	26
1.4 Magnetic Resonance Imaging of Demyelination and Remyelination .....	27
1.5 Multiple Sclerosis: Animal Models .....	31
1.5.1 Experimental Autoimmune Encephalomyelitis .....	31
1.5.2 Theiler's Murine Encephalomyelitis Virus .....	33
1.5.3 Cuprizone.....	34
1.5.4 Ethidium Bromide .....	36
1.5.5 Lysolecithin .....	36
1.6 <i>Ex Vivo</i> Magnetic Resonance Imaging .....	38
CHAPTER TWO: OBJECTIVES.....	40
2.1 Introduction to Objectives .....	40
2.2 Aim 1: .....	41
2.2.1 Hypothesis: .....	41

2.3 Aim 2: .....	41
2.3.1 Hypothesis: .....	41
CHAPTER THREE: MATERIALS AND METHODS .....	42
3.1 Study Design Summary .....	42
3.1.1 Aim 1 .....	42
3.1.2 Aim 2 .....	42
3.2 Detailed Materials and Methods .....	43
3.2.1 Lysolecithin Induced Demyelination .....	43
3.2.2 Tissue Fixation and Preparation for Imaging .....	44
3.2.3 MRI Acquisition .....	44
3.2.4 MRI Data Analysis .....	46
3.2.4.1 $T_1$ .....	46
3.2.4.2 Quantitative Magnetization Transfer .....	46
3.2.4.3 Diffusion Tensor Imaging .....	47
3.2.4.4 Statistics .....	50
3.2.5 Histology .....	50
3.2.5.1 Sectioning and Staining .....	50
3.2.5.2 Co-Registration .....	51
3.2.5.3 Analysis .....	53
3.2.5.4 Statistics .....	55
CHAPTER FOUR: DEVELOPMENT OF QUANTITATIVE MAGNETIZATION TRANSFER SEQUENCE AND ANALYSIS .....	56
4.1 Results .....	56
4.1.1 Quantitative Magnetization Transfer Parameters can be Calculated using the Volume Coil or Cryoprobe .....	56
4.1.2 Quantitative Magnetization Transfer of Lysolecithin Lesions using the Cryoprobe or Volume Coil .....	58
4.2 Discussion .....	63
4.2.1 Validation of the Quantitative Magnetization Transfer Sequence .....	63
4.3 Conclusions .....	64
CHAPTER FIVE: $T_1$ AND QUANTITATIVE MAGNETIZATION TRANSFER IMAGING PARAMETERS CORRELATE WITH HISTOLOGICAL STAINS FOR MYELIN AND NEUROFILAMENT .....	65
Results .....	65
5.1.1 Quantitative Magnetization Transfer Parameters and $T_1$ of Lysolecithin Lesions .....	65
5.1.2 Quantification of Histological Stains for Myelin and Neurofilament .....	70
5.1.3 Correlations between Histological Staining .....	74
5.1.4 Quantitative Magnetization Transfer Parameters correlate with Histological Stains for Myelin and Neurofilament .....	76
5.2 Discussion .....	83
5.2.1 $T_1$ and Quantitative Magnetization Transfer of Lysolecithin Lesions .....	83

5.2.2 Histology.....	84
5.2.3 Correlations between Histological Stains .....	85
5.2.4 Correlations between quantitative Magnetization transfer and Histology .....	85
5.3 Conclusions .....	86
<b>CHAPTER SIX: DIFFUSION TENSOR IMAGING PARAMETERS CORRELATE WITH HISTOLOGICAL STAINS FOR MYELIN AND NEUROFILAMENT .....</b>	<b>87</b>
6.1 Results.....	87
6.1.1 Diffusion Tensor Imaging Parameters in Lysolecithin Lesions.....	87
6.1.2 Diffusion Tensor Imaging Parameters correlate with histological stains for MBP and neurofilament.....	97
6.2 Discussion .....	101
6.2.1 Diffusion Tensor Imaging parameters of Lysolecithin Lesions .....	101
6.2.2 Diffusion Tensor Imaging and Histology Correlations .....	103
6.3 Conclusions .....	104
<b>CHAPTER SEVEN: CORRELATIONS BETWEEN MR IMAGING PARAMETERS</b>	<b>105</b>
7.1 Results.....	105
7.1.1 Correlations between Quantitative Magnetization Transfer and Diffusion Tensor Imaging parameters.....	105
7.2 Discussion .....	105
7.3 Conclusions .....	104
<b>CHAPTER EIGHT: GENERAL DISCUSSION .....</b>	<b>105</b>
8.1 Introduction .....	105
8.2 Summary of Finding and Discussion .....	105
8.3 Limitations of the Study .....	108
8.4 Significance of Findings .....	111
<b>CHAPTER NINE: CONCLUSIONS AND FUTURE DIRECTIONS.....</b>	<b>112</b>
9.1 Future Directions .....	112
9.2 Conclusions .....	114
<b>REFERENCES .....</b>	<b>115</b>
<b>APPENDIX A: COPYRIGHT PERMISSIONS.....</b>	<b>132</b>

## **List of Tables**

Table 4.1: Quantitative Magnetization Transfer parameters of agar gel phantoms.....	57
Table 4.2: The signal to noise ratio of volume and cryoprobe images.....	59
Table 5.1: Correlations between histological measures of myelin and axons. ....	74
Table 6.1: Correlations between DTI parameters and histological stains. ....	98
Table 7.1: Correlations between DTI parameters and qMT parameters.....	105

## List of Figures and Illustrations

Figure 1.1: The two-pool model of magnetization transfer.....	10
Figure 1.2: Representative Diffusion ellipsoids. ....	14
Figure 3.5: Schematic illustration of MR and microscopy co-registration method. ....	52
Figure 3.5: Illustration of method used to find percent MBP staining and percent SMI312 staining. ....	54
Figure 4.1: Representative FLASH-Scout images with corresponding $T_1$ maps and bound pool fraction (f) maps for the volume coil and cryoprobe. ....	60
Figure 4.2: $T_1$ and bound pool fraction at the lesion and contralateral sites. ....	61
Figure 4.3: $T_2$ of Liquid and bound pools at the lesion and contralateral sites. ....	62
Figure 5.1: $T_1$ and bound pool fraction (f) of naïve (n=5), contralateral regions (7dpi n=7; 14 dpi n=7), 7 dpi lesion (n=7) and 14 dpi lesions (n=7). ....	67
Figure 5.4: Myelin basic protein (MBP) and SMI-312 staining for naïve, 7 dpi and 14 dpi of lysolecithin. ....	72
Figure 5.5: Quantification of myelin basic protein (MBP) and SMI312 staining of naïve (n=5), contralateral regions (7 dpi n=5; 14 dpi n=7), 7 dpi lesion (n=7) and 14 dpi lesions (n=7).....	73
Figure 5.6: Scatterplots and best-fit lines of MBP and SMI312 staining. ....	75
Table 5.2: correlations between quantitative Magnetization Transfer parameters and histology. ....	77
Figure 5.7: Scatterplots and best fit lines of bound pool fraction and quantification of histological stains. ....	79
Figure 5.8: Scatterplots and best-fit lines of $T_1$ and quantification of histological stains. ....	81
Figure 5.9: Scatterplots and best-fit lines of normalized percent SMI312 staining and qMT parameters. ....	82
Figure 6.1: B=0 Echo planar images of Naïve, 7 dpi, and 14 dpi lesions. ....	90
Figure 6.2: Fractional Anisotropy (FA) of naïve (n=4), 7 dpi (n= 5) and 14 dpi (n=7) contralateral regions, 7 dpi (n=5) lesions and 14 dpi (n=7) lesions. ....	91

Figure 6.3: Normalized fractional anisotropy (FA) of naïve (n=4), 7 (n=5) and 14 (n=7) dpi lesions. ....	92
Figure 6.4: Radial diffusion, axial diffusion, and mean diffusion of naïve (n=3), 7 dpi (n=7) and 14 dpi (n=5) contralateral regions, 7 dpi lesions (n=7) and 14 dpi lesions (n=5). ....	93
Figure 6.5. Normalized axial diffusion, radial diffusion and mean diffusion of naïve (n=4) and 7 (n=5) and 14 (n=7) dpi lesions. ....	94
Figure 6.6: Linear Anisotropy (CL), Planar Anisotropy (CP), Spherical Anisotropy (CS), Relative Anisotropy and volume ratio (VR) of naïve (n=4), contralateral regions (7 dpi n=5; 14 dpi n=7), 7 dpi (n=5) and 14 dpi (n=7) lesions. ....	95
Figure 6.7: Normalized Linear Anisotropy (CL), Planar Anisotropy (CP), Spherical Anisotropy (CS), Relative Anisotropy (RA) and the volume ratio (VR) of naïve (n=4) and 7 dpi (n=5) and 14 dpi (n=7) lesions. ....	96
Figure 6.8: Scatterplots and best-fit lines of DTI parameters and quantification of histological stains. ....	100

## List of Abbreviations

AD	Axial Diffusivity
ADC	Apparent Diffusion Coefficient
ANOVA	Analysis of Variance
APCs	Antigen Presenting Cells
$B_0$	Static Magnetic Field
CIS	Clinically Isolated Syndrome
CL	Linear Case or Linear Anisotropy
CNS	Central Nervous System
CP	Planar Case or Planar Anisotropy
CS	Spherical Case or Spherical Anisotropy
CSF	Cerebral Spinal Fluid
D	Diffusion Coefficient
$\underline{D}$	The Effective Diffusion Tensor
DIS	Dissemination in Space
DIT	Dissemination in Time
DMTs	Disease Modifying Therapies
Dpi	Days Post Injection
DTI	Diffusion Tensor Imaging
EAE	Experimental Autoimmune Encephalomyelitis
EPI	Echo-Planar Imaging
f	Bound Pool Fraction
FA	Fractional Anisotropy
FID	Free Induction Decay
FLASH	Fast Low Angle Shot
FOV	Field of View
GM	Gray Matter
Igs	Immunoglobulins

M <sub>0</sub>	Net Magnetization Vector
MAG	Myelin-Associated Glycoprotein
MBP	Myelin Basic Protein
MD	Mean Diffusivity
MOG	Myelin Oligodendrocyte Glycoprotein
MRI	Magnetic Resonance Imaging
MS	Multiple Sclerosis
MT	Magnetization Transfer
MTR	Magnetization Transfer Ratio
NAWM	Normal Appearing White Matter
NEX	Number of Excitations
NMR	Nuclear Magnetic Resonance
OPCs	Oligodendrocyte Precursor Cells
PBS	Phosphate Buffered Saline
PFA	Paraformaldehyde
PLP	Proteolipid Protein
PPMS	Primary Progressive Multiple Sclerosis
qMT	quantitative Magnetization Transfer
R <sub>1</sub>	Longitudinal Relaxation Rate
R <sub>1A</sub>	Longitudinal Relaxation Rate of Liquid Pool
R <sub>1B</sub>	Longitudinal Relaxation Rate of Bound Pool
R <sub>2</sub>	Transverse Relaxation Rate
RA	Relative Anisotropy
RARE	Rapid Acquisition with Relaxation Enhancement
RD	Radial Diffusivity
RF	Radio Frequency
RRMS	Relapsing Remitting Multiple Sclerosis
SD	Standard Deviation

SMI312	Anti-Neurofilament Antibody
SNR	Signal to Noise Ratio
SPMS	Secondary Progressive Multiple Sclerosis
T <sub>1</sub>	Longitudinal Relaxation Time
T <sub>2</sub>	Transverse Relaxation Time
T <sub>2</sub> <sup>A</sup>	Transverse Relaxation Time of Liquid Pool
T <sub>2</sub> <sup>B</sup>	Transverse Relaxation Time of Bound Pool
TE	Time to Echo
TMEV	Theiler's Murine Encephalomyelitis Virus
TR	Time to Repeat
VR	Volume Ratio
VTR	Variable Time to Repeat
WM	White Matter

## **Chapter One: Introduction**

### **1.1 Multiple Sclerosis: General Overview**

In the 1800's the founder of modern neurology, Jean-Martin Charcot, described a condition that occurred in young adults causing tremor, paralysis, and gray patches in the central nervous system (CNS). He called this condition sclérose en plaque disseminé (Murray, 2004). This was the start of the approximately 150-year journey that has led to our current understanding of the disease we now call Multiple Sclerosis (MS) (Murray, 2004); a chronic inflammatory, demyelinating and degenerative disease of the CNS (Goldenberg, 2012).

Canada has one of the highest prevalence of MS in the world with an estimated 1 in 300 Albertan's living with the disease (Beck et al., 2005). The demographic at greatest risk for MS are young adults between 20-45 years of age with women being twice as likely to develop the disease compared to men (Goldenberg, 2012). MS occurs early in life and can rapidly result in disability (Patwardhan et al., 2005). Thus the rates of unemployment in MS are high and have been reported to be between 56-80% (LaRocca et al., 1982; Kornblith et al., 1986; Julian et al., 2008; Strober and Arnett, 2015). This loss of productivity along with other indirect and direct costs (for example, hospitalization) cause a significant economic burden on society. In 1995, the lifetime cost of MS was estimated to be over 1 million dollars per patient (1998).

When Charcot first described the illness, he noted nystagmus (dancing eye), intention tremor and ataxic dysarthria (scanning speech) (Murray, 2004). These symptoms became known as Charcot's triad and were used for many years to diagnose MS. Today, the diagnostic criteria, known as the McDonald Criteria, is based on clinical examination and magnetic resonance imaging (MRI) scans (Joanna et al., 2015).

There is considerable heterogeneity in the MS disease course. We classify MS into four main types: relapsing-remitting MS (RRMS), secondary progressive MS (SPMS), primary progressive MS (PPMS) and progressive relapsing MS (McDonald et al., 2001; Dalton et al., 2002; Joanna et al., 2015)

RRMS is characterized by periods of neurological deficits lasting at least 24 hours, where a patient reports worsening of symptoms and objectively visible signs indicative of acute inflammatory, demyelinating events in the CNS without the presence of fever and infection (Joanna et al., 2015). The symptoms that may occur during these relapses include sensory disturbances in the limbs, ataxia, and optic nerve dysfunction (Goodin et al., 2002). These periods, called relapses, are followed by periods, called remission, where symptoms lessen. Over time as relapses and remission progress, deficits begin to build due to incomplete recovery (Joanna et al., 2015).

Using the revised McDonald criteria (2010), the presence of one relapse accompanied with two or more T2-weighted lesions on an MRI scan that are disseminated in time and space (DIT and DIS, respectively) is sufficient to diagnose a patient with RRMS. DIS means the presence of lesions in two of the four typical MS regions of the CNS. These four areas include the periventricular region, juxtacortical region, infratentorial region, and the spinal cord. DIT can be characterized by either new lesions on a follow-up MRI or the simultaneous presence of T1-weighted lesions that the MRI contrast agent gadolinium enhances and does not enhance (Polman et al., 2011).

Approximately 75% of patients that present with RRMS will transition into SPMS within 15 years of initial diagnoses (Scalfari et al., 2012). Progressive and irreversible neurodegeneration characterize this form of MS (Goldenberg, 2012).

In PPMS, progression occurs from the onset of the disease without identifiable acute relapses, which leads to rapid neurological decline and disability. PPMS affects ~15% of total MS patients, does not have a clear female bias, and has a delayed onset compared to RRMS (Ebers, 2004; Tur and

Thompson, 2015). A patient can be diagnosed with PPMS if they present with one year of disease progression and two of the following three criteria. These criteria include lesions with DIS in the brain, lesions with DIS in the spinal cord, or CSF with elevated levels of the antibody, Immunoglobulin G (IgG) (Polman et al., 2011).

Finally, the progressive relapsing form is rare, affecting less than 5% of patients. This type of MS is similar to PPMS, the difference being that patients have relapses similar to those seen in RRMS along with their progression (Goldenberg, 2012).

Another important classification to be familiar with when discussing MS is clinically isolated syndrome (CIS). CIS is an acute or subacute episode of neurological disturbance due to a single white-matter lesion (Miller et al., 2005). Since no second episode has yet occurred, patients with CIS cannot be diagnosed with clinically definite MS. However, 85% of patients with CIS will eventually transition into having clinically definite MS (Miller et al., 2005).

MRI plays a critical role in our ability to identify and monitor MS disease progression. MRI methods are continually developing and can improve our capacity to diagnose MS, to examine the efficacy of treatments and provide us with a better understanding of MS pathology. It is critical that we test these developing techniques in animal models to demonstrate their sensitivity and specificity to the different types of pathology present in MS (Nathoo et al., 2014a, b).

## **1.2 Magnetic Resonance Imaging**

Since its first use in an MS patient the 1980s (Young et al., 1981) magnetic resonance imaging (MRI) has had a significant impact on our understanding of MS pathology and treatments by allowing non-invasive exploration of the disease. Conventional and novel MR techniques are currently

used to aid in the diagnosis of MS, help evaluate new MS treatments in clinical trials and follow patients clinically (Klawiter, 2013). Below we discuss the core principles of MRI and the role that several MRI techniques play in the field of MS.

### ***1.2.1 Physics of Magnetic Resonance Imaging***

#### **1.2.1.1 Nuclear Magnetic Resonance**

In 1946 two research experiments independently demonstrated the basic physics of nuclear magnetic resonance (NMR), the origin of MRI (Bloch, 1946; Purcell et al., 1946; Plewes and Kucharczyk, 2012). The fundamental principle behind NMR is that nuclei which contain an odd number of neutrons and protons have a property known as spin (Plewes and Kucharczyk, 2012). Due to its abundance in the body in the form of water and fat the hydrogen nucleus with one proton ( $^1\text{H}$ ) is the most commonly used atom in MR imaging. Other nuclei that are sometimes studied include sodium ( $^{23}\text{Na}$ ), phosphorous ( $^{31}\text{P}$ ), oxygen ( $^{17}\text{O}$ ), and fluorine ( $^{19}\text{F}$ ) (Plewes and Kucharczyk, 2012). From here on, we will be discussing primarily  $^1\text{H}$  for the sake of simplicity.

The spin of a nuclei is an intrinsic property of the nuclei, similar to mass or charge. This spin can be thought of as the nucleus rotating about some axis (Plewes and Kucharczyk, 2012). Due to the laws of electromagnetic induction, a moving unbalanced charge induces a magnetic field around itself. Therefore the charge and spin together give a proton properties similar to a bar magnet (Westbrook, 2015). Normally the magnetic moments, an arrow denoting the direction and size of the magnetic field, are randomly oriented. When placed in an applied magnetic field ( $B_0$ ), the magnetic moments of a nucleus will tend to align with the applied field (Westbrook, 2015) .

Due to their spin, nuclei do not perfectly align with the applied magnetic field (Westbrook, 2015). Rather they spin around the main axis of the net magnetic field in a process that is known as precession.

The precessional frequency of a nucleus, also known as the Larmor frequency ( $\omega$ ), can be calculated using the Larmor equation below (Westbrook, 2015):

$$\omega = \gamma B_0$$

$B_0$  is the strength of the externally applied magnetic field, and  $\gamma$  is the gyromagnetic ratio of the nuclei. The gyromagnetic ratio ( $\gamma$ ) is the ratio of the magnetic and angular moment of the nuclei at 1T. This constant is 42.57Mhz/Tesla for hydrogen (Westbrook, 2015).

One can think of the spins of individual protons as vectors that add to form the net magnetization vector ( $M_0$ ) (Westbrook, 2015). Typically, the magnetic moments of nuclei are randomly oriented. The magnetic moment is represented by an arrow denoting the direction and size of the magnetic field. This random orientation results in a net magnetization vector with a magnitude of 0. When placed in an static magnetic field ( $B_0$ ), the magnetic moments of a nucleus will tend to align with the applied field (Westbrook, 2015). This application of  $B_0$  leads to a net magnetization vector in the direction of the  $B_0$  (z direction). However as long as the net magnetization vector aligns with the magnetic field it cannot be measured (Plewes and Kucharczyk, 2012).

By applying a radio frequency (RF) pulse, at the same frequency of proton precession (the Larmor frequency), we can excite proton spins through resonance. Resonance is the energy transition that occurs when an object is subjected to a frequency the same as its own (Westbrook, 2015). In the case of protons, resonance causes the  $M_0$  to "flip" out of alignment with  $B_0$  and begin precessing in the xy-plane. This precession is seen in the net magnetic vector because the RF pulse causes a small number of individual spins to precess in alignment (in-phase). Once the RF pulse is switched off the precessing magnetization in the xy-plane is detected by receiver coils, where it induces a

current. The signal received by this coil is called the free induction decay (FID) (Westbrook, 2015).

Once energy is no longer entering the system, the protons will emit the energy received from the RF pulse and return to their original state, a process known as relaxation (Westbrook, 2015). Protons in different tissues have different rates of relaxation. Different rates of relaxation, varying proton concentrations and proton diffusion characteristics in tissues provide opportunities to obtain image contrast in MRI.

In addition to the above basic concepts, it is important to know that MRI signal localization occurs via spatial encoding. This encoding is carried out by gradient coils that vary the magnetic field linearly in three orthogonal directions (x, y, z). There are good reviews such as (Plewes and Kucharczyk, 2012) and (Hornak, 1996) which explain these concepts in more depth.

#### 1.2.1.2 Relaxation

As mentioned above, once the RF pulse is turned off relaxation of the protons occurs. This relaxation has two components: longitudinal and transverse. These two components are independent of one another although transverse relaxation is always the faster of the two (Plewes and Kucharczyk, 2012; Westbrook, 2015).

Longitudinal relaxation is the return of the net magnetization vector from the xy-plane to alignment with  $B_0$  (Westbrook, 2015). The time constant that describes longitudinal relaxation is called the spin-lattice relaxation time ( $T_1$ ). The  $T_1$  relaxation time is the time it takes for recovery of 63% of the net longitudinal magnetization ( $M_0$ ). The  $T_1$  is different for different tissues and therefore provides a type of contrast in MR imaging (Hornak, 1996). More specifically, tissue that can efficiently transfer energy to its surrounding will have a shorter  $T_1$  than tissue that cannot. For example, tissue with a high fat content, such as myelin,

would be expected to have shorter  $T_1$  than tissue with a lower fat content, such as a demyelinated lesion.

Transverse relaxation is the process by which individual spins dephase (Westbrook, 2015). This relaxation happens because packets of individual spins experience slightly different magnetic fields and rotate at slightly different frequencies. This variation in magnetic fields will cause the transverse component of the net magnetization vector to drop to 0.  $T_2$  is the time it takes for the signal to decrease to 37% of its initial value (Westbrook, 2015). Tissue that can undergo efficient energy exchange with itself, such as lipids, has a shorter  $T_2$  than tissue that cannot, such as cerebral spinal fluid (CSF).

We can also consider the rate of longitudinal ( $R_1$ ) and transverse relaxation ( $R_2$ ). These are the inverse of  $T_1$  and  $T_2$  respectively.

#### 1.2.1.3 Spin Echo vs. Gradient Echo

Gradient and spin echo sequences are commonly used to generate MR images. In a spin echo pulse sequence, there is a  $90^\circ$  RF pulse followed by an  $180^\circ$  RF pulse (Westbrook, 2015). As discussed above, spins lose coherence or dephase due to spin-spin relaxation after the initial RF pulse. One can think of this dephasing as a fan where some spins lag behind others. By using a  $180^\circ$  refocusing pulse, we can "flip" the spins or the fan such that the fast spins are now behind the slow spins. This flipping of spins allows the quick spins to catch up with the slow spins thus increasing coherence and regenerating some of the lost signal. This regenerated signal is called an echo (Westbrook, 2015).

In contrast to spin echo sequences, gradient echo pulse sequences use a gradient to refocus spins instead of an  $180^\circ$  pulse. The lack of an  $180^\circ$  pulse allows for faster image acquisition than a spin echo sequence. However gradient refocusing is less efficient than RF refocusing, therefore, increased speed comes at the cost of a decrease in signal to noise (Westbrook, 2015).

#### 1.2.1.4 Quantitative Magnetization Transfer Imaging

The transverse relaxation of protons bound to macromolecules (bound pool) occurs so quickly ( $\sim 10\mu\text{s}$ ) that it is not detectable by conventional MRI. However, we can apply an RF saturation pulse at a frequency that will excite these protons but not protons in water (exciting the bound vs. free or liquid pool). Following this excitation, the bound pool will transfer its magnetization to the liquid pool resulting in a signal loss on MRI images (Henkelman et al., 1993). The magnetization transfer ratio (MTR) provides an estimate of this exchange process. By obtaining two images, one with a saturation pulse (MT image) and one without a saturation pulse we can calculate MTR. This calculation is done by subtracting the MT image from the control and dividing by the control image (Pagani et al., 2008).

However, the MTR is affected by several factors including the amount of bound protons and the rate of magnetization exchange. A quantitative magnetization transfer (qMT) analysis can be used to tease apart these variables. This method involves modeling the magnetization transfer exchange system.

One model of the magnetization transfer system is known as the two pool model. As the name suggests this model consists of two pools (**Figure 1.1**). Pool A is the liquid proton pool and pool B corresponds to the bound (or semisolid) protons. Each pool has a rate ( $R_a$  or  $R_b$ ) that is the inverse of  $T_1$  and governs the recovery of longitudinal magnetization. The rate of longitudinal magnetization loss due to the off-resonance pulse is  $R_{RF}$ . The total number of spins in pool B is  $M_0^b$  and the total number of spins in pool A is  $M_0^a$  (a constant set to 1). The exchange rate between the pools is characterized by the rate constant,  $R$  (Henkelman et al., 1993). By obtaining several images with a range of different RF saturation pulses and using the mathematical description of the two pool model of the magnetization exchange, we can solve for various qMT parameters. These parameters include  $R$ ,  $R_a$ ,  $R_b$ , the  $T_2$  of both the liquid and

bound pools, and the fraction of protons in the bound pool ( $f$ ) (Henkelman et al., 1993; Ramani et al., 2002). As there are a large number of protons bound to macromolecules in the lipids that form myelin, it is not surprising that both MTR and qMT parameters have been found to correlate with tissue myelin content (Thiessen et al., 2013).

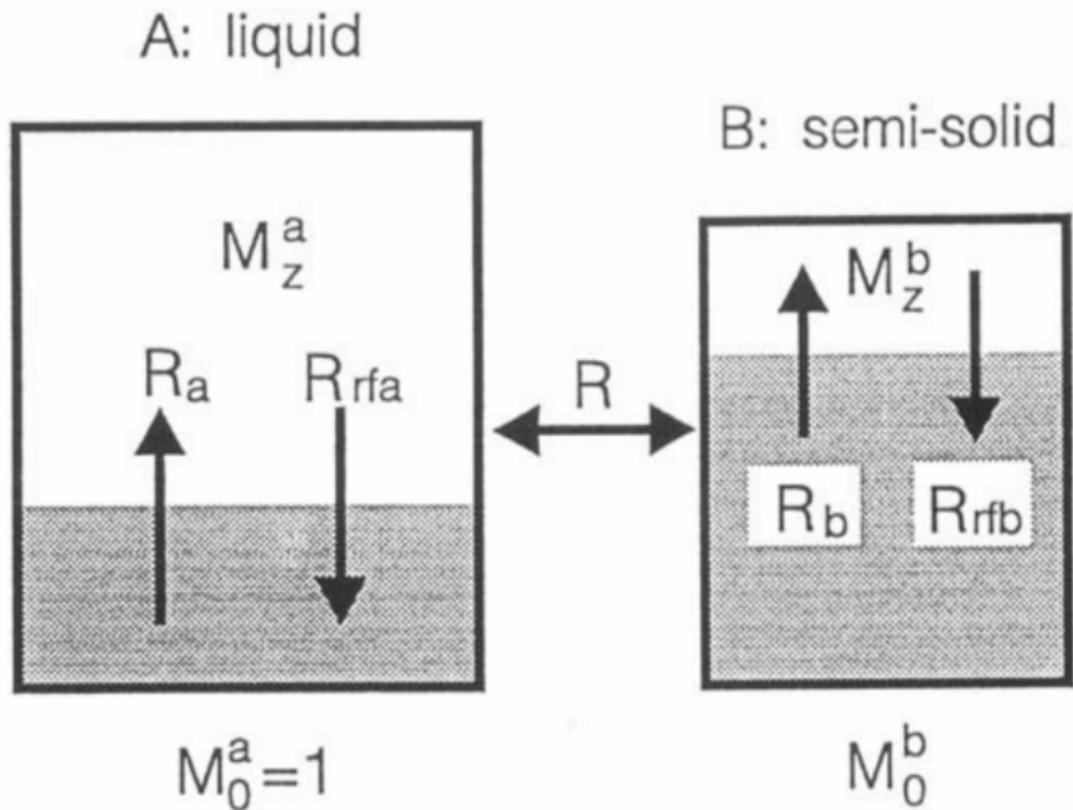


**Figure 1.1: The two-pool model of magnetization transfer.** The rectangles represent the liquid (A) and bound (or semi-solid; B) proton pools. The shaded region in each rectangle represents spins not aligned to the net magnetic field. Each pool has a rate of relaxation (liquid =  $R_a$ ; bound =  $R_b$ ) that is the inverse of its  $T_1$ . The rates of longitudinal magnetization loss due to the off-resonance pulses are  $R_{rfa}$  and  $R_{rfb}$ . The total number of spins in pool B is  $M_0^b$  and the total number of spins in pool A is  $M_0^a$  (a constant set to 1). Finally,  $R$  is the exchange rate between the two pools. From Henkelman et al., 1993.

### 1.2.1.5 Diffusion Tensor Imaging

Molecular diffusion is the random translational motion of molecules, also called Brownian motion, that results from the thermal energy carried by these molecules (Le Bihan et al., 2001; Beaulieu, 2002). Diffusion can be isotropic, equal in all directions, or anisotropic, not the same in all directions. Diffusion MRI can provide insight into tissue microstructure and will likely prove useful for *in vivo* quantification of MS pathology (Zhang et al., 2012a).

Diffusion is a type of contrast used in MR imaging (Neil, 2008). Mainly, we can encode the location of a water molecule by applying a diffusion-sensitizing magnetic field gradient pulse. After a delay of typically 50ms for clinical studies, we can use a second diffusion-sensitising field gradient is equal to the first. As a 180 degree pulse occurs between the two gradients spins are rephased by the second diffusion-sensitising gradient. The first application should dephase spins. The second gradient pulse should rephase the spins assuming that they are in the same location. If spins are stationary, the net phase change is zero. However, if the spins have diffused then they will cause the MRI signal to attenuate because the rephasing was imperfect (Neil, 2008; Pagani et al., 2008).

The diffusion coefficient,  $D$ , is a physical constant that characterizes the diffusion of a molecule. This coefficient is related to the root mean square displacement (RMS) of molecules over a given time (Beaulieu, 2002). This signal attenuation can be used to find the diffusion coefficient via the below equation:

$$\ln\left(\frac{I}{I_0}\right) = -bD$$

Where,  $I_0$  is the signal intensity without diffusion, and  $I$  is the signal intensity with diffusion.  $b$  is the b-value, a term that is a function of the gyromagnetic ratio of the nucleus of interest as well as the timing and gradient strength of the dephasing and rephasing pulses (Neil, 2008). Based on the equation above a plot

of  $\ln\left(\frac{I}{I_0}\right)$  vs. the b-value will be linear with the slope yielding D, the diffusion coefficient (Neil, 2008). This D would describe diffusion in a single direction, specifically the direction of the applied gradient magnetic fields. The diffusion coefficient measured in MRI is called the apparent diffusion coefficient (ADC) because it is not a true measure of the intrinsic diffusion but depends on the interaction of the diffusing molecules with cellular structure over a given time (Beaulieu, 2002).

Diffusion tensor imaging (DTI), first proposed by Basser, has been used to assess the structural integrity of white matter in MS patients (Basser, 1993; Basser et al., 1994b; Basser et al., 1994a; Pagani et al., 2008). In DTI, diffusion is described using a tensor. A tensor is a mathematical object similar to a vector, represented by an array of components that are functions of in space (i.e. diffusion in each direction). The effective diffusion tensor, as shown below can be used to fully describe the molecular mobility along each direction (Basser et al., 1994b; Le Bihan et al., 2001):

$$\underline{D} = \begin{matrix} D_{xx} & D_{xy} & D_{xz} \\ D_{yx} & D_{yy} & D_{yz} \\ D_{zx} & D_{zy} & D_{zz} \end{matrix}$$

This tensor ( $\underline{D}$ ) is composed of the apparent diffusion coefficients in multiple directions. Note that the tensor is symmetric (i.e.  $D_{xy} = D_{yx}$ ;  $D_{xz} = D_{zx}$ ;  $D_{yz} = D_{zy}$ ), meaning that a minimum of six measurements along six directions and a b=0 image are required to find the diffusion tensor. However, more directions are often used to avoid sampling biases (Basser et al., 1994b; Le Bihan et al., 2001).

Once the diffusion tensor components are determined the main direction of diffusivity and the diffusion values associated with these directions can be found by 'diagonalization' of the diffusion tensor (Le Bihan et al., 2001).

Diagonalization of the diffusion tensor involves manipulating it such that the off-diagonal terms of  $\underline{D}$  ( $D_{yx}, D_{zx}, D_{zy}, D_{xy}, D_{yz}, D_{xz}$ ) become zero.

Once diagonalized, the diagonal terms of the diffusion tensor are equal to the three primary eigenvectors,  $\lambda_{1-3}$  (Song et al., 2002; Song et al., 2005; Sun et al., 2006; Neil, 2008). The magnitude of these eigenvectors, called the eigenvalue, is the ADC along with the direction of the eigenvector. 3-dimensional diffusion ellipsoids are used to visually represent the eigenvector and eigenvalues (**Figure 1.2**) (Neil, 2008).

The first eigenvector ( $\lambda_1$ ), also known as axial diffusivity (AD), is oriented in the primary direction of water diffusion. We can assume that the primary direction of diffusion is along the axon. Thus we can also assume that the direction of the axon is parallel to the primary eigenvector. Decreased AD has been correlated with axonal injury. This could be a useful measure of axon integrity in MS patients. The second 2 eigenvectors ( $\lambda_2, \lambda_3$ ) are orthogonal to the first eigenvector. Their eigenvalues can be averaged to find radial diffusivity (RD). RD is thought to correspond to diffusion perpendicular to axons. Injury to myelin has been shown to increase radial diffusivity. Finally, all three eigenvalues can be averaged to find the mean diffusivity (MD), which is a more general measure of the amount of diffusion occurring in the tissue (Song et al., 2002; Song et al., 2005; Sun et al., 2006; Neil, 2008).

In addition to AD, RD, and MD we can also look at invariant indices of diffusion. These invariant indices are used because they are relatively independent of the choice of directions made for measurement and provide objective, intrinsic structural information (Le Bihan et al., 2001). These measures include relative anisotropy (RA), fractional anisotropy (FA) and the volume ratio (VR), the mathematical basis of which is explained in Chapter 3: Materials and Methods.

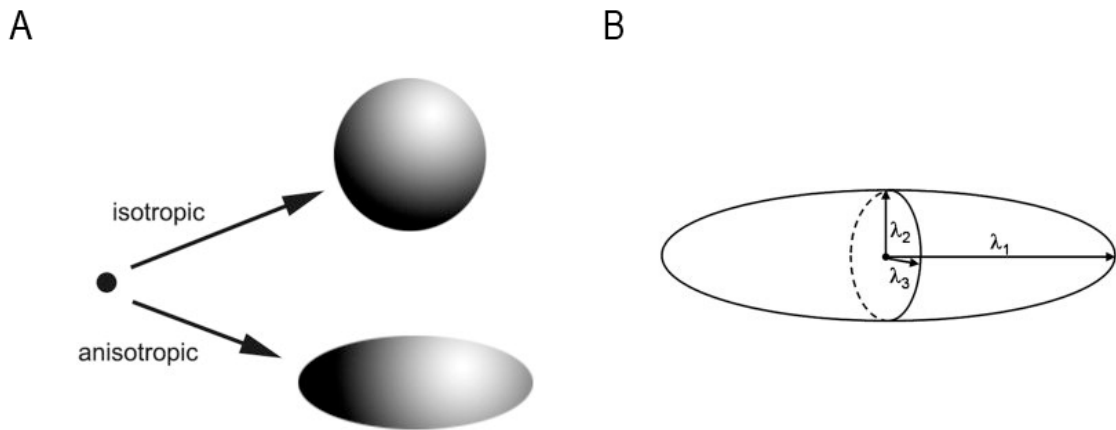


**Figure 1.2: Representative Diffusion ellipsoids.** **A:** Representative diffusion ellipsoids of isotropic, equal in all directions, (top) and anisotropic, greater in one direction, (bottom) diffusion. **B:** Representation of the diffusion ellipsoid showing eigenvectors.

From Neil, 2008.

For now, it suffices to say that the RA which is a normalized standard deviation represents the ratio of the anisotropic part of  $\underline{D}$  to its isotropic part. FA is the degree to which the diffusion ellipsoid deviated from being spherical (i.e. the extent to which diffusion is anisotropic). Both FA and RA are measured between 0-1 with 0 indicating isotropic diffusion and 1 is indicating anisotropic diffusion (Klawiter, 2013). The VR is the ratio of the ellipsoid volume to the volume of a sphere with the radius of MD. Like RA and FA, the VR ranges from 0-1 but unlike the other two indices, VR closer to 1 indicates isotropic diffusion and VR closer to 0 indicates anisotropic diffusion. VR allows one to assess the degree to which diffusion is spherical. If the white matter is damaged or fiber integrity is impaired, we would expect an increase in diffusion. If this increase in diffusion is orthogonal to the primary diffusion direction we expect to observe a decrease in FA or RA values and an increase in VR values (Soares et al., 2013).

Since RA, FA and VR reduce the diffusion tensor to one scalar value they do not necessarily give a good indication of the directional variation of the diffusion ellipsoid. A cigar-shaped and pancake-shaped ellipsoid can have equal FA even though the shape of diffusion differ. Geometric diffusion measures have been developed to better gauge the shape of the diffusion ellipsoid (Vilanova et al., 2006). These are the linear anisotropy (CL), planar anisotropy (CP) and the spherical anisotropy (CS). These values, along with the other parameters above, can be helpful in the characterization of the shape of the diffusion tensor along with orientation and integrity of CNS tissue (Kumar et al., 2014).

#### 1.2.1.6 Parameters affecting MR Signal

Several important factors should be kept in mind when acquiring MR images. These include the field of view (FOV), matrix size (the number of grid spaces in the x and y planes), and slice thickness. The FOV divided by the matrix of a direction gives the voxel size for that direction. For example, if the field of view is 1.25cm x 1.25cm and the matrix size is 128 x 128 then the voxel size, is

97.6 $\mu$ m x 97.6 $\mu$ m in the x and y-direction respectively. Obtaining images of mouse brain or spinal cord requires a small voxel. The smaller the voxel size, the higher the spatial resolution and thus the easier it is to resolve structures. However, the smaller the voxel size, the less tissue, the less signal present in each voxel and the lower the signal to noise ratio (SNR). More averages can be acquired to increase the SNR. However, each average doubles the imaging time. It is important to remember there are always trade-offs that will take place between time, SNR and spatial resolution.

### **1.3 Multiple Sclerosis: Pathophysiology**

MS is idiopathic and has a complex pathophysiology involving interactions between one's genetic predisposition, the environment and the immune system (Mallucci et al., 2015). Symptoms of MS have been shown to be primarily due to the damage to the integrity of myelinated white matter tracts within the CNS. Recent research has also highlighted the importance of gray matter damage in MS disease pathophysiology. Understanding the mechanisms that drive disease pathophysiology is critical when developing strategies to prevent and treat MS (Mallucci et al., 2015).

#### ***1.3.1 Pathogenesis of Multiple Sclerosis***

The exact cause of MS is still unknown. There is a complex interplay between genetic susceptibility and environmental factors influencing disease penetrance (Dendrou et al., 2015). Historically, two primary mechanisms have been thought to be potential triggers for MS. These include molecular mimicry and bystander activation of autoreactive immune T-cells (Libbey et al., 2007; Mallucci et al., 2015). Molecular mimicry occurs when infectious agents and self-antigens share peptide sequences or structural motifs (Fujinami and Oldstone, 1985; Wucherpfennig and Strominger, 1995; Mallucci et al., 2015). Bystander

activation, on the other hand, requires the activation of tissue-resident antigen presenting cells (APCs) within the CNS. The APCs then allow T cells to begin an autoimmune response against CNS epitopes (Munz et al., 2009; Mallucci et al., 2015).

It is thought that these two mechanisms likely act together (Mallucci et al., 2015). Activation of immune cells within the CNS may be caused by intrinsic, CNS-specific, or extrinsic, for example virally mediated, damage. This activation would lead to accumulation of CNS proteins in draining lymph nodes after leakage from the blood-brain barrier (BBB) (Stern et al., 2013; Mallucci et al., 2015). This leakage would then lead to the recruitment within the CNS of lymphocytes (from the periphery) primed against CNS antigens. Lymphocytes entering the CNS would induce the secretion of pro-inflammatory cytokines by microglia/macrophages. This secretion would lead to the destruction of CNS-tissue and the release of CNS antigens (i.e. epitope spreading)(McMahon et al., 2005; Sospedra and Martin, 2005b; Owens et al., 2011; Mallucci et al., 2015).

A newer theory regarding MS pathogenesis is the “inside-out” model of MS (Hauser and Oksenberg, 2006; Trapp and Nave, 2008; Dutta and Trapp, 2011; Stys et al., 2012). This model claims that MS is primarily a degenerative and not autoimmune disease. The initial degeneration is thought to promote an autoimmune and inflammatory response through the release of highly antigenic constituents. Evidence for this theory includes studies of early MS post-mortem tissue showing little signs of T or B cell infiltration in areas of demyelination and oligodendrocyte loss. These lesions do show macrophage infiltration and microglial activation, which is evidence of an innate immune response that is triggered to clear debris (Barnett and Prineas, 2004; Henderson et al., 2009; Stys et al., 2012). Additionally, progressive MS is characterized by reduced inflammatory episodes (Kuhlmann et al., 2002) yet neurological deficits continue to accumulate. This model might also explain why immunomodulators have been ineffective in the treatment of the progressive forms of MS.

### ***1.3.2 Multiple Sclerosis Lesions***

#### 1.3.2.1 White Matter Lesions

##### 1.3.2.1.1 Pathology

Charcot first described white matter (WM) lesions in MS as multiple focal sclerotic plaques scattered throughout the WM of the brain and the spinal cord (1998; Mallucci et al., 2015). We now know that WM lesions in MS tend to be located in the periventricular WM, juxtacortical border, cerebellum/brainstem or spinal cord (Fazekas et al., 1999; Mallucci et al., 2015). These four areas are collectively referred to as the MS typical regions of the CNS (Polman et al., 2011). The lesions in the brain tend to be round or ovoid, ranging in size from a few millimeters to more than a centimeter (Fazekas et al., 1999; Mallucci et al., 2015). Spinal cord lesions are typically located in the cervical region, run along the long axis of the cord, and extend less than two vertebral segments in length (Lycklama et al., 2003; Mallucci et al., 2015).

White matter lesions are segregated into four distinct patterns (I-IV), arising from different pathophysiological mechanisms (Lucchinetti et al., 1996; Mallucci et al., 2015). Pattern I lesions have a higher incidence in patients who have less than one year of disease history (Lucchinetti et al., 1996; Mallucci et al., 2015). Approximately 10% of total MS patients present with a pattern I lesion. They have sharply demarcated edges with perivascular infiltrating T cells and active demyelination. The most common type of WM lesion is the pattern II lesions. Large infiltration of T cells and myelin-laden macrophages, prominent deposition of immunoglobulins (Ig)s characterize these lesions. Also, ~55% of total MS patients present with pattern II lesions. Pattern III lesions are the second most common. Ill-defined borders characterize pattern III lesions. These lesions also have dying oligodendrocytes and inflamed vessels that are surrounded by myelin. This myelin is intact but has lost myelin-associated glycoprotein (MAG). ~30% of total MS patients present with pattern III lesions.

Finally, pattern IV lesions are the rarest type. Pattern IV lesions, have infiltrating T cells and activated microglia/macrophages. Around pattern IV lesions one can see extensive non-apoptotic oligodendrocyte degeneration. These lesions are seen only in PPMS patients (Lucchinetti et al., 1996; Mallucci et al., 2015).

Notably, distinct mechanisms driving the initial demyelination have been described within the different lesion patterns of MS (Lucchinetti et al., 1996; Mallucci et al., 2015). In patterns I and II, it is thought that the primary damage occurs to the myelin sheaths that subsequently triggers demyelination. In patterns III and IV the death of the oligodendrocyte, the cell that produces myelin in the CNS, is the primary driver of demyelination (Lucchinetti et al., 1996; Mallucci et al., 2015).

#### 1.3.2.1.2 Magnetic Resonance Imaging of White Matter Lesions

T1-weighted images along with the MRI contrast agent, gadolinium, can be used to monitor inflammatory and acute demyelinating MS lesions. These lesions cause an increase in blood-brain barrier permeability allowing gadolinium to enter the CNS (Klawiter, 2013). Gadolinium is highly paramagnetic, since it has seven unpaired electrons, and shortens the  $T_1$  relaxation time causing a signal enhancement on T1 weighted MR when it is present in tissue (Bellin and Van Der Molen, 2008). In MS lesions this contrast enhancement typically persists for one month on average, allowing clinicians to classify lesions as either acute (gadolinium-enhancing) or chronic (non-gadolinium enhancing)(Cotton et al., 2003). Contrast-enhanced T1 weighted imaging is now routinely used in the study of MS and provides an *in vivo* measure of inflammatory activity (Ge, 2006). This type of imaging can detect disease activity 5-10 times more frequently than the clinical evaluation of relapses (Barkhof et al., 1992), suggesting that most enhancing lesions are clinically silent (Ge, 2006).

However, there are issues with contrast enhanced T1 weighted imaging in MS. First, contrast enhanced T1 weighted lesions are less common in the progressive forms of MS (Klawiter, 2013). Second, the dosage of the contrast agent can influence the number of enhancing lesions. It has been demonstrated that larger dose can result in both an increased number and size of enhancing lesions (Wolansky et al., 1994; Sardanelli et al., 2003; Ge, 2006).

T1 weighted hypointensities (“black holes”) may also be present in the MRI scans of patients with MS. The majority of these will resolve and are called transient black holes while a minority will persist (lasting 12 months or longer)(Bagnato et al., 2003). A study of MS post-mortem brains demonstrated that chronic black holes correlated with greater tissue damage and increased axonal damage on histopathology (van Walderveen et al., 1998). Additionally, another study demonstrated that the accumulation of these black holes correlates with disease progression and disability in SPMS (Truyen et al., 1996).

T2-weighted hyperintensities (bright spots) are a standard feature in MS (McDonald et al., 2001; Polman et al., 2011). However, T2-weighted lesions are highly non-specific and can contain a variable extent of demyelination, remyelination, axonal loss, inflammation, and edema. This lack of specificity may play a role in the clinical-radiological paradox; a phenomenon in MS where lesion load on radiological scans does not appear to correlate with the extent of disability (Klawiter, 2013).

The DTI parameter, fractional anisotropy (FA) has found to be lower in lesion areas compared to NAWM (Filippi and Inglese, 2001) and it appears always to be lower in enhancing lesions. Additionally, FA values in NAWM are lower than those of corresponding control white matter (Werring et al., 1999; Bammer et al., 2000; Filippi, 2000; Cercignani et al., 2001; Filippi et al., 2001; Filippi and Inglese, 2001). Studies of DTI of white matter have also revealed a decreased FA and an increased mean diffusion (MD) in non-lesion areas (Filippi et al., 2001; Filippi and Inglese, 2001), suggesting the presence of subtle

microstructural changes that are beyond the resolution of conventional MRI. These studies are consistent with the findings of other pathological studies demonstrating that tissue damage in MS is not restricted to T2-visible lesions (Jonkman et al., 2015)

#### 1.3.2.2 Gray Matter Lesions

Until recently, MS was considered primarily a white matter disease. It is thus surprising to learn that gray matter (GM) involvement in MS was initially described by the founder of MS, Jean-Martin Charcot, in the 1800's (Mallucci et al., 2015). He was the first to point out the existence of demyelinating lesions within the GM of the brain of MS patients. For many years his findings were neglected, likely due to the difficulty of visualizing GM lesions with traditional histological methods. In 1962 Brownell and Hughes performed the first extensive analysis of GM lesions. They found that GM lesions accounted for ~26% of total MS lesions (Brownell and Hughes, 1962; Mallucci et al., 2015). Since this time advanced imaging techniques have established that cortical demyelination is, in fact, a common feature of all forms of MS (Filippi and Rocca, 2012; Geurts et al., 2013; Mallucci et al., 2015)

GM lesions, although common and widespread, tend to not be visible on conventional MRI. GM lesions tend to have a longer relaxation time which results in poor contrast resolution between normal appearing GM and GM lesions in the cortex. To better visualize GM lesions in MS newer techniques are being developed. Hulst and Geurts, 2011 reviews such methods.

### ***1.3.3 Glial and Neuronal Damage***

#### 1.3.3.1 White Matter

Oligodendrocytes are a type of glial cell that provides support and insulation to neurons in the CNS by wrapping them in a myelin sheath, a lipid-

rich concentric membrane (Hauser and Oksenberg, 2006; Mallucci et al., 2015). The myelin sheath provides trophic support to neurons and alters the electrical properties of the axon. It creates areas of high resistance and low capacitance that cause rapid saltatory conduction of nerve impulses (Waxman and Ritchie, 1993; Irvine and Blakemore, 2008). Damage to myelin or oligodendrocytes by autoimmune disease or other mechanism causes deficits in neuronal function that may be reversible or permanent (Mallucci et al., 2015).

In type I and II lesions, demyelination are triggered primarily by direct damage to the myelin sheath (Lucchinetti et al., 2000; Mallucci et al., 2015). This direct damage may be caused by toxic factors produced by activated macrophages (Hofman et al., 1989; Selmaj et al., 1991; Bitsch et al., 2000) or by humoral immunity (Genain et al., 1999; Lucchinetti et al., 2000). Approximately one-third of MS patients develop autoantibodies against myelin. Also, it appears that these autoantibodies are more likely to be detected in RRMS patients than in PPMS (Elliott et al., 2012; Mallucci et al., 2015).

The serum, cerebral spinal fluid (CSF) (Reindl et al., 1999), and lesions of MS patients have been found to contain anti – myelin oligodendrocyte glycoprotein (MOG) antibodies (Genain et al., 1999; Mallucci et al., 2015). Patients with other demyelinating disorders such as acute disseminated encephalomyelitis (ADEM) and optic neuritis (Willison and Linington, 2012), as well as healthy controls (Lampasona et al., 2004) also contain anti-MOG antibodies. Another study indicates that the MOG index, a measure of the level of antibodies to MOG within the CNS, may be a promising diagnostic tool and a marker of disease progression in MS patients (Klawiter et al., 2010; Mallucci et al., 2015). The role of anti-MOG antibodies, as well as other autoantibodies in MS, has yet to be fully understood.

Unlike type I and II lesions, in type III and IV lesions demyelination is triggered primarily by the death of the oligodendrocytes themselves (Lucchinetti et al., 2000; Mallucci et al., 2015). The most likely cause of the rare Type IV patterns lesions is the release of toxic factors from activated macrophages. On

the other hand, type III pattern lesions appear to be linked to failure in mitochondrial activity which causes the death of oligodendrocytes via the release of apoptotic factors, while simultaneously disrupting the differentiation of oligodendrocyte precursor cells (OPCs) (Ziabreva et al., 2010; Mallucci et al., 2015). Mitochondrial injury can be caused by reactive oxygen species and nitric oxide released by activated microglia (Fischer et al., 2012; Mallucci et al., 2015).

Once demyelination has occurred, sodium channels, typically located at the nodes of Ranvier, become distributed along the axon. When ATP production is reduced, for example in white matter lesions, the sodium-potassium ATPase pump becomes impaired. In its place, the sodium/calcium exchanger, which usually exchanges calcium inside the axon for sodium in the extracellular space, will reverse its activity until an increase in calcium inside the axon causes a degenerative response (Waxman, 2006; Smith, 2007; Mallucci et al., 2015). Increased calcium in the axon causes a cycle of impaired mitochondrial function, thus further propagates damage (Mahad et al., 2008a; Mahad et al., 2008b). The term virtual hypoxia is used to describe this imbalance between increased energy demand and decreased energy supply. This process eventually leads to degeneration of the axon in WM (Lassmann, 2003; Trapp and Stys, 2009; Mallucci et al., 2015).

Understanding the mechanism that drives demyelination and subsequent axonal loss in MS is essential for the development of therapies that reduce demyelination and promote remyelination in MS (Mallucci et al., 2015)

#### 1.3.3.2 Gray Matter

Progressive GM damage is now well established as one of the leading causes of irreversible neurological disability in MS patients. This cortical damage can be caused indirectly by degeneration of connecting WM tracts or directly via demyelinating plaques localized within the cortex (Mallucci et al., 2015).

Regarding indirect cortical damage, it is thought that axonal destruction may be induced by inflammatory WM lesions, which leads to secondary or Wallerian tract degeneration and global brain atrophy (Kornek and Lassmann, 1999; Mallucci et al., 2015). It has been shown that the formation of new cortical lesions is more likely to occur in areas that were connected to sites of previous damage in the WM (Kolasinski et al., 2012; Mallucci et al., 2015). This process may remain clinically silent for many years. However, compensatory CNS resources are eventually exhausted, and the result is an irreversible neurological disability (Bjartmar et al., 2003; Mallucci et al., 2015).

It has been shown that cortical demyelination can occur in areas that are not directly connected to areas of WM damage (Bo et al., 2007; Mallucci et al., 2015). A recent study demonstrated that oxidative injury may be one the major driving forces in cortical demyelination (Fischer et al., 2013; Mallucci et al., 2015). This oxidative damage appears to be related to mitochondrial impairment in damaged axons (Mallucci et al., 2015). The mitochondrial damage is probably caused by free oxygen radicals produced during inflammation and dysfunctional mitochondria themselves (Fischer et al., 2012).

#### ***1.3.4 Remyelination***

Remyelination is the process by which oligodendrocytes and oligodendrocyte precursor cells (OPCs) re-ensheath demyelinated axons (Mallucci et al., 2015). Spontaneous remyelination does occur in humans and is a highly regulated process that requires multiple steps for completion. Early in the MS disease course remyelination occurs in lesions. A repeated cycle of de- and remyelination leads to a myelin sheath that is thinner and shorter than normal (Ludwin and Maitland, 1984; Mallucci et al., 2015). Post-mortem studies suggest that the extent of remyelination that occurs is related to the location of the lesions. Deep WM and subcortical lesions appear to be more likely to undergo

complete remyelination than those in periventricular areas (Patrikios et al., 2006; Mallucci et al., 2015).

In MS, remyelination can occur in variable amounts; when it occurs and by how much is poorly understood (Mallik et al., 2014). Evidence of failure of remyelination has been seen in chronic MS patients (Mallucci et al., 2015). Maturing OPCs are rarely seen in the WM lesions of chronic MS patients indicating that there may be a block in the differentiation of OPCs causing remyelination failure (Antel et al., 2012; Mallucci et al., 2015). It is thought that remyelination is inhibited in slowly expanding lesions that are characteristic of progressive MS due to impaired clearance of myelin debris (Bramow et al., 2010; Miron and Franklin, 2014; Mallucci et al., 2015).

Failure to remyelinate is correlated with inefficient recruitment or lack of differentiation of OPCs (Mallucci et al., 2015). It is thought that the continued presence of autoreactive T cells in MS creates a hostile environment for oligodendrocyte function that inhibits complete remyelination (Mallik et al., 2014). OPC differentiation requires three steps. First OPCs establish contact with an axon, then they express a series of myelin-specific genes, and finally they ensheath the axon. Each process is tightly regulated by the release of several growth factors (Murtie et al., 2005; Mallucci et al., 2015) and by activation of a specific membrane and nuclear signaling pathways (Mallucci et al., 2015). An emerging focus of MS treatments has been to develop therapies to promote remyelination (Keough and Yong, 2013).

### ***1.3.5 Multiple Sclerosis: Treatments***

#### **1.3.5.1 Current Treatments**

There is no cure for MS. However, treatments, also known as disease-modifying therapies (DMTs), are available. In 1993 the first disease modifying therapy for RRMS, interferon beta-1b, was introduced (Buck and Hemmer,

2011). Now there are several DMTs available to patients with RRMS. The short term aims of these DMTs are to reduce MRI activity, and the frequency, and severity of relapses (Ontaneda et al., 2012). All medications approved for the treatment of RRMS have been shown to achieve these short term goals, although the magnitude and robustness of the benefits do vary. First-line therapies are safer and well tolerated, but they are only moderately effective for patients as a group. Second-line therapies have greater efficacy but also have substantial safety concerns (Ontaneda et al., 2012).

These DMTs tend to aim to suppress or alter the autoimmune process underlying the pathogenesis of MS (Sospedra and Martin, 2005a; Hemmer et al., 2006). Such DMTs modulate immune cell subsets, reduce leukocyte trafficking across the blood-brain-barrier, or sequester cells in peripheral secondary lymphoid organs (Keough and Yong, 2013). These processes appear to be an ineffective strategy for the treatment of progressive forms of MS. The inside-out model of MS described above has been put forth as a potential explanation for this lack of efficacy.

#### 1.3.5.2 Developing Treatments

Current research into MS therapeutics has begun focusing on neuroprotective agents. Since neurodegeneration occurs early during the disease and accumulates over time (Lukas et al., 2010), these agents will probably be highly effective in the treatment of MS. The focus of such neuroprotective agents will likely be to increase remyelination and reduce demyelination. It has been postulated that chronic demyelination underlies the progressive axonal injury, neuronal death, and disease progression seen in MS (Trapp and Nave, 2008; Hagemeyer et al., 2012). Additionally, animal studies have shown that remyelination can protect axons from demyelinated axon associated degeneration (Irvine and Blakemore, 2008), can restore axon conduction to

levels seen before demyelination (Smith et al., 1981), and can lead to functional recovery (Duncan et al., 2009).

A list of potential remyelination therapies that have shown promise in experimental models of demyelination can be found in Mallik et al., 2014. To develop therapies that reduce demyelination and promote remyelination we require imaging methods that are non-invasive, sensitive and specific to either myelin or axonal content of tissue, quantitative and available for use at the clinical and pre-clinical level. Overall, the most likely candidate for monitoring remyelination in MS comes from MR imaging markers (Mallik et al., 2014).

#### **1.4 Magnetic Resonance Imaging of Demyelination and Remyelination**

Some possible MRI techniques that are candidates for this include but are not limited to MTR, qMT and DTI.

As mentioned above MTR is one way to quantify the exchange in magnetization that occurs between the bound and free pools. MTR has the advantages of having a relatively short acquisition time and it is available on commercial scanners (Mallik et al., 2014). Additionally, MTR is strongly affected by myelin (Mallik et al., 2014). Studies of MS patients have demonstrated that demyelinating lesions have a lower MTR than inflammatory lesions (Guo et al., 2001; Ge, 2006). A longitudinal study of the evolution of MTR in gadolinium-enhancing lesions found a marked reduction in MTR at the lesion site followed by partial or complete resolution as inflammation reduced and remyelination occurred (Chen et al., 2008; Klawiter, 2013). In post-mortem MS brains MTR was found to be significantly higher in areas of remyelination compared to areas of demyelination (Schmierer et al., 2004; Bodini et al., 2015). Areas of remyelination had a significantly lower MTR compared to NAWM, this may be due to incomplete remyelination, morphological differences in newly formed myelin or axonal loss (Schmierer et al., 2004; Mallik et al., 2014).

It has been shown that MTR is influenced by water content, inflammation and axonal damage (Schmierer et al., 2004; Vavasour et al., 2011; Mallik et al., 2014). Other disadvantages of MTR include that it is semi-quantitative and can depend on MT pulse properties, the type of acquisition, excitation pulse flip angle and echo time, and repetition time (Mallik et al., 2014). Also, as mentioned above, it cannot distinguish between the different factors that affect magnetization transfer, including but not limited to the rate of exchange and the amount of the bound pool.

qMT can be used to separate these variables. qMT uses mathematical models of the magnetization transfer effect in biological tissue to measure fundamental quantitative parameters related to the magnetization transfer effect, including the fraction of protons in the bound pool ( $f$ ) (Cercignani et al., 2005; Mallik et al., 2014). These quantitative parameters are significantly influenced by tissue myelin content (Mallik et al., 2014). They are also reliable and reproducible (Levesque et al., 2010a; Mallik et al., 2014).

Additionally, qMT parameter bound pool fraction ( $f$ ), a measure of the fraction of protons in the semisolid pool, has been a stronger correlate to myelin content of tissue than MTR (Schmierer et al., 2007a; Thiessen et al., 2013). qMT has not been as extensively studied in MS patients as MTR. However, one study reported a reduction in  $f$  in MS lesions and NAWM. A serial study of 6 RRMS patients with acute gadolinium-enhancing lesions using qMT imaging, demonstrated a decrease of both MTR and  $f$  in acute lesions (Giacomini et al., 2009; Mallik et al., 2014). Both parameters recovered over several months, which may have been due to remyelination. Interestingly the reduction in MTR although present was smaller than that observed in  $f$ . The authors contributed this to edema increasing the  $T_1$  and thereby attenuating the MTR reduction (Giacomini et al., 2009; Mallik et al., 2014). This data was later validated by a study that looked at gadolinium-enhancing regions in 5 RRMS patients (Levesque et al., 2010b). Additionally, it has been shown that the qMT imaging parameters

decrease before gadolinium-enhancing lesion formation which may indicate early demyelination (Fazekas et al., 2002).

The challenges in qMT measurements include that it requires several images to be taken to fit the model to the data and to estimate the fundamental qMT parameters (Mallik et al., 2014). This imaging process is time-consuming. It is, however, a technique worth exploring further as the results of animal studies support the hypothesis that  $f$  is an imaging biomarker of demyelination (Ou et al., 2009a; Mallik et al., 2014). It is not unreasonable to believe that qMT would be just as useful in detecting remyelination.

Another potential imaging technique that could be used to monitor remyelination is DTI. Diffusion weighted images provide information about the diffusion behaviour of water which is altered in as a consequence of microstructural changes (Pierpaoli et al., 2001; Mallik et al., 2014). Using DTI, it is possible to derive several imaging biomarkers for characterizing tissue microstructural abnormalities (Mallik et al., 2014). These include fractional anisotropy (FA), mean diffusion (MD), axial diffusion (AD), radial diffusion (RD), relative anisotropy (RA), linear anisotropy (CL), planar anisotropy (CP), spherical anisotropy (CS) and the volume ratio (VR).

FA has been shown to correlate both with axonal count (Schmierer et al., 2007b; Gouw et al., 2008) and myelin content (Schmierer et al., 2007b; Mallik et al., 2014). Additionally, RD and AD have been shown to reflect myelin content and axon content respectively, particularly in areas with high fibre coherence (Song et al., 2002; Song et al., 2005; Mallik et al., 2014). Along with axon and myelin characteristics other aspects of fiber features, such as orientation coherence and packing of axons, axonal caliber, membrane permeability, and the presence of other cells such as glia and immune cells, can also contribute to changes in axial and radial diffusivity (Le Bihan et al., 2001; Kumar et al., 2012).

A study in post-mortem fixed MS spinal cords showed that RD distinguished between worsening severities of demyelination (Klawiter et al.,

2011). The RD in this study was decreased in areas with moderate-severe demyelination compared to both mild demyelination and normal white matter (Klawiter et al., 2011). A similar study showed that both MD and FA correlate to tissue myelin content in post-mortem MS tissue (Schmierer et al., 2007b). Additionally, RD in the corticospinal tracts and posterior columns are correlated with clinical measures of disability in MS (Naismith et al., 2013; Mallik et al., 2014). However, the specificity of DTI metrics to myelin in the spinal cord is unclear. There may be confounding effects of increased cellularity or inflammation-induced edema (Grossman et al., 2000; Mallik et al., 2014).

The main limitation with DTI comes from the fact that the parameters used are dependent on the ability of this model to detect the correct fibre tract orientation per voxel (Mallik et al., 2014). This limitation becomes a problem in areas of complex tissue microstructure where the proper orientation of fibers may not be detectable (Laule et al., 2007; Wheeler-Kingshott and Cercignani, 2009; Mallik et al., 2014). Also, in the presence of joint inflammation and demyelination, RD may underestimate the amount of demyelination and AD may overestimate the amount of axonal loss (Wang et al., 2011).

Each of the above techniques has its advantages and disadvantages. As trials of potential neuroprotective agents become more important in the overall spectrum of MS research, these experiments should be designed to maximize their sensitivity to actual treatment effects (Mallik et al., 2014). This maximization involves selecting patient groups with the most potential to show a response and obtaining large sample sizes (Mallik et al., 2014) but most importantly it includes selecting an imaging outcome that accurately measures treatment responses. This selection process requires a thorough understanding of how the different potential imaging techniques respond to demyelination and remyelination in various situations. Animal models can be used to gain this understanding.

## **1.5 Multiple Sclerosis: Animal Models**

No single animal model represents the entire spectrum of heterogeneity of human MS (Procaccini et al., 2015). However, some animal models mimic aspects of MS disease pathology. These animal models are used as tools to study disease development and novel therapeutic approaches. There are valid concerns about how representative these animal models can be since they do not reflect all aspects of the disease. While we should keep these concerns in mind, animal models have provided us with valuable insight into the pathophysiology of illness (Nathoo et al., 2014a). Each of the below animal models provides a different route of investigation into MS disease processes (Nathoo et al., 2014a).

### ***1.5.1 Experimental Autoimmune Encephalomyelitis***

Experimental autoimmune encephalomyelitis (EAE) is the most commonly used animal model of MS (Nathoo et al., 2014a, b; Procaccini et al., 2015). In this model autoimmunity to CNS components is induced through immunization with self-antigens derived from myelin proteins (Procaccini et al., 2015). The first description of this model was in monkeys that had been immunized with rabbit brain extracts which caused paralysis associated with demyelination of the brain and spinal cord (Rivers et al., 1933). Later this procedure was modified to also use Freund's adjuvant (CFA)(Freund and McDermott, 1942) and pertussis toxin (PT)(Munoz and Mackay, 1984). These compounds potentiate the humoral immune response and induce oscillatory symptoms more typical of a relapsing-remitting disease (Procaccini et al., 2015). Rodent EAE models, particularly mice, are the most commonly used because of their affordability and the availability of genetically modified strains (Ransohoff, 2012; Nathoo et al., 2014a).

The immunogens that can be used to induce EAE are derived from self-CNS proteins and include myelin basic protein (MBP), proteolipid protein (PLP) or myelin oligodendrocyte glycoprotein (MOG)(Procaccini et al., 2015). The type of

response obtained is dependent both on the strain of mouse and the immunogen used for induction. Immunization of SJL/J mice with an epitope of PLP induced a relapsing-remitting disease course (Tompkins et al., 2002), while immunization of C57BL6/J mice with MOG causes more of a chronic illness (Tuohy et al., 1989).

EAE in mice is characterized by an ascending paralysis starting at the tail and progressing toward the forelimbs (Batoullis et al., 2011; Procaccini et al., 2015). The paralysis seen in EAE can be assessed using a 5 (McRae et al., 1992; Berard et al., 2010) or 15 point scale (Weaver et al., 2005). Regarding pathology MS and EAE share many characteristics including the destruction of myelin sheaths and axonal degeneration (Steinman and Zamvil, 2005; Nathoo et al., 2014a). Like MS, EAE lesions show DIT/DIS (Adams and Kubik, 1952; Baxter, 2007) and have the presence of CD4<sup>+</sup> and CD8<sup>+</sup> T cells that are reactive to myelin (Steinman and Zamvil, 2005). Finally, studies have also shown that the process of leukocyte migration into the CNS is similar in EAE and MS (Agrawal et al., 2011).

These similarities make EAE a model that has been significant in contributing to our knowledge of autoimmunity and neuroinflammation in MS (Procaccini et al., 2015) but like any model it does have its limitations. These include that EAE cannot be used to study relapse rate, acute EAE mainly affects the spinal cord with white matter unlike MS, and acute EAE does not provide information about disease progression (Procaccini et al., 2015).

EAE white matter has a reduced MTR (Gareau et al., 2000), similar to MS (Nathoo et al., 2014a). Later it was shown that MTR correlates well with levels of demyelination in EAE (Brochet and Dousset, 1999). Another study that compared MTR to bound pool fraction (f) in EAE mice found that f was more sensitive to demyelination than MTR (Rausch et al., 2009). AD has been shown to correlate with axonal injury in EAE and anisotropy measures correlated with clinical disability in this model (Budde et al., 2008; Budde et al., 2009). AD and RD have

also been shown to correlate with clinical disability in EAE and can be used as outcome measures in pre-clinical trials of MS therapeutics (Wang et al., 2013).

It is hard to study remyelination in EAE mice because lesions occur randomly in terms of timing and location. This randomness makes it difficult to distinguish lesions undergoing demyelination from those undergoing remyelination. It is also challenging to determine whether changes seen in MRI methods in this model are due to inflammation or demyelination (Nathoo et al., 2014a). These limitations make EAE a less than ideal model in which to study the effects of potential remyelinating therapies.

### ***1.5.2 Theiler's Murine Encephalomyelitis Virus***

Theiler's murine encephalomyelitis virus (TMEV) is a non-enveloped, positive-sense, single-stranded RNA virus (Tsunoda and Fujinami, 2010) and is a neurotropic viral infection model for MS (Libbey et al., 2007). This model is particularly intriguing because a virus, Epstein-Barr, has been linked to MS as an environmental susceptibility factor (Procaccini et al., 2015). Intracerebral administration of TMEV in susceptible mouse strains, like SJL/J, leads to demyelination (Dal Canto et al., 1996). There are two subgroups of TMEV, GDVII and TO. GDVIIs are highly neurovirulent for mice and induce death within 1 to 2 weeks. TOs are the milder strains producing acute polioencephalomyelitis. In contrast to EAE, TMEV appears to only be able to induce a demyelinating disease in mice and is always chronic and progressive (Owens, 2006; Procaccini et al., 2015).

TMEV contains T<sub>2</sub> hyperintensities that are presumed to relate to demyelination. They have not however been linked to demyelination specifically. Few others studies looking at MRI in the TMEV model exist. A good review of the studies of TMEV and MRI can be found in Nathoo et al., 2013 a and b.

The main advantages of the TMEV model include that the virus-induced pathology is similar to the chronic progressive forms of MS. Also, the demyelination induced in this model is through activation of the immune system and not a direct result of the virus itself. Additionally, it can be useful for testing therapies targeting adhesion molecules, axonal degeneration, and immunosuppression (Procaccini et al., 2015). The disadvantages of this model include that it can only cause a demyelinating disease in mice and that demyelination requires persistent viral infection which is not the case in MS patients (Procaccini et al., 2015). Like EAE, TMEV is not ideal for studying potential remyelinating therapies.

### ***1.5.3 Cuprizone***

Toxic demyelinating models like cuprizone, ethidium bromide and lyssolecithin are more suitable than EAE and TMEV to study de- and remyelination (Blakemore and Franklin, 2008). Cuprizone is a (bis-cyclohexanone-oxaldihydrazone) is a copper chelator which is added to rodent chow, leading to oligodendrocyte cell death with subsequent demyelination in the corpus callosum, superior cerebellar peduncles, and the cortex (Matsushima and Morell, 2001; Skripuletz et al., 2008; Procaccini et al., 2015). Ingestion of cuprizone for six weeks followed by a regular diet for six weeks causes demyelination followed by remyelination (Matsushima and Morell, 2001). Ingestion of cuprizone for 12 consecutive weeks leads to chronic demyelination (Matsushima and Morell, 2001).

The precise mechanism underlying demyelination induced by cuprizone ingestion is not entirely understood (Procaccini et al., 2015). Administration of copper along with cuprizone does not reduce the toxic effects of cuprizone (Hemm et al., 1971). Therefore, the chelator effects of cuprizone are probably not the primary cause of demyelination. We do know that cuprizone causes

mitochondrial disturbances. This mitochondrial dysfunction is seen in both the liver and brain of cuprizone-treated mice (Suzuki, 1969; Komoly et al., 1987). It is also known that cuprizone causes oligodendrocyte apoptosis while other cells appear to be unaffected and it is this oligodendrocyte cell death which causes demyelination (Procaccini et al., 2015), like type III and type IV lesions in MS. This evidence suggests that the large bio-energetic demand of oligodendrocytes, which require large amounts of oxygen and ATP for membrane synthesis, cannot be met by the dysfunctional mitochondria in cuprizone mice (Procaccini et al., 2015).

The cuprizone model can be used to study the mechanisms of de- and remyelination in the absence of primarily immune-mediated phenomenon (Procaccini et al., 2015). Magnetization transfer imaging has been used to monitor changes in white matter post cuprizone intoxication (Nathoo et al., 2014a). MTR has been shown to decrease with demyelination and increase with remyelination (Zaaraoui et al., 2008). A study done in 2013 looked at a variety of MRI measures in mice exposed to cuprizone for six weeks (Thiessen et al., 2013). This study found significant reductions in MTR, the bound pool fraction ( $f$ ) and the rate of exchange between the bound and free pools ( $k$ ) in the corpus callosum and external capsule. Additionally, this study found that of the MRI parameters assess  $f$  had the strongest significant correlation to myelin, suggesting that the reduction in  $f$  was due to myelin loss (Thiessen et al., 2013).

Additionally, this study saw significant reductions in FA and AD while RD and MD were significantly increased in cuprizone mice (Thiessen et al., 2013). This model has been used to demonstrate that radial diffusivity increases with demyelination (Song et al., 2005; Sun et al., 2006; Xie et al., 2010) and decreases during remyelination (Song et al., 2005; Nathoo et al., 2014a).

The disadvantages of this model include that the copper chelator may have yet unknown effects on cells other than oligodendrocytes which may indirectly affect the de- and remyelination process. It is also difficult to

histologically quantify remyelination in the corpus callosum, one of the primary areas of demyelination in the cuprizone model (Keough et al., 2015). Also, the timeline of the cuprizone model, which takes 12 weeks to de- and remyelinate, is longer than the lysolecithin model described on the next page.

#### ***1.5.4 Ethidium Bromide***

Ethidium bromide is a toxic agent which causes intercalation with nucleic acids, thus injuring any cells containing a nucleus (Waring, 1965; Merrill, 2009). When injected into the dorsal column of the spinal cord or the caudal cerebellar peduncle this toxin causes demyelination followed by spontaneous remyelination (Waring, 1965). Therefore, like cuprizone above can be used to study de- and remyelination. In this model maximum demyelination occurs two weeks after injection (Graca and Blakemore, 1986). Not until around 14 weeks after injection is extensive remyelination seen in this model (Woodruff and Franklin, 1999). A diffusion study of ethidium bromide in rat spinal cord found that during demyelination RD decreased and AD increased (Talbot et al., 2016). Like the cuprizone model, the ethidium bromide model has a longer timeline for de- and remyelination than the lysolecithin model described below.

#### ***1.5.5 Lysolecithin***

An injection of the detergent lysophosphatidylcholine (lysolecithin) into the CNS causes demyelination and remyelination lasting roughly two weeks (Nathoo et al., 2014a; Keough et al., 2015). The area of injection may be the dorsal or ventral columns of the spinal cord, the corpus callosum or the internal capsule (Nathoo et al., 2014a). Lysolecithin is an activator of phospholipase A2, and it is believed that demyelination occurs due to primary toxic effects of the detergent on the myelin sheath and not secondary effects on oligodendrocytes (Hall, 1972; Denic et al., 2011). This mechanism of damage makes it similar to

type I and type II MS lesions. Studies have demonstrated that lysolecithin-induced demyelination is not immune dependent and is present also in immune-deficient mice (Denic et al., 2011). However, shortly after lysolecithin injection, there is a short-lived infiltration of T cells, B cells, and macrophages. This immune response is thought to be beneficial for remyelination (Bieber et al., 2003).

The purpose of this model is not to mimic MS as a disease but to provide a model to study the process of demyelination and remyelination (Blakemore and Franklin, 2008; Denic et al., 2011). The advantages of this model include knowledge of the lesion location, a well-described and short timeline of de- and remyelination, and minimal axonal damage or inflammation compared to other models. One disadvantage of this model include that the cause of demyelination is not autoimmune as is thought to be the cause in MS.

The MTR has been shown to be reduced with demyelination in both rodent and monkey lysolecithin models (Dousset et al., 1995; Deloire-Grassin et al., 2000; McCreary et al., 2009; Nathoo et al., 2014a). MTR changes with remyelination have been more variable with one study showing an increase in remyelination in lysolecithin injected rats (Deloire-Grassin et al., 2000) and another showing no significant change with remyelination in lysolecithin injected mice (McCreary et al., 2009). In both these studies, MTR did not return to baseline values which may be attributed to incomplete remyelination (Deloire-Grassin et al., 2000; McCreary et al., 2009; Nathoo et al., 2014a). To the best of our knowledge, no study exists that has assessed quantitative magnetization transfer in this model. Using DTI, the FA and AD have been shown to decrease while RD increases in lysolecithin-injected rats (DeBoy et al., 2007). Additionally, the lesion was visible in DTI tractography, a method that provides a visual representation of white matter tracts (Nathoo et al., 2014a).

The MRI methods used to investigate white matter changes over the lysolecithin disease course are promising. However, further work needs to be

done to identify which method or methods can reliably provide measures of remyelination and repair (Nathoo et al., 2014a).

Recently a new procedure for lysolecithin injection which uses a glass capillary instead of a needle for the injection has been described (Keough et al., 2015). This process helps to reduce axonal damage in this model. Much of the data above was obtained in the older lysolecithin model (pre-glass capillary). To the best of our knowledge studies assessing how MRI metrics change during the disease course in this glass capillary model have not been explored. This model is currently being used to develop remyelinating therapies for MS (Keough et al., 2016). Understanding how MRI parameters change during the disease course of this model will allow us to add these metrics as outcome measures in this trails. Adding MRI measures to these trials will help provide a better understanding of how these therapeutics will fair in clinical trials, where MRI is one of the primary tools used to evaluate the effectiveness of such treatments.

## **1.6 *Ex Vivo* Magnetic Resonance Imaging**

*Ex vivo* MRI can be used to obtain images with a large number of averages and thus a higher signal to noise. However, the effects of chemical fixation and temperature complicate this process. Chemical fixation allows us to keep tissue as "lifelike" as possible by inactivating all biochemical and proteolytic processes and locking structures in space (Huang and Yeung, 2015). The aldehyde group in formaldehyde can react with protein nitrogen, primarily in the basic amino acid lysine, to form a cross-link called a methylene bridge (Kiernan, 2000; Huang and Yeung, 2015). Formaldehyde does not chemically change substances such as carbohydrates, lipids, and nucleic acids. These materials become trapped in a matrix of insolubilized and cross-linked protein molecules. (Kiernan, 2000). If left alone formaldehyde will polymerize to form paraformaldehyde. Methanol and formic acid can be used to prevent

polymerization, but these can have adverse effects on the fixation of tissue. Hence, it is recommended that a fresh formaldehyde solution is made from paraformaldehyde powder and used immediately (Huang and Yeung, 2015).

Regarding MRI, fixation can cause a decrease in  $T_1$  that is greater in gray matter than in white matter resulting in minimal  $T_1$  contrast (Tovi and Ericsson, 1992; D'Arceuil et al., 2007). On the other hand, the drop in white matter  $T_2$  was slightly more than the reduction in gray matter  $T_2$  although there was still a clear gray/white  $T_2$  difference (D'Arceuil et al., 2007). Formalin fixation has been shown to cause a 50% increase in the bound pool fraction ( $f$ ) however this parameter remained well correlated with the myelin content of tissue (Schmierer et al., 2008).

Concerning diffusion, the apparent diffusion coefficient (ADC) values are substantially decreased in *ex vivo* imaging compared to *in vivo* values, with a greater change in white matter than in gray matter (D'Arceuil et al., 2007). A large part of this reduction in ADC and other diffusion parameters is due to brain death and changes in temperature. However, fixation has no effect on anisotropic measures (D'Arceuil et al., 2007).

## Chapter Two: Objectives

### 2.1 Introduction to Objectives

As discussed in Chapter One, a major area of MS research is to develop methods to stimulate remyelination. Drug testing requires animal models, and MRI is one of the primary tools used to evaluate the effectiveness of MS therapeutics (Nathoo et al., 2014b). It follows that *in vivo* drug evaluation in both pre-clinical and clinical trials requires micro-imaging methods suitable for animal use and sensitive to remyelination. This thesis assessed the sensitivity of quantitative magnetization transfer (qMT) and Diffusion tensor imaging (DTI) to remyelination using the lysolecithin model of de- and remyelination. DTI and qMT are key MR methods being assessed for use in studying demyelination in MS patients (Mallik et al., 2014), it follows that they will also be sensitive to remyelination. The lysolecithin model is being used to develop therapies to promote remyelination for the treatment of MS. Data from this thesis will help determine if qMT and DTI can be incorporated into pre-clinical trials as outcome measures. Also, data from this thesis will contribute to informing future clinical trials of MS therapeutics. We expect to see an increase in the bound pool fraction when there is a decrease in myelin. This is because as myelin decreases the amount of protons bound to macromolecules will also decrease, as a number of these protons exist in the lipids that compose myelin. This hypothesis is based on previous work done in the cuprizone model (Thiessen et al., 2013; Turati et al., 2015) and post mortem MS tissue (Schmierer et al., 2007a). We also expect to see an increase in radial diffusion and decrease in fractional anisotropy as myelin decreases. This is because as myelin decreases diffusion orthogonal to the primary direction will become easier increasing radial diffusivity and decreasing fractional anisotropy. Additionally, axonal damage will lead to a greater difficulty of diffusion in the primary direction decreasing axial diffusivity. This hypothesis is

based on previous work done in the cuprizone model (Thiessen et al., 2013) and post mortem MS tissue (Schmierer et al., 2007b).

## **2.2 Aim 1:**

To correlate quantitative magnetization transfer parameters to myelin and axonal content of lysolecithin lesions found histologically.

### ***2.2.1 Hypothesis:***

The bound pool fraction will have a positive correlation to the myelin content in lysolecithin lesions.

## **2.3 Aim 2:**

To correlate diffusion tensor imaging parameters to myelin and axonal content of lysolecithin lesions found histologically.

### ***2.3.1 Hypothesis:***

The radial diffusivity will negatively correlate with, and fractional anisotropy will positively correlate with tissue myelin content. Axial diffusivity will positively correlate to the axonal content in lysolecithin lesions.

## Chapter Three: Materials and Methods

### 3.1 Study Design Summary

#### 3.1.1 Aim 1

Female C57Bl/6 mice from Charles-River were used. Animals received a lysolecithin injection in the thoracic spinal cord ventral white matter. They were sacrificed and perfusion fixed at 7 (peak demyelination) and 14 (early remyelination) days post injection (dpi). Naïve animals without any injections were used as controls. Spinal cords were imaged *ex vivo* using a 9.4T Avance Bruker MRI. The sequences used for qMT include a *Rapid Acquisition with Relaxation Enhancement – Variable Time to Repeat* (RARE-VTR) and *Fast Low Angle Shot* (FLASH) images. The qMT parameters, including bound pool fraction, were found using the two pool model with continuous wave approximation (Henkelman et al., 1993; Ramani et al., 2002). Mean values for each parameter were compared at the different time points using regions of interest around the lesion site and in white matter contralateral to the lesion site. Cords were stained for MBP (myelin marker) and SMI312 (axon marker). The percent staining of the two markers within the lesion area was assessed and correlated to qMT parameters.

#### 3.1.2 Aim 2

Naïve and 7 and 14 dpi *ex vivo* lysolecithin lesions were imaged using an echo planner imaging sequence (EPI). These images were used to calculate the diffusion tensor and to find DTI imaging parameters. We then looked for correlations between the DTI parameters and the percent staining of MBP and SMI312 within the lesion area.

Images were analyzed using ImageJ, MATLAB, and MedINRIA software.

## 3.2 Detailed Materials and Methods

### *3.2.1 Lysolecithin Induced Demyelination*

Experiments in this thesis were approved by the Animal Care Committee of the University of Calgary. Animals used in this thesis were cared for in accordance with the Canadian Council on Animal Care guidelines.

The lysolecithin injection procedure used has been described in detail previously (Keough et al., 2015). 8-10 week old female C57BL/6 mice (Charles-Rivers) were anesthetized with an intraperitoneal injection of ketamine (200mg/kg) and xylazine (10mg/kg) solution. Once anesthetized the animals were prepared for surgery by shaving the dorsal side of the animal, close to the ears. The area was then wiped with 70% ethanol, and iodine was used to disinfect the area. The mice were given a subcutaneous injection of 40 $\mu$ l of bupomorphine, an analgesia, before surgery.

Mice were then placed in a stereotactic frame, dorsal side up. The arms and tail were fastened in place using surgical tape, and the head was held in place using a tooth clamp. A 3 cm midline incision was made, starting just below the ears and cutting towards the tail. The prominent outgrowth of the thoracic (T) 2 vertebra, a characteristic feature of C57BL/6 mice, was located. Spring scissors were used to perform a blunt dissection of the overlying musculature to visualize T2 and forceps were used to feel for the hard surfaces of T3 and T4. Once the proper anatomical location was confirmed shallow lateral cuts were made to the connective tissue between T3 and T4 were made. A laminectomy was not required due to the natural spacing between the vertebrae in the upper thoracic portion of the mouse vertebral column.

Once the correct location was found, and the spinal cord was visualized via removal of overlying connective tissue, 0.5 $\mu$ L of a 1% solution of lysolecithin dissolved in 1 x phosphate buffered saline (PBS) was injected into the ventral column of the spinal cord to induce demyelination. The injection was done using

a pre-pulled glass capillary attached to the arm of a stereotactic micromanipulator. Mice were then removed from the stereotactic device, and the incision site was closed with sutures.

### ***3.2.2 Tissue Fixation and Preparation for Imaging***

Animals were perfused with 10mL of 1x PBS followed by 10mL of 4% paraformaldehyde (PFA) 7 (n=7) and 14 (n=7) days post injection (dpi). Naive mice (n=5) were used as controls. Spinal cords were removed and stored in a 4% PFA solution for 24 hours and following which they were transferred to a 30% sucrose solution for at minimum 72 hours. Spinal cords were placed in a 1 x PBS solution to wash out the fixative and sucrose for 72 to 84 hours before imaging (Dula et al., 2010).

### ***3.2.3 MRI Acquisition***

All MRI Sequences were done on a 9.4T Bruker Avance console. FLASH-scouts and RARE-T2 weighted (RARE-T2w) images were acquired to locate the lesion. The parameters for these sequences can be found below. RARE-VTR images were used to calculate  $T_1$  and FLASH qMT images were used to calculate qMT parameters. EPI were acquired and used to calculate DTI parameters. The specific parameters for each image sequence can be found below.

Two separate qMT sequences are used in the following chapters. The first sequence used a 35mm volume coil. The FLASH-scouts were acquired with the following parameters: matrix=256x256, FOV=1.5x1.5cm, TE/TR/ $\alpha$ =4ms/200ms/30°, and a number of excitations (NEX) =7, and voxel size=59x59x1000 $\mu$ m. The RARE-T2w images, RARE-VTR images and the FLASH qMT images were all acquired with a matrix=128x128, FOV=1.25x1.25cm, and slice thickness of 0.56mm resulting in a resolution of 98x98x560 $\mu$ m. The particular RARE-T2w imaging parameters were: TE/TR/ $\alpha$ =16/2000ms/180°,

NEX=10, RARE Factor=8. The specific RARE-VTR parameters were: TE/ $\alpha$ =11ms/180°, and TR's=100,300,700,1400,5000ms, NEX=8, RARE factor=2. Finally, the FLASH qMT images were acquired with the following parameters: TE/TR/ $\alpha$ =6/70ms/10°, NEX=32. One FLASH qMT image was obtained without ( $M_0$ ) off-resonance saturation, and 18 were acquired with ( $M_{sat}$ ) off-resonance saturation. The off-resonance saturation was  $M_{sat}$  images included RF amplitudes of 5, 10, 20 $\mu$ T each at frequencies of 1000, 2000, 4000, 6000, 10000, and 30000 Hz (Thiessen et al., 2013).

The second qMT sequence used was run with a Bruker cryoprobe. This coil is helium cooled. The low temperature of the coil decreases random thermal motion of electrons in the conductor thus reducing the noise in images. For these images the FLASH-scout images had the following parameters: matrix=256x256, FOV=2.0x2.0cm, TE/TR/ $\alpha$ =4ms/500ms/45°, and NEX=1, and resolution=78x78x1000 $\mu$ m. The RARE-T2w images, RARE-VTR images and the FLASH qMT images were all acquired with a matrix=128x128, FOV=1.25x1.25cm, and slice thickness 500 $\mu$ m resulting in a resolution of 98x98x500 $\mu$ m. The specific RARE-T2w imaging parameters were: TE/TR/ $\alpha$ =16/2500ms/180°, NEX=1, RARE Factor=8. The specific RARE-VTR parameters were: TRs=95.5,295.5,695.5,1395.5, 4895.5ms, NEX=2, RARE factor=2. Finally, the FLASH qMT images were acquired with the following parameters: TE/TR/ $\alpha$ =6/70ms/10°, NEX=7. The  $M_{sat}$  images were acquired with the same off-resonance pulses as were used with the volume coil.

Diffusion weighted EPIs (matrix=128x128, FOV=1.25x1.25cm, TE/TR/ $\alpha$ =36/1000ms, NEX=8, b-values/directions =1400/16 & 2000/20 and voxel size=98x98x500 $\mu$ m) was also acquired using the cryoprobe. These images were used for the DTI analysis.

### 3.2.4 MRI Data Analysis

MR data was analyzed using ImageJ v. 1.47 and MATLAB 7.7.0 software.

#### 3.2.4.1 $T_1$

RARE-VTR  $T_1$  maps were generated by fitting RARE-VTR images to a saturation recovery curve using MATLAB software provided by Dr. Melanie Martin (Thiessen et al., 2013). Regions of interest around the lesion site and contralateral to the lesion site were drawn on the RARE  $T_1$  weighted image with the longest TR and imported onto the  $T_1$  maps. These were used to find the mean  $T_1$  for the two regions of interest.

#### 3.2.4.2 Quantitative Magnetization Transfer

FLASH-qMT images were normalized to the  $M_0$  image and fit to the two-pool model of magnetization transfer (Henkelman et al., 1993) with continuous wave pulse equivalent approximations (Ramani et al., 2002) and a super-Lorentzian absorption line shape for the bound pool (Thiessen et al., 2013). For the peak RF amplitudes of 5, 10, and 20  $\mu\text{T}$ , the amplitudes of the continuous wave power equivalents ( $\omega_{1\text{CWPE}}$ ) are 279.7, 559.5, and 1119 rad/s, respectively (Thiessen et al., 2013). Relevant metrics of the two pool model include: magnetization transfer rate between the free and bound pools ( $R$ ), longitudinal relaxation rate of the free ( $R_{1A}$ ) and bound ( $R_{1B}$ ) pools, transverse relaxation rate of the free ( $T_2^A$ ) and the bound ( $T_2^B$ ) pool, and the bound pool fraction ( $f$ ). Several groups have recommended that  $R_B$  is fixed to  $1/s$  (Henkelman et al., 1993; Morrison and Henkelman, 1995; Quesson et al., 1997; Graham and Henkelman, 1999). By fitting the observed signal at various off-resonance frequencies and amplitudes to the equation below, we can find  $R$ ,  $1/R_A T_2^A$ ,  $T_2^B$  and  $f/R_A(1-f)$  (Ramani et al., 2002):

$$\frac{M_z^A}{M_0^A} = g \left( \frac{R_{1B} \left( \frac{RM_0^A f}{R_{1A}(1-f)} \right) + R_{RFB} + R_{1B} + RM_0^A}{\left( \frac{RM_0^A f}{R_{1A}(1-f)} \right) (R_{1B} + R_{RFB}) + \left( 1 + \left[ \frac{\omega_{CWPE}}{2\pi\Delta f} \right]^2 \left[ \frac{1}{R_{1A}T_2^A} \right] \right) (R_{RFB} + R_{1B} + RM_0^A)} \right)$$

In this equation  $M_z^A/M_0^A$  is the normalized signal intensity,  $g$  = a scaling factor including the gain of the RF amplifier,  $M_0^A$  = fully relaxed value of the free pool,  $R_{RFB}$  = is the rate of loss of longitudinal magnetization by the bound pool, and  $\Delta f$  = the off-resonance frequency. Once  $R_{1B}$ ,  $R M_0^A$  and  $f/R_{1A}(1-f)$  are known, and by determining  $R_{1A}^{obs}$  using the  $T_1$  maps ( $R_{1A}^{obs} = 1/T_1$ ), we can find the  $R_{1A}$  using the equation below (Ramani et al., 2002):

$$R_{1A} = \frac{R_A^{obs}}{1 + \left( \frac{\frac{RM_0^A f}{(1-f)R_{1A}} (R_{1B} - R_A^{obs})}{(R_{1B} - R_A^{obs}) + RM_0^A} \right)}$$

Once  $R_{1A}$ ,  $f/R_{1A}(1-f)$  and  $1/R_{1A}T_2^A$  are known, the values for  $f$  and  $T_2^A$  can be determined (Ramani et al., 2002).

These calculations were performed using MATLAB software provided by Dr. Melanie Martin (Thiessen et al., 2013).

### 3.2.4.3 Diffusion Tensor Imaging

Echo planar diffusion weighted images were used to calculate the effective diffusion tensor,  $\underline{D}$ , of each voxel (Basser et al., 1994a; Basser and Jones, 2002). Diagonalization of the diffusion tensor provides us with the

eigenvectors and eigenvalues,  $\lambda$  (Basser et al., 1994b; Le Bihan et al., 2001). These eigenvectors and eigenvalues can be represented as 3-dimensional diffusion ellipsoids as mentioned in Chapter One. The principal axis of the ellipsoid gives the main direction in the voxel coinciding with the direction of the fibers and the first eigenvector/value ( $\lambda_1$ ). The second two eigenvectors ( $\lambda_2, \lambda_3$ ) are perpendicular to the primary eigenvector.

Using the eigenvectors and eigenvalues we found the axial diffusion ( $\lambda_1$ ), radial diffusion ( $(\lambda_2 + \lambda_3)/2$ ) and mean diffusion ( $(\lambda_1 + \lambda_2 + \lambda_3)/3$ ) (Neil, 2008). The fraction of the 'magnitude' of  $\underline{D}$  that can be ascribed to anisotropic diffusion, or the fractional anisotropy (FA) was calculated using the eigenvectors and eigenvalues as shown below (Le Bihan et al., 2001):

$$FA = \frac{\sqrt{3[(\lambda_1 - \langle\lambda\rangle)^2 + (\lambda_2 - \langle\lambda\rangle)^2 + (\lambda_3 - \langle\lambda\rangle)^2]}}{\sqrt{2(\lambda_1^2 + \lambda_2^2 + \lambda_3^2)}}$$

Where  $\langle\lambda\rangle$  is equal to the mean diffusion (Le Bihan et al., 2001).

Fractional anisotropy was separated into three cases depending on the shape of the ellipsoid (Westin et al., 1999). The first case is called the linear case (CL), also known as linear anisotropy. This case occurs when diffusion mainly corresponds to the direction of the  $\lambda_1$ , in other words in this case diffusion is primarily linear ( $\lambda_1 \gg \lambda_2 \approx \lambda_3$ ). For this case,

$$CL = \frac{\lambda_1 - \lambda_2}{\lambda_1 + \lambda_2 + \lambda_3}$$

The second case is the planar case (CP), also known as planar anisotropy. This case occurs when diffusion in the directions of  $\lambda_1$  and  $\lambda_2$  are about equal, in other words, diffusion is primarily planar ( $\lambda_1 \approx \lambda_2 \gg \lambda_3$ ). For this case,

$$CP = \frac{2(\lambda_2 - \lambda_3)}{\lambda_1 + \lambda_2 + \lambda_3}$$

Finally, the third case is the spherical case (CS), also known as spherical anisotropy. This case occurs when diffusion in the directions of  $\lambda_1$ ,  $\lambda_2$ , and  $\lambda_3$  is about equal, in other words, diffusion is primarily spherical ( $\lambda_1 \approx \lambda_2 \approx \lambda_3$ ). For this case,

$$CS = \frac{3(\lambda_3)}{\lambda_1 + \lambda_2 + \lambda_3}$$

(Westin et al., 1999).

Two other parameters that were found from the diffusion tensor analysis include relative anisotropy (RA) and the volume ratio (VR). The RA is a normalized standard deviation that represents the ratio of the anisotropic part of the effective diffusion tensor to its isotropic part (Le Bihan et al., 2001). It was calculated using the equation below:

$$RA = \frac{\sqrt{[(\lambda_1 - \langle\lambda\rangle)^2 + (\lambda_2 - \langle\lambda\rangle)^2 + (\lambda_3 - \langle\lambda\rangle)^2]}}{\sqrt{3\langle\lambda\rangle}}$$

Where  $\langle\lambda\rangle$  is equal to the mean diffusion (Le Bihan et al., 2001).

Finally, VR represents the ratio of the ellipsoid volume to the volume of a sphere with the radius of the mean diffusion. It was calculated using the equation below (Le Bihan et al., 2001):

$$VR = \frac{\lambda_1\lambda_2\lambda_3}{\langle\lambda\rangle^3}$$

It should be noted that while FA and RA both range from 0 (isotropic diffusion) to 1 (anisotropic diffusion), VR ranges from 1 (isotropic diffusion) to 0 (anisotropic diffusion) (Le Bihan et al., 2001).

The above calculations were done using MedINRIA 1.9.2.0.

#### 3.2.4.4 Statistics

All sets of data were tested for normal distribution using a Shapiro-Wilk normality test. An equal variance test was used to see if the different groups had equality of variance. One-way analysis of variance (ANOVA) with a Tukey's posthoc tests was used to compare the naïve, ventral white matter contralateral to the lesion, 7 day and 14 day post injection lesions (dpi) data unless otherwise stated. For all statistical tests,  $p \leq 0.05$  was considered significant. These analyses were run using Sigma plot software. Correlations between MRI parameters were found using a Spearman's correlation test.

### ***3.2.5 Histology***

#### 3.2.5.1 Sectioning and Staining

After MR imaging the cords were placed in a 20% sucrose solution. Next, they were switched to a 30% sucrose solution 24 hours before freezing. When ready for freezing, three cords were placed together in a rectangular container and covered with the optimum cutting temperature (OCT) formulation. The container was then placed on the cryostat freezing panel.

Once frozen the container was removed, and the OCT block was gently removed from the container. Tissue was then placed on a sectioning block and sectioned axially at 20 $\mu$ m and mounted on slides. Slides were kept frozen until 30 minutes before staining.

The tissue sections were defrosted and dried for 30 minutes. They were stained for Myelin basic protein (MBP) and SMI312 which were used as myelin

and axons markers, respectively. MBP is a component of myelin proteins essential for myelin compaction and stability and is frequently used as an index of myelination. Decreased expression of MBP indicates a reduced number of myelinating oligodendrocytes (Azin et al., 2015). SMI312 is an antibody directed against highly phosphorylated epitopes of neurofilament (Ulfig et al., 1998).

First, the sections underwent delipidation via placement in progressively increasing and then decreasing concentrations of ethanol for one minute each. The concentrations used were: 50%, 70%, 90%, 95%, and 100% ethanol. Following this tissue was blocked with 10% horse serum containing 1% bovine serum albumin and 0.1% cold fish skin gelatin. Tissue was then incubated overnight with the primary antibodies (1:1000 rabbit MBP and 1:2000 Mouse SMI312) diluted in antibody buffering solutions at 4°C. The next day tissue was washed three times with 0.05% Tween 20 in 1xPBS for 5 minutes per wash. Next, tissue was incubated with the secondary antibodies (AF488 donkey anti-rabbit and AF594 donkey anti-mouse) for 1 hour at room temperature. Finally, slides were once more washed three times in 0.05% Tween 20 in 1xPBS for 5 minutes per wash before mounting with Immuno-Mount (ThermoScientific, Canada).

#### 3.2.5.2 Co-Registration

Once stained, sections were imaged using confocal microscopy. An example schematic explaining how lesions were co-registered to MRI images can be found on the next page (**Figure 3.5**).

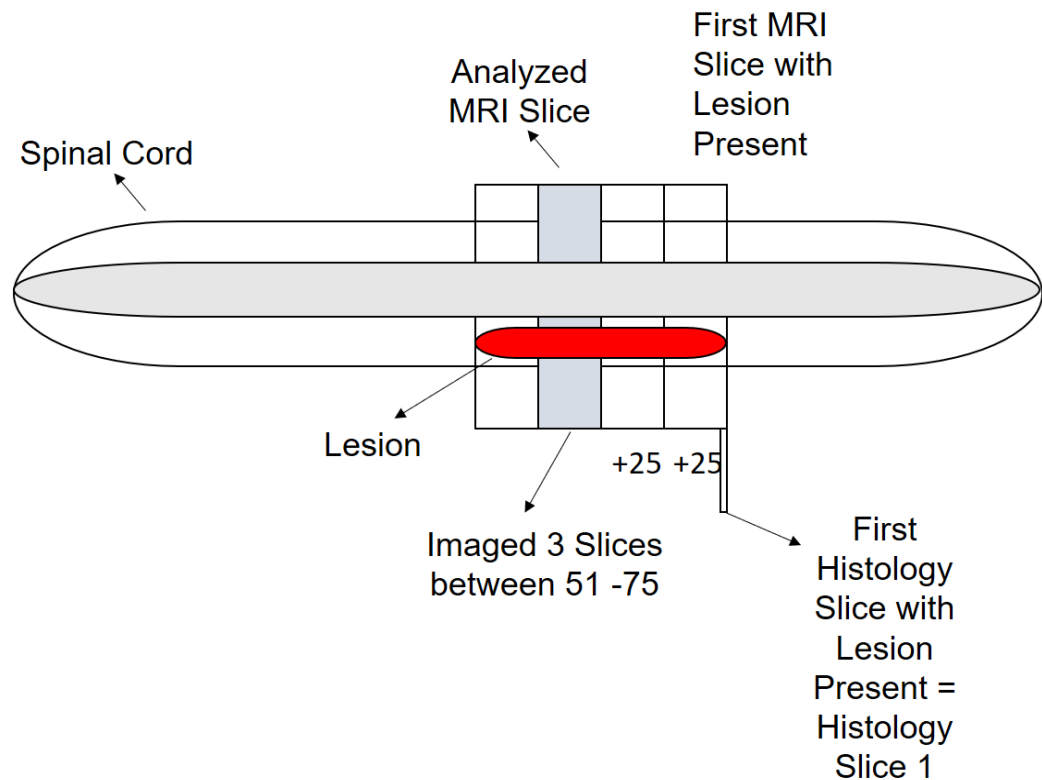


**Figure 3.5: Schematic illustration of MR and microscopy co-registration method.** To begin, we found the first MRI slice in which the lesion was present. We called this MRI slice 1. Next, we determined how many MRI slices away the analyzed slice was from MRI slice 1. We then found the first histology slice in which the lesion appeared and called this histology slice 1. Then knowing that 25 histology slices = 1 MRI slice we were able to determine which range of histology slices correspond to the MR images. Finally, three histology slices within the range found were then imaged using a confocal microscope. In the example above the analyzed MRI slice is three slices away from MRI slice 1. Thus the histology slices that correspond to the MRI slice are 50-74 slices away from histology slice 1.

### 3.2.5.3 Analysis

The percent of the lesion area occupied by MBP rings was found on ImageJ using a 'thresholding' method. The lesion perimeter was manually traced, and the area outside the lesion was cleared (**Figure 3.6A, B**). We then measured the number of pixels in the lesion area (LA). Next, thresholding was used to eliminate background staining in the region of interest, leaving only the area taken up by stained MBP myelin rings (**Figure 3.6C, D**). We then measured the number of pixels in the thresholded area (i.e. pixels stained by MBP) (T). Next, we found the percent MBP staining by taking the MBP pixels (T) and dividing by the lesion pixels (LA) and multiplying by 100 (**Figure 3.6E**). The percent of the lesion area occupied by MBP rings was used as a measure of myelin content in the lesion site.

The percent of the lesion area occupied by SMI312 was calculated the same way as the percent MBP staining. The lesion area was traced in the MBP stained images imported onto the SMI312 images, and then thresholding was done in the same way described above.

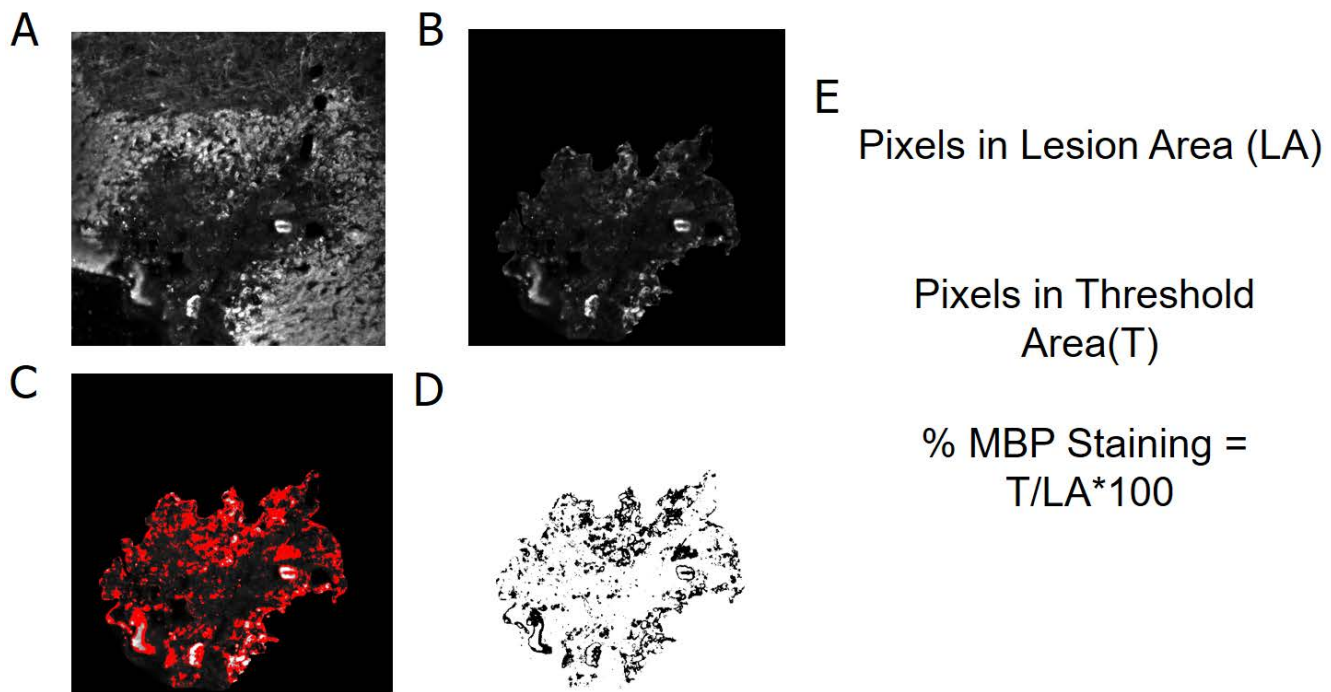


**Figure 3.5: Illustration of method used to find percent MBP staining and percent SMI312 staining.** **A:** Lesion was traced. **B:** Area outside the lesion was cleared, and the number of pixels in the lesion area was determined. **C:** Thresholding was used to highlight the MBP staining. **D:** When thresholding was applied the pixels occupied by MBP became black, and the rest of the pixels turned white. The pixels that were thresholded were then found. **E:** The calculation used to find the % MBP staining.

#### 3.2.5.4 Statistics

All sets of histology data were tested for normal distribution using a Shapiro-Wilk normality test. An equal variance test was used to see if the different groups had equality of variance. One-way analysis of variance (ANOVA) with a Tukey's posthoc tests were used to compare the naïve, ventral white matter contralateral to the lesion, 7 day and 14 day post injection lesions (dpi) data unless otherwise stated. For all statistical tests  $p \leq 0.05$  was considered significant. These analyses were run using Sigma plot software. Correlations between histology and MRI parameters were found using a Spearman's correlation test.

## Chapter Four: Development of Quantitative Magnetization Transfer Sequence and Analysis

### 4.1 Results

#### *4.1.1 Quantitative Magnetization Transfer Parameters can be Calculated using the Volume Coil or Cryoprobe*

The qMT sequences and analysis employed in this study were based on that used in a 2013 paper by Dr. Jonathan Thiessen (Thiessen et al., 2013). To test this sequence and analysis, we obtained data on 2 and 4% agarose phantoms. The qMT sequence was tested using two separate coils, the volume coil and the cryoprobe (n=3, for both). The qMT data obtained on the two phantoms with each coil are presented on the following page alongside literature values for reference. The measured values of bound pool fraction (f), the calculated rate of relaxation of the liquid pool ( $R_{1A}$ ) and experimentally observed rate of relaxation of the liquid pool ( $R_{1}^{obs}$ ) were all near or within the range of values previously reported in the literature. The  $T_2$  values of the liquid pool ( $T_2^A$ ) and bound pools ( $T_2^B$ ) were higher and lower, respectively, compared to values previously reported in the literature (**Table 4.1**).

**Table 4.1: Quantitative Magnetization Transfer parameters of agar gel phantoms.** Literature values reported by Sled & Pike, 2001 for a pulsed magnetization transfer experiment and Henkelman et al., 1993 for a continuous wave magnetization transfer experiment are also reported. Mean $\pm$ SD.

	Parameter	f	R <sub>1A</sub> (s <sup>-1</sup> )	R <sub>1B</sub> (s <sup>-1</sup> )	T <sub>2</sub> <sup>A</sup> (ms)	T <sub>2</sub> <sup>B</sup> ( $\mu$ s)	R <sub>1</sub> <sup>obs</sup> (s <sup>-1</sup> )
<b>2% Agar</b>	Experimental Data (Cryoprobe) n=3	0.0069 $\pm$ 0.0007	0.43 $\pm$ 0.005	1.0 $\pm$ 0.0	120 $\pm$ 8	6.7 $\pm$ 0.4	0.44 $\pm$ 0.006
	Experimental Data (Volume Coil) n=3	0.0055 $\pm$ 0.0004	0.31 $\pm$ 0.02	1.0 $\pm$ 0.0	121 $\pm$ 11	5.2 $\pm$ 0.7	0.31 $\pm$ 0.02
	Pulsed Magnetization Transfer Experiment (Sled and Pike, 2001)	0.0066 $\pm$ 0.0004	0.42 $\pm$ 0.02	1.0 $\pm$ 0.0	56.4 $\pm$ 3	14.3 $\pm$ 0.5	0.42 $\pm$ 0.009
	Continuous Wave Experiment (Henkelman et al., 1993)	0.0051 $\pm$ 0.001	0.51 $\pm$ 0.07	1.0 $\pm$ 0.0	63 $\pm$ 8	12.9 $\pm$ 0.1	0.49 $\pm$ 0.02
<b>4% Agar</b>	Experimental Data (Cryoprobe) n=3	0.016 $\pm$ 0.0001	0.44 $\pm$ 0.006	1.0 $\pm$ 0.0	48 $\pm$ 0.009	6.5 $\pm$ 0.06	0.45 $\pm$ 0.006
	Experimental Data (Volume Coil) n=3	0.011 $\pm$ 0.0001	0.34 $\pm$ 0.03	1.0 $\pm$ 0.0	60 $\pm$ 2	4.8 $\pm$ 0.16	0.33 $\pm$ 0.03
	Pulsed Magnetization Transfer Experiment (Sled and Pike, 2001)	0.012 $\pm$ 0.002	0.48 $\pm$ 0.1	1.0 $\pm$ 0.0	34 $\pm$ 2	14.1 $\pm$ 0.3	0.49 $\pm$ 0.05
	Continuous Wave Experiment (Henkelman et al., 1993)	0.011 $\pm$ 0.002	0.70 $\pm$ 0.10	1.0 $\pm$ 0.0	32 $\pm$ 2	12.9 $\pm$ 0.1	0.68 $\pm$ 0.03

#### ***4.1.2 Quantitative Magnetization Transfer of Lysolecithin Lesions using the Cryoprobe or Volume Coil***

Once we verified our ability to estimate some qMT parameters reliably, a qMT sequence was run on 7-day post injection (dpi) lysolecithin cords using both the volume and cryoprobe.

The signal to noise was calculated by taking the signal of a region of interest and dividing by the standard deviation of the background. Regions of interest used for the signal to noise calculation were drawn in the agar medium in which the cords were embedded. The cryoprobe, unsurprisingly, had a higher signal to noise for all image types obtained (**Table 4.2**).

Lesions were visible on FLASH-Scout images. Visually the  $T_1$  appears to be higher (whiter) on the  $T_1$  map and  $f$  seems to be lower (darker) on the bound pool fraction map at the lesion site for both coils (**Figure 4.1**).

Statistically, the mean  $T_1$  was found to be significantly longer at the lesion site compared to the contralateral region of interest regardless of coil used (volume coil:  $n=5$ ; cryoprobe:  $n=3$ ;  $p=0.01$  for both coils). The  $f$  was not found to be significantly different when using the volume coil ( $p=0.18$ ), but it was found to be significantly lower at the lesion site compared to contralateral white matter when using the cryoprobe ( $p=0.004$ ) (**Figure 4.2**).

The  $T_2^A$  and  $T_2^B$  were not found to be significantly different regardless of coil used (**Figure 4.3**).

**Table 4.2: The signal to noise ratio of volume and cryoprobe images.**

The regions of interest used for the calculations were made in the agar gel in which the lysolecithin spinal cords were embedded. Volume coil means were obtained from 5 separate imaging sessions, and cryoprobe means come from 3 different imaging sessions. RARE-VTR signal to noise was calculated on the 3<sup>rd</sup> TR image. FLASH qMT signal to noise was calculated on the image without off-resonance radio frequency pulses. CV = coefficient of variation. Mean±SD

Image Type	Signal to Noise			
	Volume Coil		Cryoprobe	
	(Mean±SD)	CV	(Mean±SD)	CV
FLASH-Scout	43±3	0.07	273±147	0.54
RARE-VTR	18±4	0.22	128±54	0.42
FLASH qMT	51±2	0.04	166±16	0.10

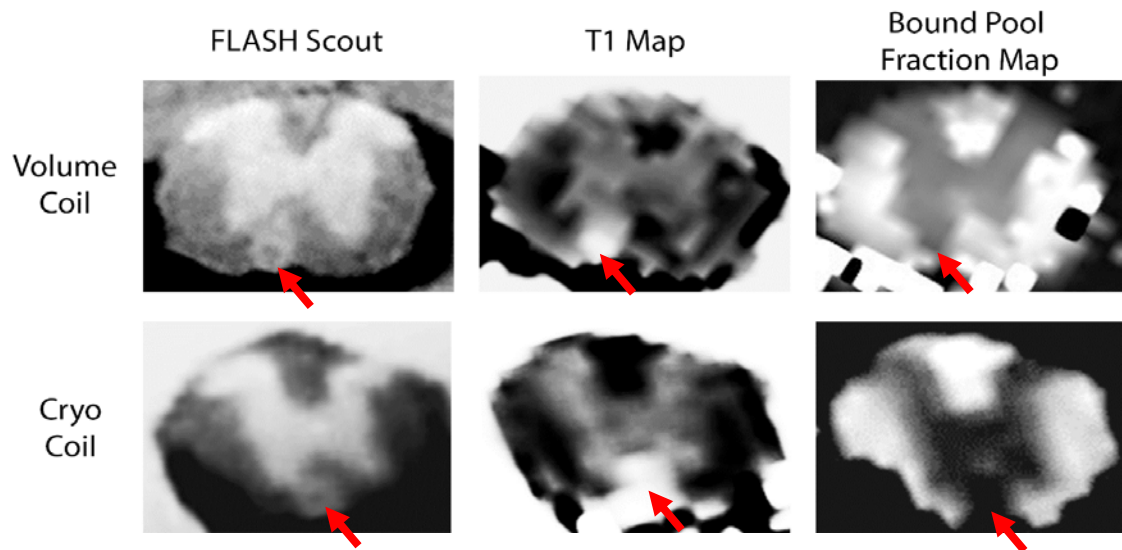


**Figure 4.1: Representative FLASH-Scout images with corresponding  $T_1$  maps and bound pool fraction ( $f$ ) maps for the volume coil and cryoprobe.** Lesions are visible on FLASH-Scout images.  $T_1$  appears higher (whiter) and  $f$  seems lower (darker) at the lesion for both coils. Lesion indicated by red arrows.

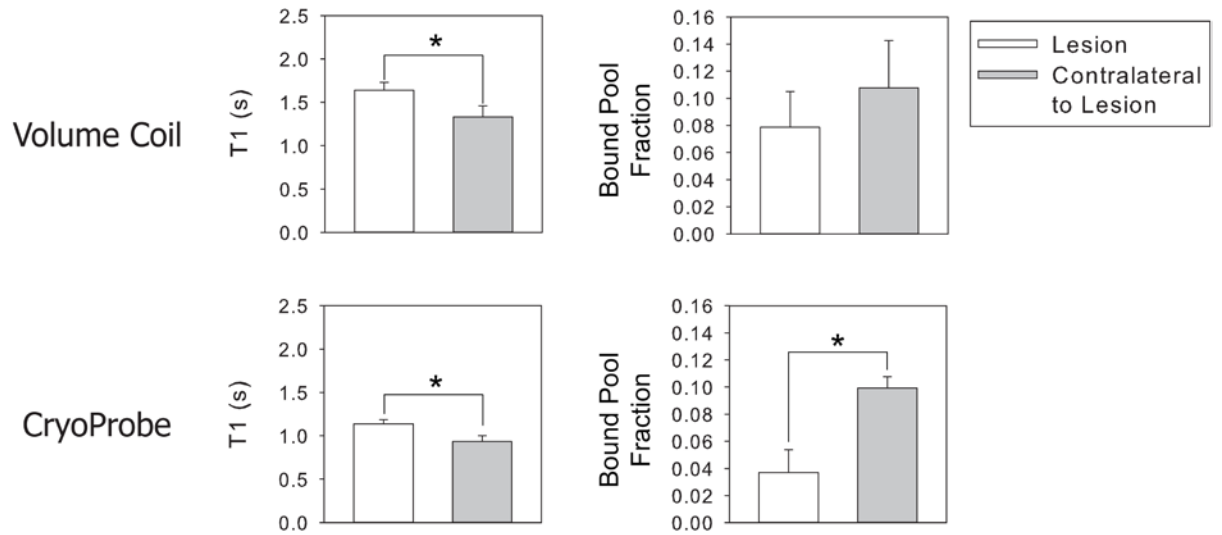


**Figure 4.2: T<sub>1</sub> and bound pool fraction at the lesion and contralateral sites.** T<sub>1</sub> was significantly higher at the lesion site regardless of the coil. The f was not significantly lower at the lesion when using the volume coil (n=5) but was when using the cryoprobe (n=3). t-tests were used to test for significance. Mean±SD. \* ≤0.05

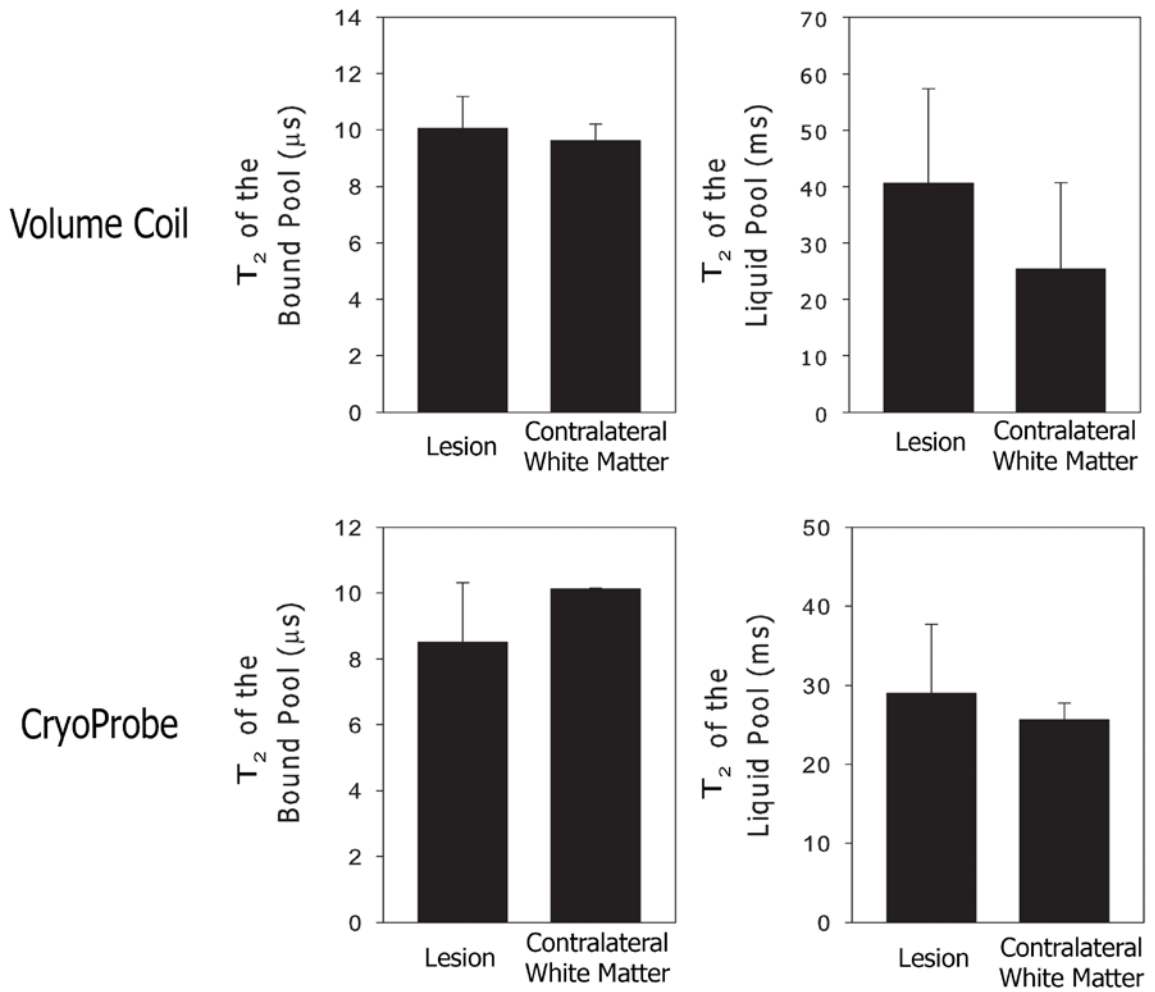


**Figure 4.3: T<sub>2</sub> of Liquid and bound pools at the lesion and contralateral sites.** T<sub>2</sub> of both pools was not significantly different at the lesion site regardless of coil used (n=3 cryoprobe; n=5 volume coil). T-tests were used to test for significance. Mean±SD.

## 4.2 Discussion

### *4.2.1 Validation of the Quantitative Magnetization Transfer Sequence*

To begin, we were able to demonstrate that the qMT sequence and analysis used in this study can reproducibly calculate the bound pool fraction ( $f$ ) and the longitudinal relaxation rate of the liquid pool ( $R_{1A}$ ), for both the cryoprobe and volume coil. The  $f$  and  $R_{1A}$  values found in the phantom experiments were within range of those previously reported in the literature (Henkelman et al., 1993; Sled and Pike, 2001). The  $T_2$  of the liquid ( $T_2^A$ ) and bound pools ( $T_2^B$ ) seen in the phantom experiments were higher and lower, respectively than those previously reported in the literature for both coils (Henkelman et al., 1993; Sled and Pike, 2001). This result may be due to the of the different models used to calculate these values. The phantom studies reported in literature used pulsed magnetization Transfer (Sled and Pike, 2001) and a continuous wave (Henkelman et al., 1993) models for their calculations. The experiments reported here used a continuous wave approximation model. The values for  $T_2^A$  and  $T_2^B$  of naïve white matter found in this study are within range of those reported for control cuprizone mice by Thiessen et al., 2013. The Thiessen study used the same model and analysis software that is used to calculate magnetization transfer here (Thiessen et al., 2013).

Next, we imaged 7 dpi lesions with two different coils, a quadrature 35mm volume coil, and a surface cryoprobe. We found that both coils were able to detect the higher  $T_1$  in the lesion area. Although it has been shown that  $f$  has a stronger correlation to the myelin content of tissue than the  $T_1$  (Thiessen et al., 2013) using the volume coil we failed to detect any changes to  $f$ . However, when we used the cryoprobe, which has a higher signal to noise, and imaged the same cords we discovered a significantly lower  $f$  at the lesion site. Our inability to detect this difference in  $f$  when using the volume coil may because of its lower signal to noise causing a higher variability in the  $f$  compared to the cryoprobe.

Due to the increase in signal to noise provided by the cryoprobe we used it for all further experiments. Additionally, the use of the cryoprobe allowed us to shorten our acquisition time.

### **4.3 Conclusions**

This chapter shows data from phantom experiments and preliminary experiments with 7 dpi lysolecithin lesions using two different RF coils. We show that the Bruker cryoprobe provides more consistent results for qMT in WM lesions in *ex vivo* spinal cord imaging. Our qMT protocol provides data similar to that reported in the literature. This development chapter shows that we now have a protocol which is reproducible for studying qMT in *ex vivo* cords.

## Chapter Five: T1 and Quantitative Magnetization Transfer Imaging Parameters correlate with Histological Stains for Myelin and Neurofilament

### Results

#### *5.1.1 Quantitative Magnetization Transfer Parameters and T<sub>1</sub> of Lysolecithin Lesions*

Naïve (n=5), 7 dpi (n=7) and 14 dpi (n=7) cords were imaged and the T<sub>1</sub> and qMT parameters were calculated.

Regions of interest (ROIs) were drawn around the 7 dpi and 14 dpi lesions as well as in the ventral white matter contralateral to the lesion site and in naïve cords. The mean bound pool fraction (f) of 7 dpi lesions ( $0.051 \pm 0.025$ ; mean $\pm$ SD) was found to be significantly lower than naïve ( $0.14 \pm 0.017$ ) ( $p < 0.001$ ), and 7 dpi ( $0.11 \pm 0.037$ ) ( $p = 0.002$ ) and 14 dpi ( $0.11 \pm 0.026$ ) ( $p = 0.002$ ) contralateral regions. The mean 14 dpi lesion f ( $0.060 \pm 0.018$ ) was also significantly lower than naïve ( $p < 0.001$ ), and 7 dpi ( $p = 0.002$ ) and 14 dpi ( $p = 0.008$ ) contralateral region. The mean 7 dpi lesion f were not significantly different from the mean 14 dpi lesion f ( $p = 0.98$ ) (**Figure 5.1A**).

The T<sub>1</sub> was significantly longer at 7 dpi lesions ( $1.38 \pm 0.18$ s) compared to naïve ( $1.13 \pm 0.013$ s) ( $p = 0.012$ ), and 7 dpi ( $1.11 \pm 0.13$ s) ( $p = 0.002$ ) and 14 dpi contralateral ( $1.11 \pm 0.04$ s) ( $p = 0.003$ ) regions. The mean T<sub>1</sub> of 14 dpi lesion ( $1.32 \pm 0.13$ s) was also significantly longer compared to 7 dpi ( $p = 0.02$ ) and 14 dpi ( $p = 0.02$ ) contralateral regions of interest. The mean T<sub>1</sub> was not significantly different between 7 dpi and 14 dpi lesions ( $p = 0.93$ ) or between 14 dpi and naïve cords ( $p = 0.07$ ) (**Figure 5.1B**).

The T<sub>2</sub> of the liquid pool (T<sub>2</sub><sup>A</sup>) and the T<sub>2</sub> of the bound pool (T<sub>2</sub><sup>B</sup>) failed a Shapiro-Wilk test of normality and therefore an ANOVA on ranks with a Dunn's post-hoc test was used to test for significant differences between the groups. The mean T<sub>2</sub><sup>A</sup> was found to be significantly longer at 14 dpi ( $106 \pm 35$ ms) than the naïve T<sub>2</sub><sup>A</sup> ( $51.44 \pm 9.6$ ms) ( $p < 0.05$ ). There were no other significant

differences between groups found (**Figure 5.2A**). There were no significant differences found between the  $T_2^B$  of the different groups (**Figure 5.2B**).

The qMT data of each group was normalized by dividing by the value of the contralateral side (**Figure 5.3**). The naïve group had a significantly higher normalized  $f$  ( $1.00 \pm 0.04$ ) compared to 7 dpi ( $0.47 \pm 0.18$ ) and 14 dpi ( $0.53 \pm 0.09$ ) ( $p < 0.001$  for both comparisons). No significant difference was found between the normalized  $f$  of 7 dpi and 14 dpi lesions ( $p = 0.63$ ) (**Figure 5.3A**).

The naïve group had a significantly lower normalized  $T_1$  ( $1.00 \pm 0.04$ ) compared to 7 dpi ( $1.25 \pm 0.14$ ) ( $p = 0.005$ ) and 14 dpi ( $1.19 \pm 0.10$ ) ( $p = 0.03$ ) (**Figure 5.3B**). No significant difference was found between the normalized  $f$  of 7 dpi and 14 dpi lesions ( $p = 0.59$ ) (**Figure 5.3B**).

The  $T_2^A$  and  $T_2^B$  failed the Shapiro-Wilk normality test and therefore an ANOVA on ranks was used to test for significant differences between groups. There is no significant difference between naïve, 7 dpi lesions and 14 dpi lesions normalized  $T_2^A$  ( $p = 0.14$ ) (**Figure 5.3C**). The naïve group had a significantly higher normalized  $T_2^B$  ( $1.02 \pm 0.05$ ) compared to 14 dpi ( $0.90 \pm 0.04$ ) ( $p < 0.05$ ). Significant differences were not found between 7 dpi normalized  $T_2^B$  ( $0.82 \pm 0.24$ ) and naïve or 14 dpi  $T_2^B$  ( $p > 0.05$ ) (**Figure 5.3D**).

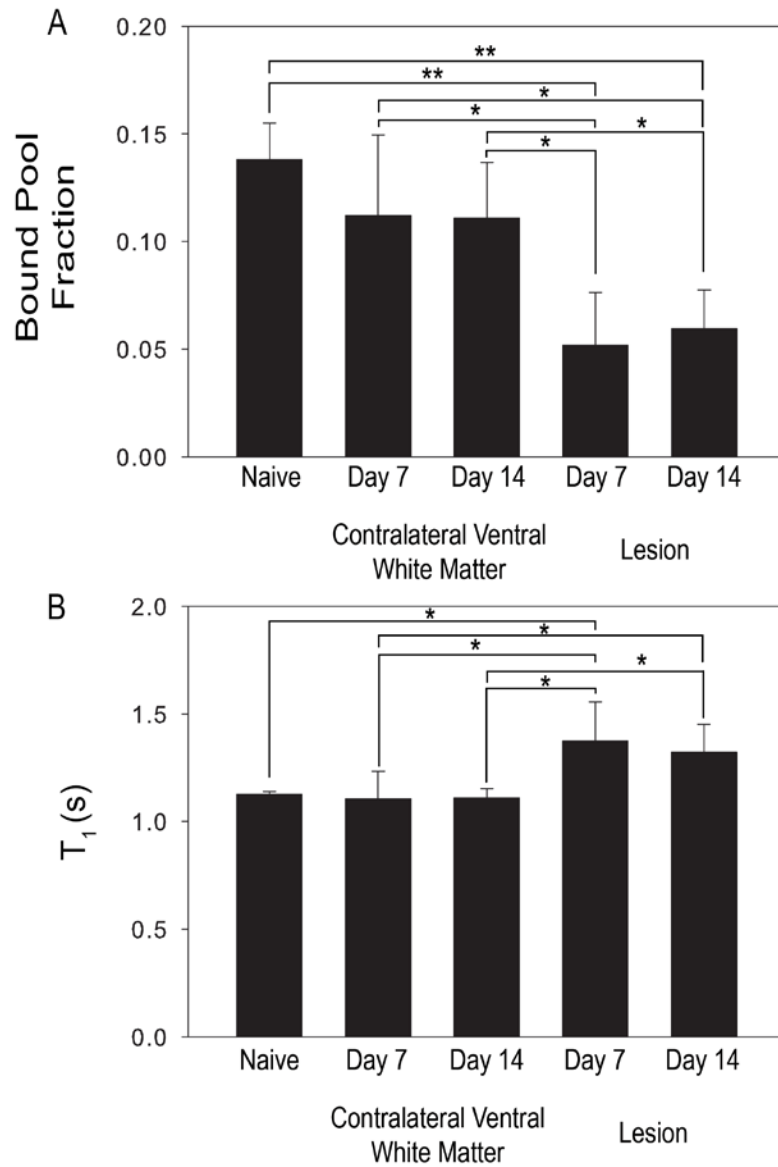


**Figure 5.1: T<sub>1</sub> and bound pool fraction (f) of naïve (n=5), contralateral regions (7dpi n=7; 14 dpi n=7), 7 dpi lesion (n=7) and 14 dpi lesions (n=7).** **A:** The f was significantly lower at 7 dpi and 14 dpi compared to both naïve and contralateral sites. **B:** T<sub>1</sub> was significantly longer at 7 dpi and 14 dpi in the lesion compared to the contralateral regions of interest. A one-way ANOVA with a Tukey's posthoc test was used to test for significant differences between groups. Mean±SD.\* ≤0.05, \*\*<0.001

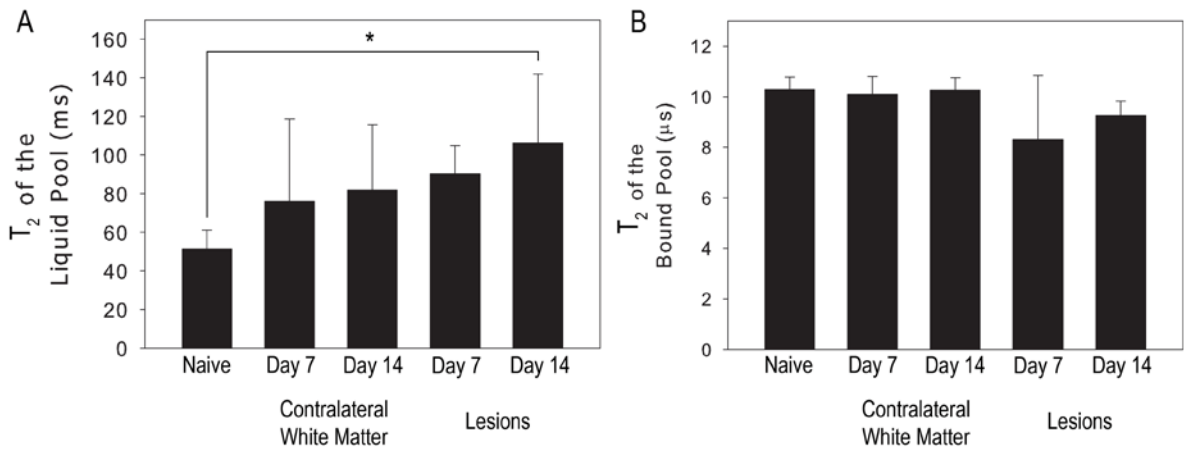


**Figure 5.2: T<sub>2</sub> of the liquid and bound pools of naïve (n=5), contralateral regions (7 dpi n=7; 14 dpi n=7), 7 dpi lesion (n=7) and 14 dpi lesions (n=7).** **A:** The T<sub>2</sub> of the liquid pool was significantly longer at 14 dpi lesions compared to naïve cords. **B:** The T<sub>2</sub> of the bound pool was not significantly different between groups. The data failed a Shapiro-Wilk test of normality and therefore an ANOVA on Ranks with a Dunn's posthoc test was used to check for significant differences between groups. Mean±SD. \* ≤0.05

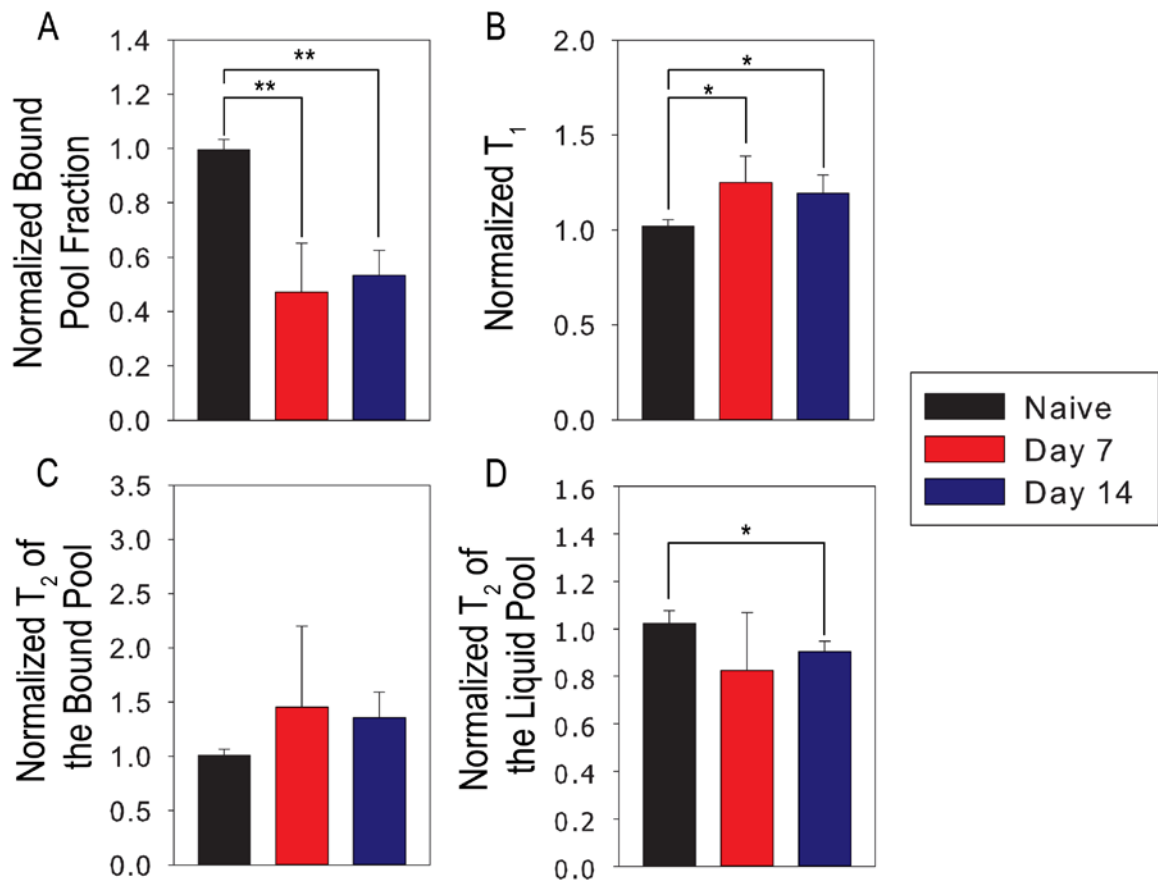


**Figure 5.3: Normalized bound pool fraction,  $T_1$  and  $T_2$  of the liquid and bound pools of 7 (n=7) and 14 (n=7) dpi lesions.** The lesion and naïve data were normalized by dividing by the value of the contralateral side. One-way ANOVAs with a Tukey's posthoc test were used to test for significant differences between groups f and  $T_1$ s. ANOVA on Ranks with a Dunn's posthoc test was used to test for significant differences between groups  $T_2$  of the liquid and bound pools. Mean±SD. \*  $\leq 0.05$ , \*\* $< 0.001$

### ***5.1.2 Quantification of Histological Stains for Myelin and Neurofilament***

Naïve (n=5), 7 dpi (n=5) and 14 dpi (n=6) lesions were stained with SMI312 (neurofilament stain) and myelin basic protein (MBP; Myelin stain) (**Figure 5.4**).

The percent MBP and SMI312 staining within the lesion site, contralateral ventral white matter and ventral white matter of naïve cords were found (**Figure 5.5**). The mean percent MBP staining of 7 dpi lesions ( $15\pm 1\%$ ) is significantly lower than the means of naïve ( $83\pm 2\%$ ), 7 dpi contralateral ( $82\pm 1\%$ ), 14 dpi contralateral ( $84\pm 2\%$ ) and 14 dpi lesions ( $29\pm 2\%$ ) ( $p < 0.001$ , for all comparisons). The mean 14 dpi lesion percent MBP staining is also significantly lower than naïve, 7 dpi contralateral and 14 dpi contralateral ( $p < 0.001$ , for all comparisons) (**Figure 5.5A**).

The percent MBP staining of each group was normalized by dividing by the values of the contralateral side. Normalized percent MBP staining of 7 dpi lesions ( $0.19\pm 0.02$ ) was significantly lower than that of 14 dpi lesions ( $0.52\pm 0.05$ ) and naïve ( $1.00\pm 0.04$ ) ( $p < 0.001$  for both comparisons). Additionally, 14 dpi lesions had significantly lower normalized percent MBP staining than naïve ( $p < 0.001$ ) (**Figure 5.5B**).

The mean percent SMI312 staining of 7 dpi lesions ( $27\pm 2\%$ ) is significantly lower than the means of naïve ( $63\pm 2\%$ ), 7 dpi contralateral ( $64\pm 2\%$ ), and 14 dpi contralateral ( $63\pm 3\%$ ) ( $p < 0.001$ , for all comparisons). The mean 14 dpi lesion percent SMI312 staining ( $24\pm 4\%$ ) is also significantly lower than naïve, 7 dpi contralateral and 14 dpi contralateral percent SMI312 staining ( $p < 0.001$ , for all comparisons). The mean percent SMI312 staining in 7 dpi lesions was not significantly different than the mean of 14 dpi lesions ( $p = 0.39$ ) (**Figure 5.5C**).

The percent SMI312 staining of naïve, 7 dpi and 14 dpi lesions were normalized by dividing by the values of the contralateral side. The normalized

percent SMI312 staining of 7 dpi lesions ( $0.42 \pm 0.02$ ) was not significantly different from 14 dpi lesion ( $0.38 \pm 0.05$ ) ( $p=0.31$ ). Normalized percent SMI312 staining of the naïve group ( $1.00 \pm 0.03$ ) was significantly higher than both 7 dpi and 14 dpi lesion areas ( $p < 0.001$ , for both comparisons) (**Figure 5.5D**).

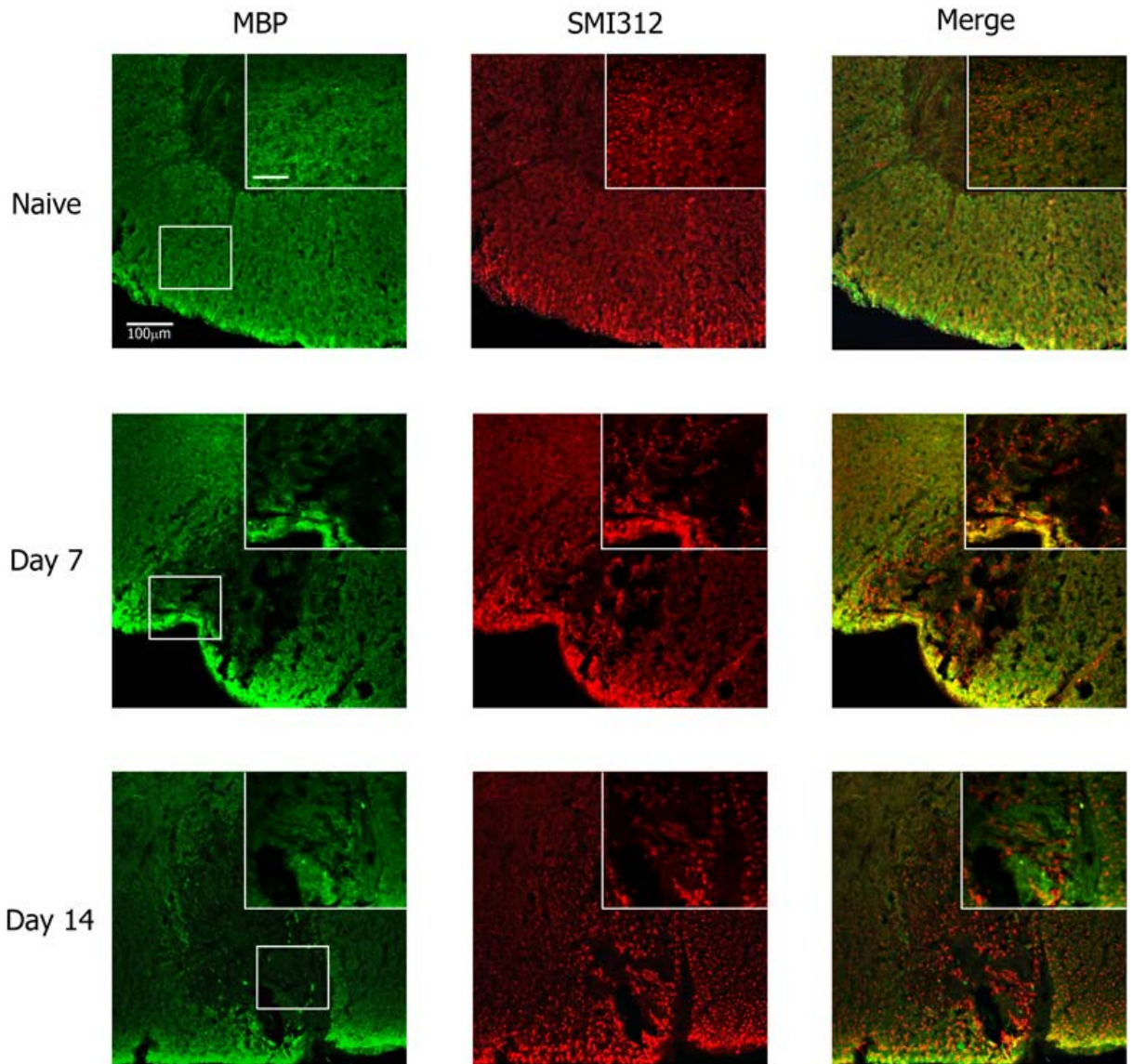


**Figure 5.4: Myelin basic protein (MBP) and SMI-312 staining for naïve, 7 dpi and 14 dpi of lysolecithin.** Staining of thoracic spinal cords of the C57BL/6 mice. MBP staining is shown in green, SMI-312 staining (pan-neurofilament stain) is shown in red. A decrease in MBP and SMI-312 staining can be seen in both the 7 dpi and 14 dpi lesion area. Scale bars (White Top Left Image): 100µm (main image), 50µm (inset). White boxes in MBP image indicate the location of the higher magnification images.

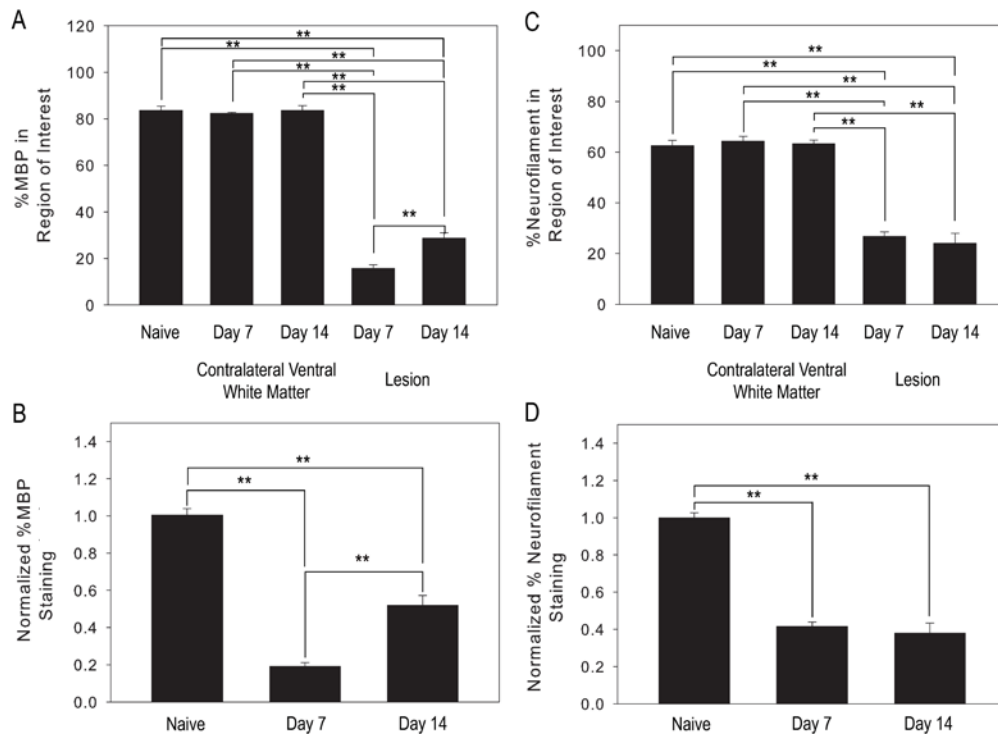


**Figure 5.5: Quantification of myelin basic protein (MBP) and SMI312 staining of naïve (n=5), contralateral regions (7 dpi n=5; 14 dpi n=7), 7 dpi lesion (n=7) and 14 dpi lesions (n=7).** **A:** The percent of MBP staining was significantly lower in 7 dpi and 14 dpi lesions than naïve and contralateral white matter controls. 14 dpi lesions had significantly higher % MBP staining compared to 7 dpi lesions. **B:** The %MBP staining was normalized by dividing by the value of the contralateral side. When normalized, the %MBP staining was still significantly higher in naïve controls compared to 7 dpi and 14 dpi lesions. Also, 14 dpi lesion normalized % MBP staining remained greater than 7 dpi lesions normalized % MBP staining. **C:** The percent of SMI312 (pan-neurofilament stain) was significantly lower at 7 dpi and 14 dpi lesions compared to naïve and contralateral white matter controls. **D:** The % SMI312 staining was normalized by dividing by the value of the contralateral side. The normalized % SMI312 staining was still significantly higher in naïve controls compared to 7 dpi and 14 dpi lesions. One-way ANOVAs with a Tukey's posthoc tests were used to test for significant differences between groups. Mean±SD. \* ≤0.05, \*\*<0.001

### 5.1.3 Correlations between Histological Staining

The percent MBP staining correlated with the percent SMI312 staining and the normalized percent SMI312 staining. The normalized percent MBP staining did not significantly correlate with the percent SMI312 staining or the normalized percent SMI312 staining (**Table 5.1**). Scatterplots with best-fit lines of histology correlations can be seen in **Figure 5.6**.

**Table 5.1: Correlations between histological measures of myelin and axons.** Spearman correlation coefficients ( $\rho$ ) of mean MBP staining to SMI312 staining in lysolecithin lesions, contralateral white matter, and naïve controls.

Parameter	% MBP	Normalized % MBP
% SMI312	$\rho=0.60^{**}$ $p<0.001$	$\rho=0.44$ $p=0.08$
Normalized % SMI312	$\rho=0.61^{**}$ $p=0.01$	$\rho=0.47$ $p=0.06$

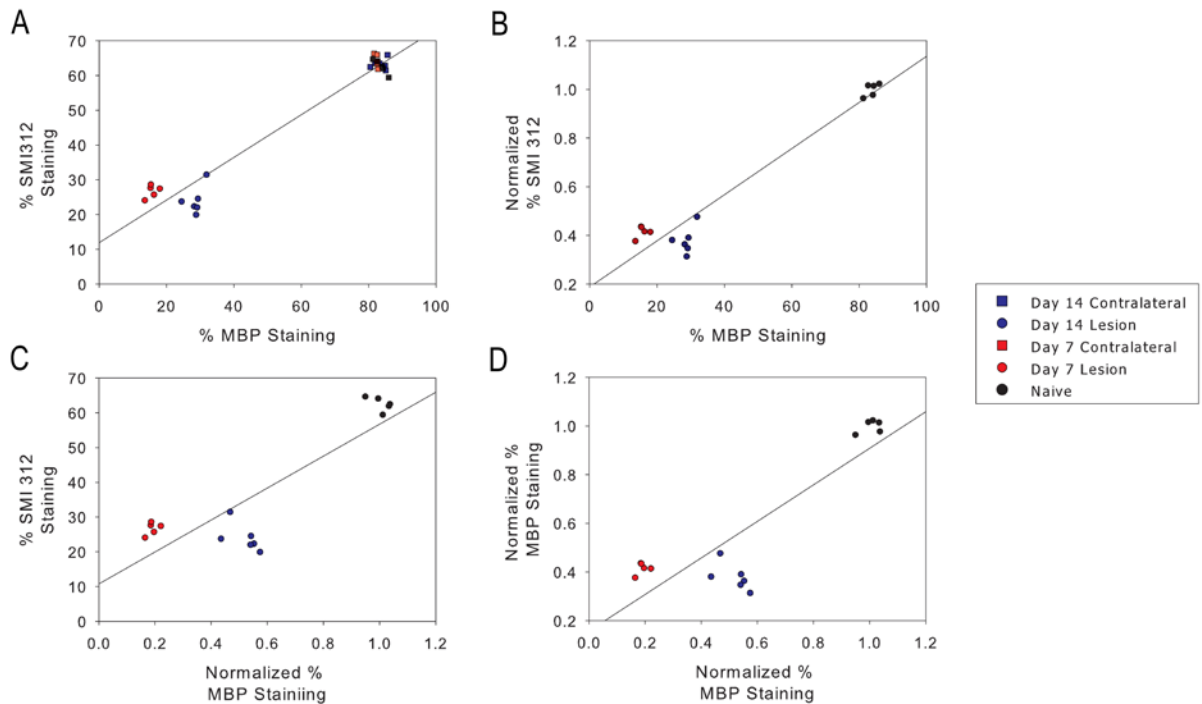


**Figure 5.6: Scatterplots and best-fit lines of MBP and SMI312 staining.**

Each point on the graphs represents a region of interest. **A:** Percent MBP staining and percent SMI312 staining. Contralateral side was used as a separate region of interest in this graph. **B:** Percent MBP staining and normalized percent SMI312 staining. **C:** Normalized percent MBP staining and normalized percent SMI312 staining. **D:** Normalized percent MBP staining and normalized percent SMI312 staining.

#### ***5.1.4 Quantitative Magnetization Transfer Parameters correlate with Histological Stains for Myelin and Neurofilament***

Significant correlations were found between the percent MBP staining and  $f$ , normalized  $f$ ,  $T_1$ , normalized  $T_1$ ,  $T_2^A$ ,  $T_2^B$  and normalized  $T_2^B$ . When percent MBP staining was normalized, these same correlations were still seen. We also found significant correlations between % SMI312 staining and  $f$ , normalized  $f$ ,  $T_1$ , normalized  $T_1$ ,  $T_2^A$ ,  $T_2^B$  and normalized  $T_2^B$ . These correlations remained when % SMI312 staining was normalized (**Table 5.2**).

Scatterplots with best-fit lines of  $f$  and normalized  $f$  compared to histological stains can be seen in **Figure 5.7**. Scatterplots with best-fit lines of  $T_1$  and normalized  $T_1$  compared to histological stains can be seen in **Figure 5.8**. Finally, scatterplots with best-fit lines of other qMT parameters that were found to strongly correlate (correlation coefficient above 0.70) with the quantification of histological staining can be accessed in **Figure 5.9**.

**Table 5.2: correlations between quantitative Magnetization Transfer parameters and histology.**

Spearman correlation coefficients ( $\rho$ ) of qMT parameters (bound pool fraction (f),  $T_1$ , and  $T_2$  of the liquid ( $T_2^A$ ) and bound pools ( $T_2^B$ ) and quantifications of histological staining. \* $p < 0.05$ , \*\* $p < 0.001$ . Yellow background indicates a significant difference. Green background indicates significant differences with  $\rho < -0.70$  or  $\rho > 0.70$ .

Parameter	% MBP	Normalized % MBP	% SMI312	Normalized % SMI312
f	$\rho = 0.66^{**}$ $p < 0.001$	$\rho = 0.66^*$ $p = 0.005$	$\rho = 0.67^*$ $p < 0.001$	$\rho = 0.73^{**}$ $p < 0.001$
Normalized f	$\rho = 0.83^{**}$ $p < 0.001$	$\rho = 0.74^{**}$ $p < 0.001$	$\rho = 0.70^*$ $p = 0.002$	$\rho = 0.72^*$ $p = 0.001$
$T_1$	$\rho = -0.60^{**}$ $p = 0.001$	$\rho = -0.51^*$ $p = 0.04$	$\rho = -0.77^{**}$ $p < 0.001$	$\rho = -0.80^{**}$ $p < 0.001$
Normalized $T_1$	$\rho = -0.68^*$ $p = 0.003$	$\rho = -0.54^*$ $p = 0.03$	$\rho = -0.64^*$ $p = 0.007$	$\rho = -0.69^*$ $p = 0.003$
$T_2^A$	$\rho = -0.45^*$ $p = 0.01$	$\rho = -0.49$ $p = 0.052$	$\rho = -0.51^*$ $p = 0.006$	$\rho = -0.77^{**}$ $p < 0.001$
Normalized $T_2^A$	$\rho = -0.34$ $p = 0.19$	$\rho = -0.55^*$ $p = 0.03$	$\rho = -0.42$ $p = 0.10$	$\rho = -0.45$ $p = 0.08$
$T_2^B$	$\rho = 0.48^*$ $p = 0.01$	$\rho = 0.59^*$ $p = 0.02$	$\rho = 0.49^*$ $p = 0.009$	$\rho = 0.53^*$ $p = 0.04$
Normalized $T_2^B$	$\rho = 0.63^*$ $p = 0.009$	$\rho = 0.57^*$ $p = 0.02$	$\rho = 0.67^*$ $p = 0.004$	$\rho = 0.72^*$ $p = 0.002$

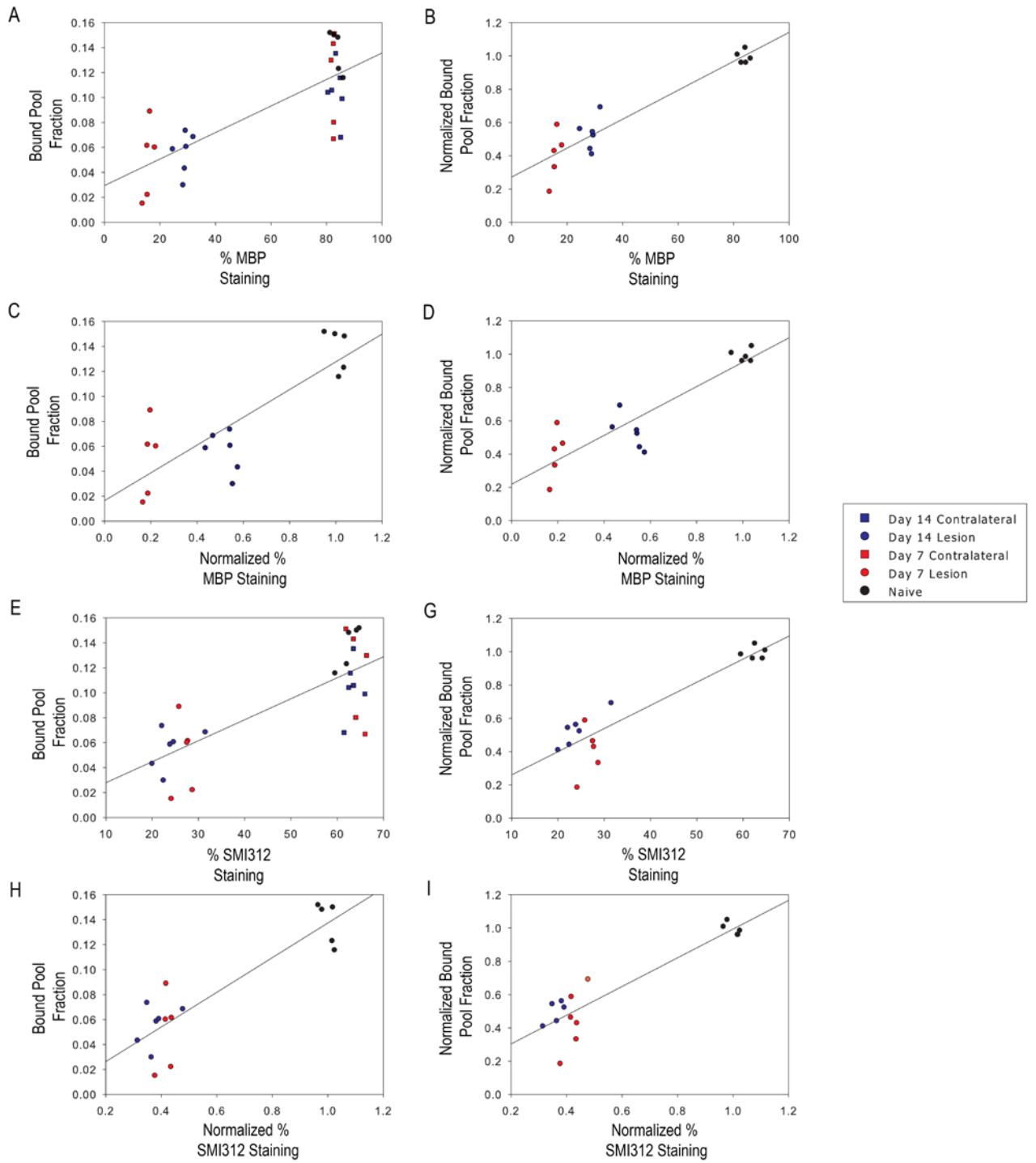


**Figure 5.7: Scatterplots and best fit lines of bound pool fraction and quantification of histological stains.** Each point on the graphs represents a region of interest. **A:** Bound pool fraction and percent MBP staining, **B:** Normalized bound pool fraction and percent MBP staining, **C:** Bound pool fraction and normalized percent MBP staining, **D:** Normalized bound pool fraction and normalized percent MBP staining, **E:** Bound pool fraction and percent SMI312 staining, **G:** Normalized bound pool fraction and percent SMI312 staining, **H:** Bound pool fraction and normalized percent SMI312 staining, **I:** Normalized bound pool fraction and normalized percent SMI312 staining.

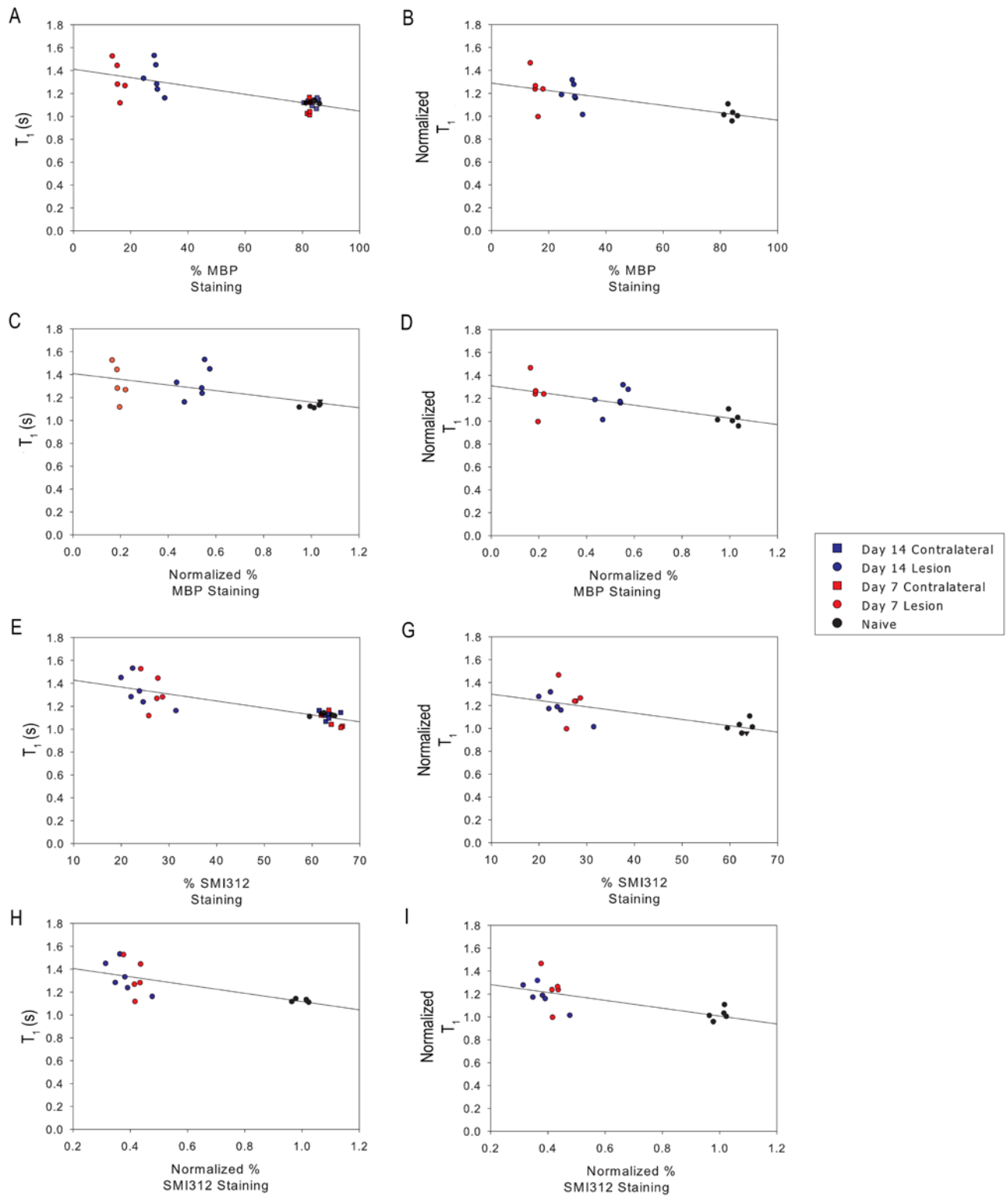


**Figure 5.8: Scatterplots and best-fit lines of  $T_1$  and quantification of histological stains.** Each point on the graphs represents a region of interest. **A:**  $T_1$  and percent MBP staining, **B:** Normalized  $T_1$  and percent MBP staining. **C:**  $T_1$  and normalized percent MBP staining. **D:** Normalized  $T_1$  and normalized percent MBP staining. **E:**  $T_1$  and percent SMI312 staining, **G:** Normalized  $T_1$  and percent SMI312 staining. **H:**  $T_1$  and normalized percent SMI312 staining. **I:** Normalized  $T_1$  and normalized percent SMI312 staining. Normalization of a parameter was done by dividing by the value of the contralateral side.



## 5.2 Discussion

### *5.2.1 T<sub>1</sub> and Quantitative Magnetization Transfer of Lysolecithin Lesions*

After the qMT sequence was validated, we used it to compare lysolecithin cords at 7 and 14 dpi with naïve controls. 7 dpi is known to correspond to peak demyelination in this model, and by 14 dpi we expect that remyelination will have begun (Keough et al., 2015). We found that T<sub>1</sub> was longer in 7 and 14 dpi lesions compared to controls, and the f was lower in 7 and 14 dpi lesions compared to controls. T<sub>1</sub> has previously been shown to inversely correlate with the number of myelinated axons in tissue (Thiessen et al., 2013). Thus the increase in T<sub>1</sub> may be due to inflammation and the loss of both axons and myelin within the lesion area.

The f has been previously shown to decrease with demyelination in other animal models and post-mortem MS tissue (Schmierer et al., 2004; Schmierer et al., 2008; Samsonov et al., 2012; Janve et al., 2013; Thiessen et al., 2013; Turati et al., 2015). Unfortunately, the f of 7 and 14 dpi lesions was not significantly different indicating this parameter was unable to differentiate between de- and remyelination in the lysolecithin model.

A previous study that looked at the ability of f to detect de- and remyelination in cuprizone mice found that f was able to distinguish remyelinated tissue from demyelinated tissue in C57BL/6 but not in SJL/J mice (Turati et al., 2015). Histological evaluation of remyelination in these two strains demonstrated that remyelination did occur but was less extensive in SJL/J mice. The paper suggested this less extensive remyelination as the reason f was unable to detect remyelination in this model (Turati et al., 2015). Although the histological data of this study demonstrated that remyelination is detectable at 14 dpi, it is possible

that this remyelination was not extensive enough for detection by  $f$ , like the SJL/J cuprizone mice.

It has been shown that fixation can cause an increase in qMT parameters (Schmierer et al., 2008). *In vivo*  $f$  values of control mouse brains have been reported to be between 0.06-0.08 (Rausch et al., 2009), where as in this study we found values of  $\sim 0.15$ . The higher  $f$  reported here is likely due to fixation. To control for changes to qMT parameters caused by variability in fixation, we divided the qMT measurements of lesion areas by the qMT measurements of contralateral white matter (i.e. normalized the measurements). This normalization would help adjust for fixation because both sections of the cord would have had the same quality of fixation.

Normalizing the data by dividing by the values of the contralateral side did not result in any major changes to the differences found. The normalized  $f$  remained lower, and the normalized  $T_1$  remained higher in 7 dpi and 14 dpi lesions compared to naïve controls.

This data indicates that qMT parameters can be used to detect demyelination in the lysolecithin model of MS.

### ***5.2.2 Histology***

As expected the % MBP and % SMI312 staining demonstrated a significant decrease in both myelin and axonal content of lysolecithin lesions (Keough et al., 2015). Also, % MBP showed that remyelination has begun to occur by 14 dpi in the lysolecithin model as expected based on the literature (Keough et al., 2015).

Like the qMT parameters, we also normalized the histology data by dividing by the amount of staining in the contralateral white matter. This normalization was done to control for variations in the effectiveness of staining between cords. Also like the qMT parameters normalization of the histological

values did not result in major changes to the differences between groups that were found.

The % MBP staining quantification confirms that demyelination has occurred at 7 dpi and remyelination has begun at 14 dpi. The % SMI312 quantification demonstrates that significant axonal loss has taken place in 7 dpi and 14 dpi in lesions.

### ***5.2.3 Correlations between Histological Stains***

Significant correlations were seen between the percent MBP staining and both the percent SMI312 staining and normalized percent SMI312 staining. This correlation is to be expected as when axons are lost then, myelin is likewise lost, and similar correlation coefficients between axon and myelin stains have been previously reported (Thiessen et al., 2013; Turati et al., 2015). These correlations were no longer significant when MBP data was normalized. Scatterplots of percent MBP staining and normalized percent MBP staining shown in Figure 5.7 demonstrate that the difference between 14 dpi and 7 dpi lesions is amplified when the MBP data is normalized. This amplification of the difference between 14 dpi and 7 dpi lesions that exist with MBP staining but not SMI312 staining, may be what causes the significant correlation to be lost.

### ***5.2.4 Correlations between quantitative Magnetization transfer and Histology***

$f$  was the qMT parameter with the strongest correlation to the amount of MBP staining and  $T_1$  had the strongest correlation to the amount of SMI312 staining.  $f$ , in terms of biology, relates to the amount of lipids present in tissue.  $T_1$ , on the other hand, relates to the spin-lattice relaxation characteristics of protons. In other words, we would expect to see a higher  $T_1$  in areas where lattice size has decreased (i.e. the loss of lipids) and areas where water mobility

has increased.  $f$ , unlike  $T_1$  is more specific to just the loss of lipids and less affected by changes in water mobility (Thiessen et al., 2013). These results are similar to those reported by Thiessen et al., 2013 where they found  $f$  had the strongest correlation to myelin and  $T_1$  to axons in cuprizone mice. The correlation coefficient for  $f$  and histological quantification of myelin seen here is within the range of those previously reported in the literature (Odrobina et al., 2005; Schmierer et al., 2007a; Thiessen et al., 2013).

This data demonstrates that qMT parameters correlate with histological measures of both myelin and axonal content of tissue in lysolecithin mice.

### **5.3 Conclusions**

This chapter shows data from histology and quantitative magnetization transfer as it relates to demyelination and remyelination in the lysolecithin model. We found that despite the high correlation between bound pool fraction and the histological measures of myelin, this parameter was unable to distinguish between demyelinated and partially remyelinated lesions.

## Chapter Six: Diffusion Tensor Imaging Parameters Correlate with Histological Stains for Myelin and Neurofilament

### 6.1 Results

#### 6.1.1 Diffusion Tensor Imaging Parameters in Lysolecithin Lesions

Naïve (n=4), 7 dpi (n=5) and 14 dpi (n=7) cords were imaged with an echo-planar sequence and diffusion tensor parameters were calculated. The lesions at 7 dpi and 14 dpi are visible on b=0 echo planar images (**Figure 6.1**). Lesions were not visible on DTI tractography.

The mean fractional anisotropy (FA) of 7 dpi lesions ( $0.41 \pm 0.18$ ) is significantly lower than naïve ( $0.87 \pm 0.006$ ) ( $p=0.001$ ), 7 dpi contralateral ( $0.72 \pm 0.18$ ) ( $p=0.005$ ) and 14 dpi contralateral regions ( $0.73 \pm 0.07$ ) ( $p=0.008$ ). There were no differences found between 14 dpi lesion FA ( $0.57 \pm 0.09$ ) and naïve ( $p=0.06$ ), 7 dpi contralateral ( $p=0.40$ ), 14 dpi contralateral ( $p=0.41$ ) and 7 dpi lesion groups ( $p=0.36$ ) (**Figure 6.2**).

The FA of naïve, 7 dpi and 14 dpi lesions were normalized by dividing by the value of the contralateral side (**Figure 6.3**). The mean normalized FA of naïve regions of interest ( $1.0 \pm 0.1$ ) and 7 dpi lesions ( $0.56 \pm 0.14$ ) are significantly different ( $p < 0.001$ ). The mean 14 dpi lesions normalized FA ( $0.78 \pm 0.18$ ) was not significantly different from naïve ( $p=0.07$ ) or 7 dpi ( $p=0.053$ ) (**Figure 6.3**).

There was no difference ( $p=0.61$ ) in AD found between groups. The 7 dpi lesion RD ( $0.60 \pm 0.22 \text{mm}^2/\text{s}$ ) is significantly higher than naïve ( $0.13 \pm 0.04 \text{mm}^2/\text{s}$ ) ( $p < 0.001$ ), 7 dpi contralateral ( $0.30 \pm 0.11 \text{mm}^2/\text{s}$ ) ( $p=0.006$ ) and 14 dpi contralateral ( $0.28 \pm 0.06 \text{mm}^2/\text{s}$ ) ( $p=0.004$ ). There was no difference found between 14 dpi lesions RD ( $0.40 \pm 0.07 \text{mm}^2/\text{s}$ ) and that of naïve ( $p=0.08$ ), 7 dpi contralateral ( $p=0.69$ ), 14 dpi contralateral ( $p=0.62$ ) and 7 dpi lesions ( $p=0.15$ ). The mean diffusivity (MD) data failed an equal variance test and therefore a Kruskal-Wallis one-way ANOVA on Ranks was used to test for significant

differences. There was no difference found between groups MD means ( $p=0.12$ ) (**Figure 6.4**).

The AD, RD, and MD of naïve and 7 dpi and 14 dpi lesions were normalized by dividing by the value of the contralateral side (**Figure 6.5**). The mean normalized AD of naïve cords ( $1.21\pm 0.28$ ) was significantly higher than the normalized AD of 7 dpi ( $0.86\pm 0.09$ ) and 14 dpi ( $0.91\pm 0.12$ ) lesions ( $p=0.008$  and  $p=0.023$ , respectively). The mean 7 dpi and 14 dpi normalized ADs were not significantly different ( $p=0.85$ ). The normalized RD and MD were not significantly different between groups ( $p=0.58$  and  $p=0.62$ , respectively) (**Figure 6.5**).

The CL of 7 dpi lesions ( $0.22\pm 0.14$ ) was significantly lower than naïve ( $0.62\pm 0.12$ ) ( $p=0.001$ ), 7 dpi contralateral ( $0.52\pm 0.20$ ) ( $p=0.005$ ) and 14 dpi contralateral regions ( $0.48\pm 0.03$ ) ( $p=0.03$ ). There were no differences found between 14 dpi lesion CL ( $0.38\pm 0.11$ ) and naïve ( $p=0.08$ ), 7 dpi contralateral ( $p=0.37$ ), 14 dpi contralateral ( $p=0.74$ ) and 7 dpi lesion groups ( $p=0.32$ ) (**Figure 6.6A**). There was no difference between groups CP ( $p=0.35$ ) (**Figure 6.6B**). The VR of 7 dpi lesions ( $0.028\pm 0.006$ ) was significantly higher than naïve ( $0.009\pm 0.005$ ) ( $p=0.001$ ), 7 dpi contralateral ( $0.015\pm 0.01$ ) ( $p=0.01$ ) and 14 dpi contralateral regions ( $0.016\pm 0.004$ ) ( $p=0.03$ ). The VR of 14 dpi lesion ( $0.024\pm 0.004$ ) was significantly ( $p=0.02$ ) higher than naïve cords (**Figure 6.6E**). There was no difference between the VR of 14 dpi lesions and 7 dpi contralateral ( $p=0.18$ ), 14 dpi contralateral ( $p=0.29$ ), and 7 dpi lesions ( $p=82$ ) (**Figure 6.6E**).

The CS and RA data failed an equal variance test and therefore a Kruskal-Wallis one-way ANOVA on Ranks with a Dunn's posthoc test was used to test for significant differences between groups. The one-way ANOVA on ranks indicated that there is a significant difference between groups RA ( $p=0.02$ ) but a Dunn's post hoc test did not find any significant differences between groups (**Figure 6.6D**). The CS of 7 dpi lesions ( $0.62\pm 0.14$ ) was significantly higher than naïve ( $0.22\pm 0.08$ ) ( $p<0.001$ ), 7 dpi contralateral ( $0.35\pm 0.19$ ) ( $p=0.006$ ) and 14 dpi

contralateral regions ( $0.34 \pm 0.09$ ) ( $p=0.006$ ). The CS of 14 dpi lesions ( $0.52 \pm 0.08$ ) was significantly ( $p=0.02$ ) higher than naïve cords. There was no difference between the CS of 14 dpi lesions and 7 dpi contralateral ( $p=0.18$ ), 14 dpi contralateral ( $p=0.17$ ), and 7 dpi lesions ( $p=0.59$ ) (**Figure 6.6C**).

The CL, CP, CS, RA and VR of the 7 dpi and 14 dpi lesions were normalized by dividing by the value of the contralateral side (**Figure 6.7**). The mean normalized CL of naïve controls ( $1.02 \pm 0.17$ ) was significantly higher than both 7 dpi ( $0.40 \pm 0.69$ ) ( $p < 0.001$ ) and 14 dpi lesions ( $0.69 \pm 0.24$ ) ( $p=0.04$ ). The normalized CL of 7 and 14 dpi lesions were also significantly different ( $p=0.03$ ) (**Figure 6.7A**). The mean normalized CS of naïve ( $0.90 \pm 0.40$ ) controls was significantly lower than 7 dpi lesions ( $2.18 \pm 0.94$ ) ( $p=0.40$ ) but not significantly different compared to 14 dpi lesions ( $1.65 \pm 0.60$ ) ( $p=0.76$ ). The normalized CS of 7 dpi lesions was not significantly different from the normalized CL of 14 dpi lesions ( $p=0.29$ ) (**Figure 6.7C**). The normalized RA of naïve controls ( $1.11 \pm 0.07$ ) was significantly higher than that of 7 dpi ( $0.52 \pm 0.12$ ) ( $p < 0.001$ ) and 14 dpi ( $0.74 \pm 0.22$ ) ( $p=0.006$ ) lesions. A significant difference was not seen between the normalized RA of 7 dpi and 14 dpi lesions ( $p=0.06$ ) (**Figure 6.7D**). The normalized CP was not significantly different between groups ( $p=0.68$ ) (**Figure 6.7B**). The normalized VR failed an equal variance test and thus a Shapiro-Wilk ANOVA on Ranks was used to test for significant differences. The mean normalized VR was not significantly different between groups ( $p=0.09$ ) (**Figure 6.7E**).

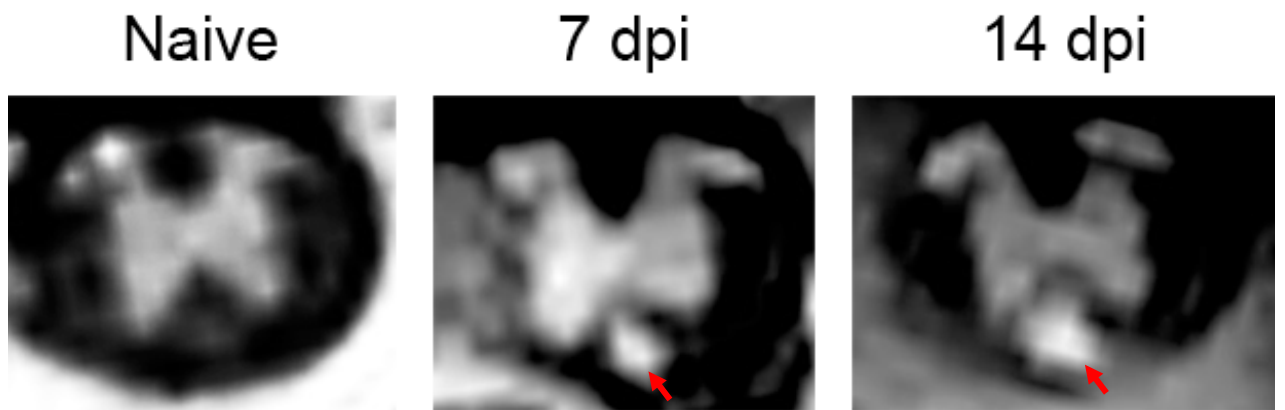


**Figure 6.1: B=0 Echo planar images of Naïve, 7 dpi, and 14 dpi lesions.**  
Lesions are indicated by red arrows.

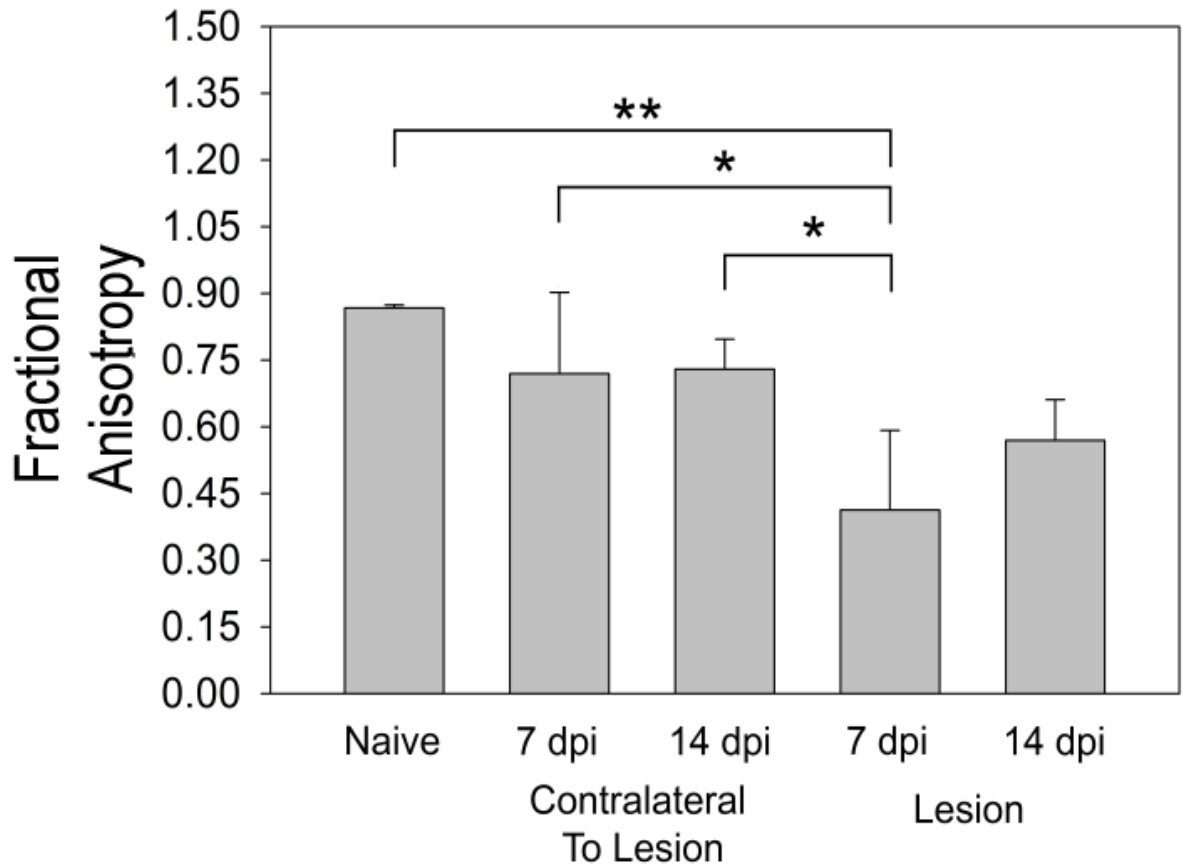


**Figure 6.2: Fractional Anisotropy (FA) of naïve (n=4), 7 dpi (n= 5) and 14 dpi (n=7) contralateral regions, 7 dpi (n=5) lesions and 14 dpi (n=7) lesions.** The FA of 7 dpi lesions were significantly lower than naïve and contralateral regions. A one-way ANOVA with Tukey's post hoc test was used to test for significant differences between groups. Mean±SD. \* <0.05, \*\*≤0.001

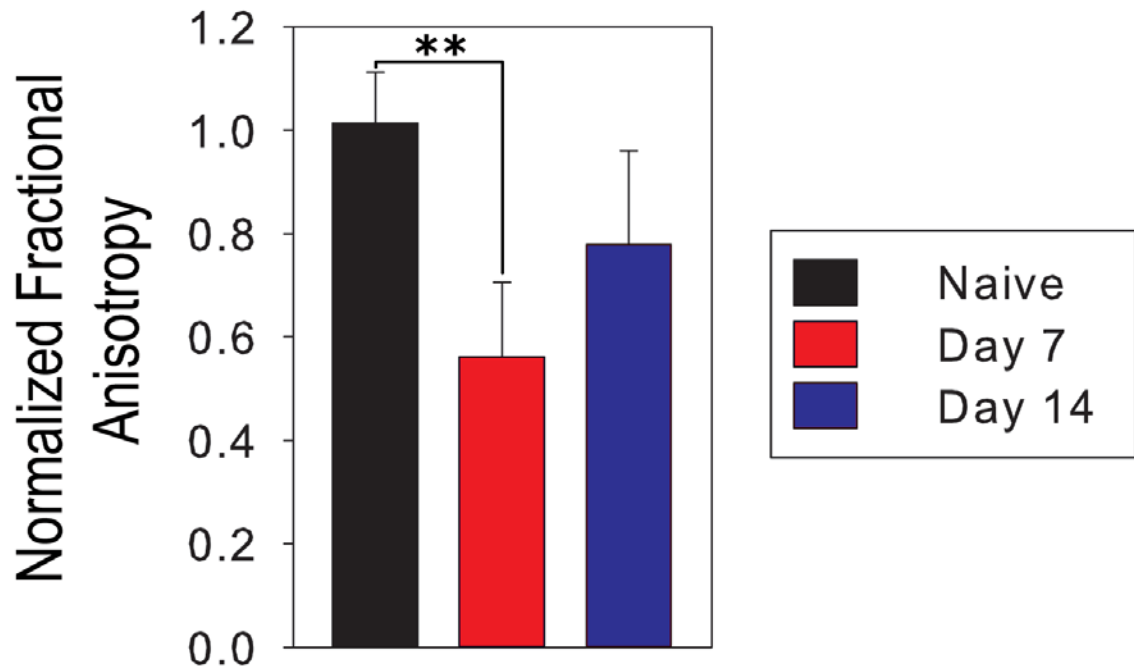


**Figure 6.3: Normalized fractional anisotropy (FA) of naïve (n=4), 7 (n=5) and 14 (n=7) dpi lesions.** The lesion data was normalized by dividing by the value of the contralateral side. The normalized FA of naïve cords was significantly higher than 7 dpi lesions. One-way ANOVAs with Tukey's post hoc test were used to test for significant differences. Mean±SD. \*\*≤0.001

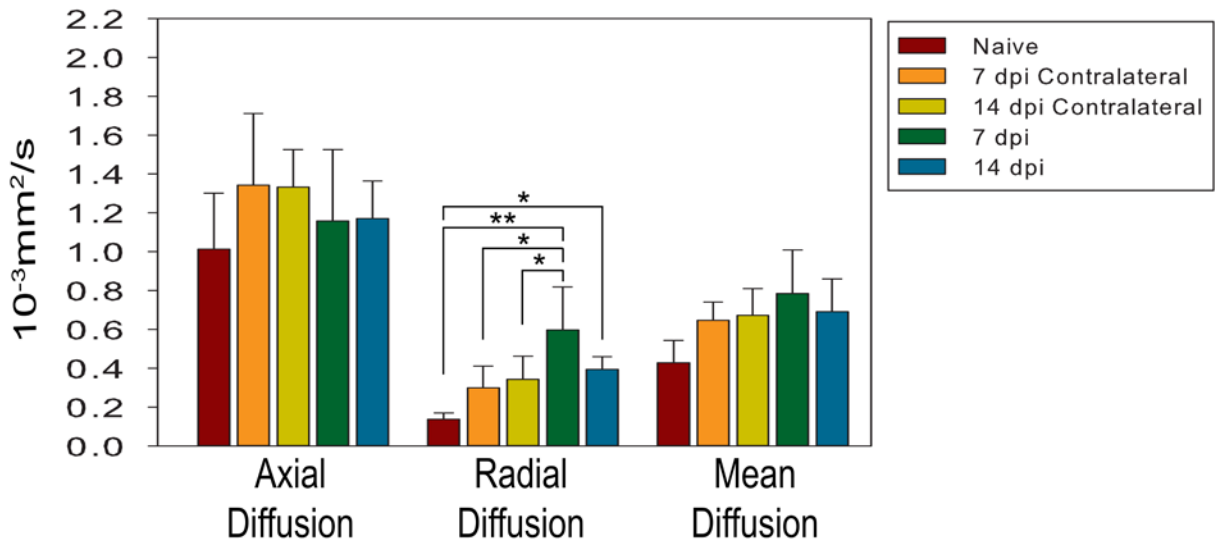


**Figure 6.4: Radial diffusion, axial diffusion, and mean diffusion of naïve (n=3), 7 dpi (n=7) and 14 dpi (n=5) contralateral regions, 7 dpi lesions (n=7) and 14 dpi lesions (n=5).** Axial did not significantly differ between groups. The radial diffusivity was significantly higher in 7 dpi lesions compared to naïve cords and contralateral regions. 7 dpi also have a higher mean diffusivity compared to naïve cords. A one-way ANOVA with a Tukey's post hoc test was used to test for differences between groups. Mean±SD. \* ≤0.05, \*\*<0.001

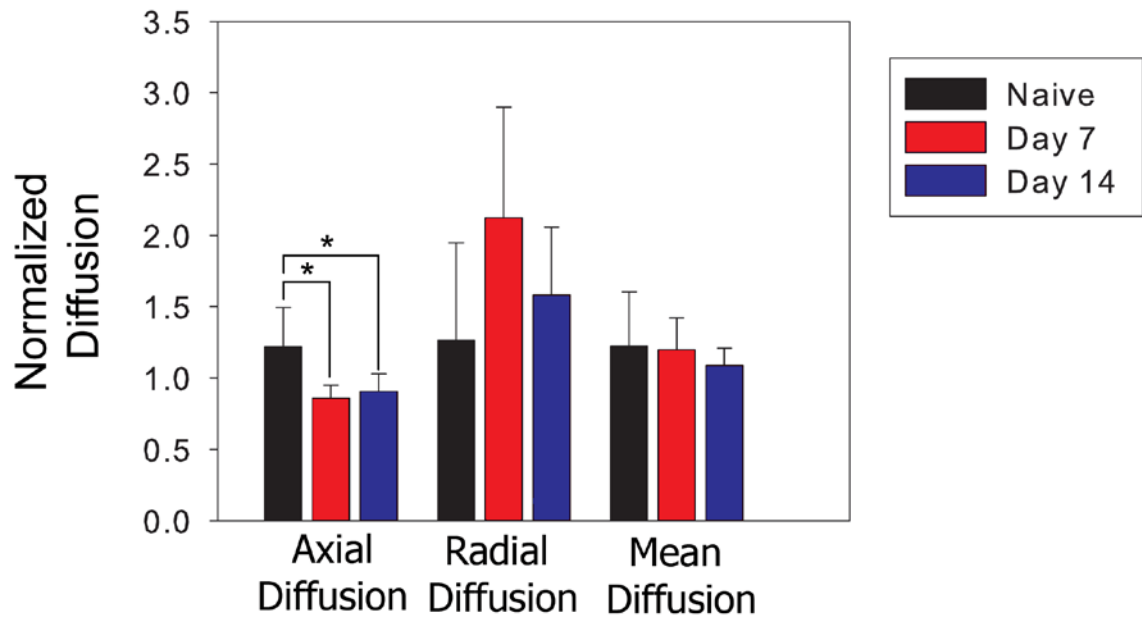


**Figure 6.5. Normalized axial diffusion, radial diffusion and mean diffusion of naïve (n=4) and 7 (n=5) and 14 (n=7) dpi lesions.** The data was normalized by dividing by the value of the contralateral side. The axial diffusion was significantly higher at naïve compared to 7 and 14 dpi lesions. One-way ANOVAs with Tukey's post hoc tests were used to test for significant differences between groups. Mean±SD. \* <0.05

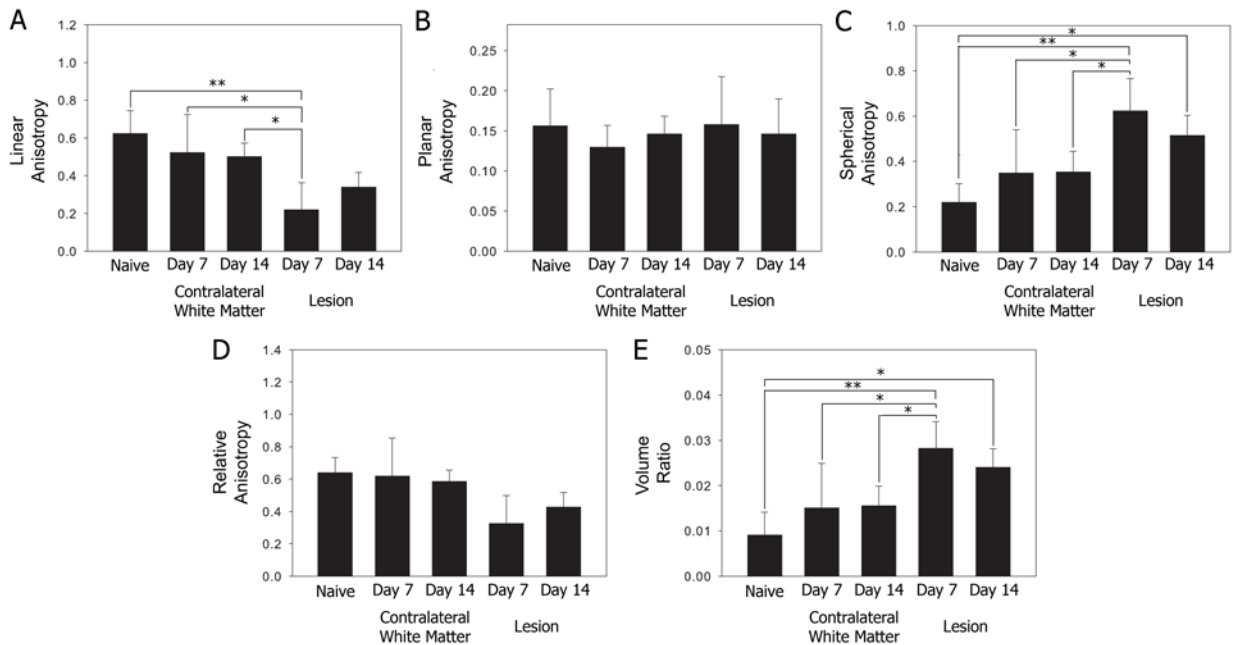


**Figure 6.6: Linear Anisotropy (CL), Planar Anisotropy (CP), Spherical Anisotropy (CS), Relative Anisotropy and volume ratio (VR) of naïve (n=4), contralateral regions (7 dpi n=5; 14 dpi n=7), 7 dpi (n=5) and 14 dpi (n=7) lesions. A:** The CL of 7 dpi lesions is significantly lower than naïve and contralateral regions. **C, E:** The CS and VR were significantly higher at 7 dpi lesions compared to naïve and contralateral controls. 14 dpi lesions also have significantly higher CS and VR than naïve and contralateral regions of interest. **B, D:** The CP and RA were not found to be significantly different between groups. A one-way ANOVA with a Tukey posthoc test was used to test for significant differences between groups for CL, CP, and VR. An ANOVA on ranks was used to test for significant differences between groups for CP and RA. Mean±SD. \* ≤0.05, \*\*<0.001

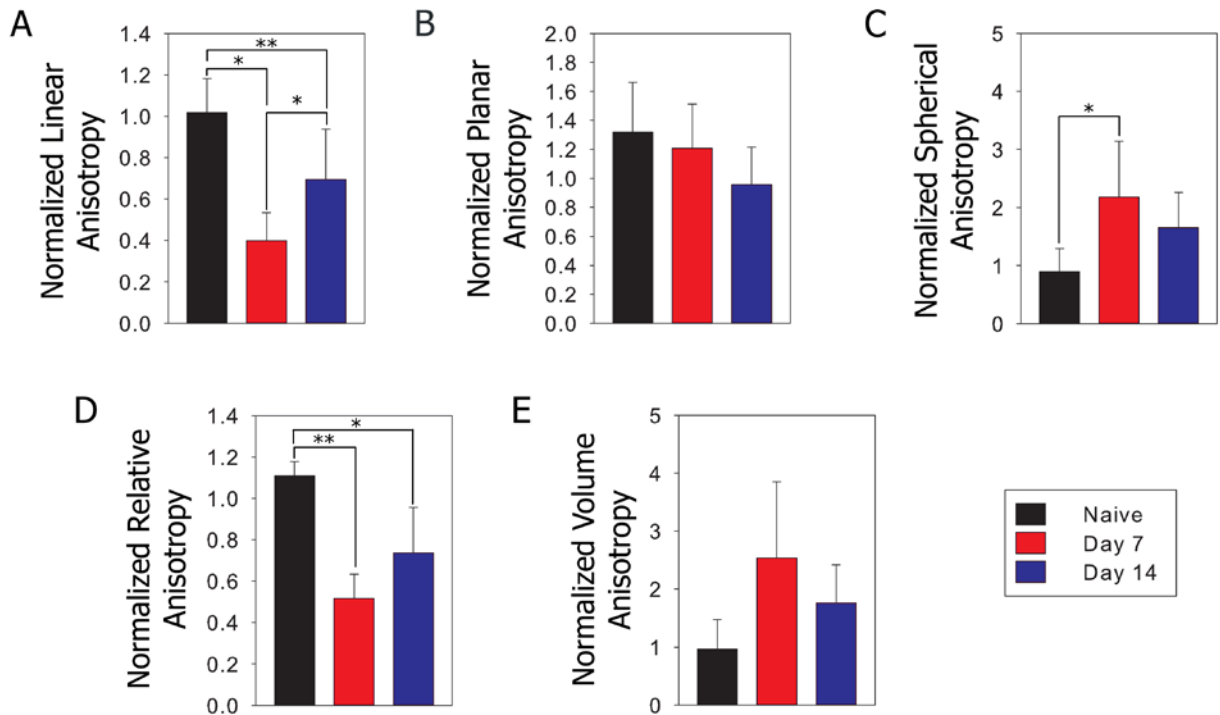


**Figure 6.7: Normalized Linear Anisotropy (CL), Planar Anisotropy (CP), Spherical Anisotropy (CS), Relative Anisotropy (RA) and the volume ratio (VR) of naive (n=4) and 7 dpi (n=5) and 14 dpi (n=7) lesions.**

The data was normalized by dividing by the value of the contralateral side. **A:** The CL was significantly lower at 7 dpi compared to 14 dpi and naive controls. The CL of 14 dpi cords was also significantly lower than naive controls. **B:** No significant differences were found between groups CP. **C:** The CS was significantly higher at 7 dpi compared to naive controls. **D:** The RA of naive controls was significantly higher than 7 dpi and 14 dpi lesions. **E:** The VR was not significantly different between groups. One-way ANOVAs with Tukey's post hoc tests were used to test for significant differences between groups CL, CP, CS, and RA. A Kruskal-Wallis ANOVA on Ranks was used to test for significant differences between groups mean VRs. Mean±SD. \* ≤0.05, \*\*<0.001

### ***6.1.2 Diffusion Tensor Imaging Parameters correlate with histological stains for MBP and neurofilament***

Significant correlations were found between percent MBP staining and FA, normalized FA, normalized AD, RD, CL, normalized CL, CS, normalized CS, RA, normalized RA, and VR. These correlations remained when percent MBP was normalized. We also saw a correlation between normalized percent MBP and normalized VR. There were significant correlations between percent SMI312 staining and FA, RD, CL, CS, RA, and VR. There was also a significant correlation between the normalized percent SMI312 staining and FA and RD but no other DTI parameter (**Table 6.1**).

Scatterplots and best-fit lines of strong significant correlations ( $\rho > 0.70$  or  $\rho < -0.70$ ) are shown (**Fig. 6.8**).

**Table 6.1: Correlations between DTI parameters and histological stains.**

Spearman correlation coefficients ( $\rho$ ) of DTI parameters and quantifications of histological staining. \* $p < 0.05$ , \*\* $p < 0.001$ . Yellow background indicates a significant difference. Green background indicates significant differences with  $\rho < -0.70$  or  $\rho > 0.70$ .

Parameter	% MBP	Normalized % MBP	% SMI312	Normalized % SMI312
FA	$\rho = 0.58^*$ $p = 0.002$	$\rho = 0.70^*$ $p = 0.003$	$\rho = 0.59^*$ $p = 0.002$	$\rho = 0.53^*$ $p = 0.04$
Normalized FA	$\rho = 0.69^*$ $p = 0.004$	$\rho = 0.73^*$ $p = 0.002$	$\rho = 0.33$ $p = 0.22$	$\rho = 0.33$ $p = 0.23$
AD	$\rho = 0.27$ $p = 0.19$	$\rho = 0.36$ $p = 0.18$	$\rho = 0.06$ $p = 0.75$	$\rho = -0.03$ $p = 0.90$
Normalized AD	$\rho = 0.69^*$ $p = 0.006$	$\rho = 0.66^*$ $p = 0.007$	$\rho = 0.43$ $p = 0.10$	$\rho = 0.45$ $p = 0.08$
RD	$\rho = -0.62^{**}$ $p < 0.001$	$\rho = -0.63^*$ $p = 0.01$	$\rho = -0.57^*$ $p = 0.003$	$\rho = -0.63^*$ $p = 0.01$
Normalized RD	$\rho = 0.10$ $p = 0.72$	$\rho = -0.005$ $p = 0.97$	$\rho = -0.15$ $p = 0.58$	$\rho = 0.03$ $p = 0.91$
MD	$\rho = -0.22$ $p = 0.27$	$\rho = -0.28$ $p = 0.31$	$\rho = -0.25$ $p = 0.22$	$\rho = -0.40$ $p = 0.14$
Normalized MD	$\rho = 0.13$ $p = 0.64$	$\rho = 0.08$ $p = 0.78$	$\rho = 0.06$ $p = 0.82$	$\rho = 0.16$ $p = 0.57$
CL	$\rho = 0.46^*$ $p = 0.02$	$\rho = 0.61^*$ $p = 0.02$	$\rho = 0.52^*$ $p = 0.007$	$\rho = 0.44$ $p = 0.10$
Normalized CL	$\rho = 0.69^*$ $p = 0.004$	$\rho = 0.78^{**}$ $p < 0.001$	$\rho = 0.31$ $p = 0.25$	$\rho = 0.26$ $p = 0.35$
CP	$\rho = 0.20$ $p = 0.34$	$\rho = 0.33$ $p = 0.22$	$\rho = -0.04$ $p = 0.83$	$\rho = 0.13$ $p = 0.65$
Normalized CP	$\rho = 0.15$ $p = 0.58$	$\rho = 0.26$ $p = 0.35$	$\rho = 0.39$ $p = 0.15$	$\rho = 0.35$ $p = 0.19$
CS	$\rho = -0.60^{**}$ $p = 0.001$	$\rho = -0.73^{**}$ $p = 0.002$	$\rho = -0.59^*$ $p = 0.001$	$\rho = -0.38$ $p = 0.15$
Normalized CS	$\rho = -0.59^*$ $p = 0.02$	$\rho = -0.73^{**}$ $p = 0.002$	$\rho = -0.32$ $p = 0.24$	$\rho = -0.28$ $p = 0.30$
RA	$\rho = 0.46^*$ $p = 0.02$	$\rho = 0.59^*$ $p = 0.04$	$\rho = 0.47^*$ $p = 0.02$	$\rho = 0.26$ $p = 0.35$
Normalized RA	$\rho = -0.73^*$ $p = 0.001$	$\rho = 0.81^{**}$ $p < 0.001$	$\rho = 0.32$ $p = 0.24$	$\rho = 0.26$ $p = 0.34$
VR	$\rho = -0.59^*$ $p = 0.001$	$\rho = -0.71^*$ $p = 0.002$	$\rho = -0.61^{**}$ $p = 0.001$	$\rho = -0.42$ $p = 0.12$
Normalized VR	$\rho = -0.49$ $p = 0.06$	$\rho = -0.64^*$ $p = 0.01$	$\rho = -0.24$ $p = 0.37$	$\rho = -0.20$ $p = 0.47$

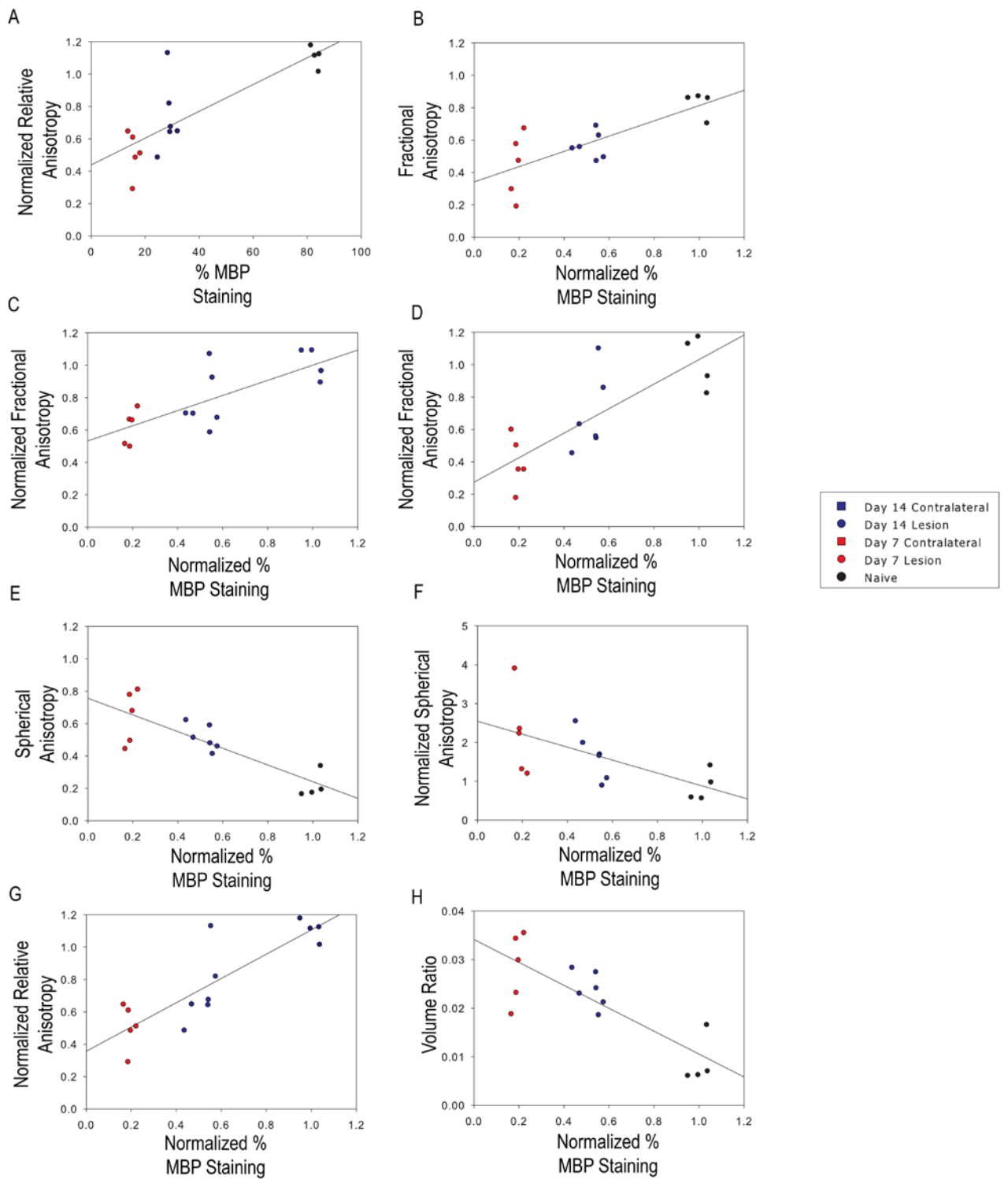


**Figure 6.8: Scatterplots and best-fit lines of DTI parameters and quantification of histological stains.** Only strong significant ( $\rho > 0.70$ ) correlations are shown. Each point on the graphs represents a cord. **A:** Normalized RA and percent MBP staining, **B:** FA and normalized percent MBP staining, **C:** Normalized FA and normalized percent MBP staining, **D:** Normalized CL and normalized percent MBP staining, **E:** CS and normalized percent MBP staining, **F:** Normalized CS and normalized percent MBP staining, **G:** Normalized RA and normalized percent MBP staining, **H:** VR and normalized percent MBP staining.

## 6.2 Discussion

### *6.2.1 Diffusion Tensor Imaging parameters of Lysolecithin Lesions*

We used diffusion tensor imaging to compare lysolecithin cords at 7 and 14 dpi. We found that the fractional anisotropy (FA) was significantly lower and the radial diffusivity (RD) was significantly higher at 7 dpi compared to controls. The 14 dpi RD is only significantly different from naïve controls. Interestingly we found that 14 dpi lesions FA was not significantly different from controls or 7 dpi lesions. This partial recovery in this parameter is likely due to remyelination.

The DTI parameters, like the qMTI parameters, were normalized by dividing by the contralateral side. Normalizing the FA did not result in major changes to the differences found between groups. However, normalizing the groups axial diffusivity (AD) and RD did cause changes to the significant differences observed. In the normalized set of data, the AD was significantly lower at both 7 dpi and 14 dpi lesions. Additionally, the normalized RD was not significantly different between groups.

A previous study of lysolecithin injection in rat spinal cord found a lower FA and AD and a higher RD in lysolecithin lesions compared to controls (DeBoy et al., 2007). This study also found that the injection site was visible on DTI tractography, which was not the case in our study. This difference may be due to the laminectomy performed during the injection procedure in the rat study (DeBoy et al., 2007). The lysolecithin model used during this study does not involve a laminectomy which would explain the differences in tractography observed.

Additionally, even though the DeBoy paper did look at lysolecithin lesions 14 and 21 dpi the data was grouped together with 7 dpi lesion data (DeBoy et al., 2007). To the best of our knowledge, no other published studies have looked at diffusion tensor imaging of the lysolecithin model. Also unpublished data from

our lab indicates that FA recovers during remyelination in the lysolecithin model (Nathoo et al., Unpublished).

Publications looking at DTI in the other animal models have shown that both FA and AD decreases and RD increase with demyelination (Song et al., 2005; Xie et al., 2010; Janve et al., 2013; Thiessen et al., 2013). Additionally, another cuprizone study found that RD recovered during remyelination. In this study, RD increased by 25% compared to control values during demyelination and then recovered to be only 10% higher than controls during remyelination (Jelescu et al., 2016).

FA can be separated into linear, planar and spherical measures depending on the shape of the diffusion ellipsoid. The linear anisotropy (CL) was lower at 7 dpi, and the spherical anisotropy (CS) was higher at 7 dpi compared to controls. The CL at 14 dpi was not significantly different from 7 dpi or controls and the SA at 14 dpi was only significantly higher than naive controls. This data indicates that the changes seen in FA are likely due to a decrease in the linear case and an increase in the spherical case with no significant change observed in the planar case.

Interestingly, when normalized the CL was significantly different between all groups (naïve, 7 dpi lesions and 14 dpi lesions). This significant difference at 14 dpi to both controls and 7 dpi was not seen in any other DTI or qMT parameter. This partial recovery in CL is likely due to remyelination, and axonal regeneration would not have had enough time to occur by 14 dpi. It also demonstrates the value of looking at the factors that compose FA rather than just FA itself as most DTI studies do.

Additionally, the volume ratio (VR), which is the ratio of the diameter of the diffusion ellipsoid to the diameter of a sphere with a radius of MD, was significantly higher in 7 dpi lesions compared to all controls. The VR was also significantly higher in 14 dpi lesions compared to naïve controls. Finally, the RA was significantly lower at 7 dpi and 14 dpi lesions compared to naïve controls

when normalized. This data is consistent with data that has demonstrated that the VR has also been shown to be higher and the RA has been demonstrated to be lower in shiverer mutant mice which lack myelin (Nair et al., 2005).

This data indicates that diffusion tensor imaging parameters, including FA, RD, CL, CS and VR, can be used to detect demyelination and remyelination in the lysolecithin model of MS.

### ***6.2.2 Diffusion Tensor Imaging and Histology Correlations***

The DTI parameters with the strongest correlations to myelin staining were normalized RA, the CS (both normalized and not normalized), the normalized CL, and the FA (both normalized and not).

Previous studies have shown correlations between myelin and FA (Schmierer et al., 2007b; Janve et al., 2013; Thiessen et al., 2013). One study also saw a correlation between myelin and AD (Thiessen et al., 2013) and one saw a correlation between myelin and MD (Schmierer et al., 2007b).

The studies that have previously assessed the correlation between DTI and myelin did not report correlations for CL, CP, CS, RA and VR parameters. To the best of my knowledge, there are no previously reported correlation coefficients for these parameters. As mentioned above CL, CP and CS are separations of FA; it is possible that looking at these parameters individually can provide greater insight into tissue pathology than looking just at FA, AD, RD, and MD, as is usually done.

There were also mild correlations between the percent SMI312 staining and FA and RD. Surprisingly, these correlations are lower than previously reported and the correlation between percent SMI312 staining and AD was not significant as has previously been reported (Schmierer et al., 2007b; Janve et al., 2013; Thiessen et al., 2013). Other studies have also seen a correlation between AD and axonal content (Thiessen et al., 2013) and between MD and axonal

content (Schmierer et al., 2007b). The lower correlation coefficients seen here are also likely in part due to the increased noise is perceived in MRI parameters when imaging at the higher resolutions required for mouse spinal cord work. As well as the partial volume effects that can occur when looking at small lesions with relatively large voxels.

This data demonstrates that diffusion parameters correlate with histological measures of both myelin content of lysolecithin lesions.

### **6.3 Conclusions**

This chapter shows data from diffusion tensor imaging (DTI) as it relates to demyelination and remyelination in the lysolecithin model. We found that DTI parameters did partial recover with remyelination. This data indicates that these parameters could be used as outcome measures in pre-clinical trials of therapeutics in this model.

## Chapter Seven: Correlations between MR Imaging Parameters

### 7.1 Results

#### *7.1.1 Correlations between Quantitative Magnetization Transfer and Diffusion Tensor Imaging parameters*

We looked for correlations between MRI parameters. We found a strong ( $\rho < -0.70$  or  $\rho > 0.70$ ) significant correlations between f and FA. Normalized f had strong significant correlations with both FA and normalized FA. Finally, normalized  $T_2^B$  had a strong correlation with FA (**Table 7.1**).

### 7.2 Discussion

Assessing how well MRI parameters correlate with each other helps determine which MRI parameters may be affected by the same underlying tissue properties.

We found a strong correlation between FA and f. Previously reported correlations between f and diffusion anisotropy had been weak or mild (Ou et al., 2009b; Stikov et al., 2011; Janve et al., 2013; Thiessen et al., 2013; Li et al., 2014). However, a study by Stikov, which looked at the correlation between f and diffusion anisotropy in different regions of the brain, found that there was a higher correlation between FA and f could in areas with high directional coherence (Stikov et al., 2011).

#### **Table 7.1: Correlations between DTI parameters and qMT parameters.**

Spearman correlation coefficients ( $\rho$ ) of qMT and DTI parameters in lysolecithin lesions and controls. Top row =  $\rho$ ; Bottom row = p-value; \*p<0.05. Yellow background indicates significant correlations with  $-0.70 < \rho < 0.70$ . Green background indicates significant correlations with  $\rho < -0.70$  or  $\rho > 0.70$ .

(Following Page)

	<b>f</b>	<b>Normalized f</b>	<b>T<sub>1</sub></b>	<b>Normalized T<sub>1</sub></b>	<b>T<sub>2</sub><sup>A</sup></b>	<b>Normalized T<sub>2</sub><sup>A</sup></b>	<b>T<sub>2</sub><sup>B</sup></b>	<b>Normalized T<sub>2</sub><sup>B</sup></b>
<b>FA</b>	<b>0.81*</b> <b>&lt;0.001</b>	0.74* <b>0.001</b>	<b>-0.38*</b> <b>0.05</b>	-0.48 0.06	<b>-0.58*</b> <b>&lt;0.001</b>	-0.09 0.75	<b>0.57*</b> <b>&lt;0.001</b>	<b>0.72*</b> <b>0.002</b>
<b>Normalized FA</b>	<b>0.68*</b> <b>0.005</b>	<b>0.70*</b> <b>0.003</b>	-0.36 0.19	-0.41 0.13	<b>-0.57*</b> <b>0.03</b>	-0.10 0.71	<b>0.62*</b> <b>0.01</b>	<b>0.59*</b> <b>0.02</b>
<b>AD</b>	0.29 0.15	0.15 0.58	-0.06 0.76	-0.06 0.81	-0.22 0.29	0.02 0.94	0.36 0.07	0.25 0.35
<b>Normalized AD</b>	<b>0.56*</b> <b>0.03</b>	<b>0.54*</b> <b>0.04</b>	-0.36 0.18	-0.39 0.15	<b>-0.58*</b> <b>0.02</b>	-0.44 0.09	<b>0.57*</b> <b>0.02</b>	0.36 0.17
<b>RD</b>	<b>-0.81*</b> <b>&lt;0.001</b>	<b>-0.84*</b> <b>&lt;0.001</b>	<b>0.38*</b> <b>0.05</b>	<b>0.63*</b> <b>0.01</b>	<b>0.55*</b> <b>0.004</b>	0.17 0.54	<b>-0.52*</b> <b>0.02</b>	<b>-0.66*</b> <b>0.007</b>
<b>Normalized RD</b>	0.06 0.82	0.05 0.85	0.05 0.84	-0.15 0.58	0.13 0.64	0.12 0.64	0.16 0.55	0.06 0.81
<b>MD</b>	<b>-0.36</b> <b>0.07</b>	<b>-0.55*</b> <b>0.03</b>	0.18 0.38	0.43 0.11	0.15 0.45	0.07 0.78	-0.12 0.54	-0.36 0.17
<b>Normalized MD</b>	0.02 0.94	0.02 0.94	0.05 0.85	-0.09 0.75	-0.04 0.89	-0.20 0.45	0.14 0.61	-0.01 0.96
<b>CL</b>	0.38 0.06	0.46 0.08	<b>-0.42*</b> <b>0.03</b>	-0.27 0.33	-0.19 0.34	0.24 0.39	<b>0.38*</b> <b>0.05</b>	0.24 0.36
<b>Normalized CL</b>	0.35 0.19	0.44 0.10	-0.20 0.47	-0.16 0.55	-0.30 0.28	-0.19 0.48	0.32 0.23	0.25 0.35
<b>CP</b>	0.17 0.41	0.18 0.51	-0.19 0.36	-0.35 0.19	0.02 0.91	-0.25 0.34	0.08 0.68	0.05 0.85
<b>Normalized CP</b>	0.33 0.22	0.20 0.47	-0.43 0.11	-0.36 0.18	-0.37 0.17	-0.46 0.08	0.35 0.19	0.29 0.27
<b>CS</b>	<b>-0.44*</b> <b>0.02</b>	-0.43 0.11	<b>0.44*</b> <b>0.02</b>	0.21 0.44	0.27 0.19	0.31 0.24	<b>-0.44*</b> <b>0.02</b>	-0.20 0.45
<b>Normalized CS</b>	<b>-0.57*</b> <b>0.03</b>	<b>-0.53*</b> <b>0.04</b>	0.43 0.11	0.36 0.18	<b>0.57*</b> <b>0.03</b>	0.18 0.48	<b>-0.62*</b> <b>0.01</b>	<b>-0.65*</b> <b>0.008</b>
<b>RA</b>	0.30 0.13	0.23 0.40	-0.34 0.08	-0.05 0.85	-0.15 0.48	-0.25 0.35	0.35 0.07	0.04 0.88
<b>Normalized RA</b>	0.34 0.21	0.42 0.11	-0.24 0.38	-0.18 0.51	-0.23 0.40	-0.16 0.54	0.30 0.25	0.19 0.48
<b>VR</b>	<b>-0.45*</b> <b>0.02</b>	-0.45 0.09	<b>0.47*</b> <b>0.02</b>	0.23 0.40	0.27 0.18	0.30 0.26	<b>-0.44*</b> <b>0.02</b>	-0.23 0.39
<b>Normalized VR</b>	<b>-0.53*</b> <b>0.04</b>	-0.48 0.07	0.42 0.12	0.32 0.24	<b>0.51*</b> <b>0.05</b>	0.10 0.71	<b>-0.57*</b> <b>0.03</b>	<b>-0.62*</b> <b>0.01</b>

In this paper, they suggest that this difference is caused by a greater overlap in the sensitivity of  $f$  and diffusion anisotropy to underlying tissue properties in areas of high directional coherence (Stikov et al., 2011). Therefore, it is not surprising that we found a higher correlation between qMT and diffusion anisotropy parameters than have previously been reported in the literature. Especially since this work was done in the spinal cord (an area of high fiber coherence) and the majority of the work published has been done in the brain (Ou et al., 2009b; Janve et al., 2013; Thiessen et al., 2013; Li et al., 2014).

This data demonstrates that qMT and diffusion parameters, particularly FA and  $f$ , overlap in their sensitivity to underlying tissue properties in the lysolecithin spinal cord model of demyelination and remyelination.

### **7.3 Conclusions**

This chapter focused on correlations between DTI and qMT. We found that in the lysolecithin model  $f$  and FA are strongly correlated. This data indicates that these parameters are likely responding to the same underlying pathology.

## **Chapter Eight: General Discussion**

### **8.1 Introduction**

This thesis sought to characterize the ability of quantitative magnetization transfer (qMT) and diffusion tensor imaging (DTI) to detect demyelination and remyelination in the lysolecithin model of multiple sclerosis (MS). When this work was initiated (September 2014), there were no literature studies carried out using MRI on the modified lysolecithin model developed in the Yong lab (Keough et al., 2015) and no studies of qMT on any lysolecithin model. This chapter will review the novel findings and discuss limitations of this work. Here we will also consider the significance of our finding for MS treatment development and clinical assessment.

### **8.2 Summary of Finding and Discussion**

The first aim of this project was to correlate quantitative magnetization transfer parameters to the myelin and axonal content of lysolecithin lesions found histologically. When this was done, we found that the normalized bound pool fraction had the strongest correlation with the histological myelin staining and that  $T_1$  had the strongest correlation with the histological axon marker. These findings were consistent with the results seen in a similar experiment in the cuprizone model (Thiessen et al., 2013). We believe that by normalizing the qMT data, we were able to compensate for variations in the quality of perfusion and fixation. Fixation has been shown to drop the bound pool fraction by ~50% (Schmierer et al., 2008). Therefore, variations in the quality of fixation would be expected to create noise in this parameter that can be compensated for by normalization to the contralateral side. We did not find an increase in bound pool fraction in our remyelination group compared to our demyelination group. As suggested in Chapter 5 remyelination may not have been extensive enough at 14

dpi for injection. It has been shown that the bound pool fraction can detect extensive but not modest amounts of remyelination (Turati et al., 2015).

qMT is a relatively newer technique and is just beginning to be studied in MS patients. One study demonstrated that qMT parameters were reduced before lesion formation in MS patients (Fazekas et al., 2002). Based off how the different qMT parameters changed pre-lesion formation the paper suggested that the changes seen were not due to blood-brain barrier leakage but were a result of damage to myelin. Additionally, another study which looked at the bound pool fraction ( $f$ ) in progressive acute, gadolinium-enhancing regions of MS patients found that  $f$  was most abnormal at the time of enhancement and followed a pattern of recovery over subsequent months (Levesque et al., 2010b). This study suggested that recovery was due to slow and progressive remyelination which is known to occur in some MS patients. It is known that remyelination does occur in some MS patients and is variable depending on the location of the lesion site (Lassmann, 2013). Taken together this data suggests that if cooperated into routine clinical scans qMT parameters can be used to predict lesion locations and monitor lesions for recovery. However, data from this thesis and other animal model studies (Turati et al., 2015) suggest that a lack of recovery in qMT parameters should be interpreted carefully. In such a situation it does not mean there is a complete lack of remyelination but rather the lack of extensive remyelination.

The second aim of this project was to correlate diffusion tensor imaging parameters to the myelin and axonal content of lysolecithin lesions found histologically. When this was done, we found that the strongest correlation was seen between normalized RA and histological staining for myelin. RA is not assessed as often as FA in studies of demyelination and remyelination. One study of age-related changes in different anatomical regions of the brain found that FA could underestimate changes in myelination that were detected with RA (Lobel et al., 2009). This paper suggested that this was because RA can complement FA in

future studies of myelination (Lobel et al., 2009), a suggestion that is supported by the results of this thesis.

We also found correlations between histological axon staining and both FA and RD. These correlations were in the range of those previously seen and thus are not surprising. It was, however, surprising that a correlation was not observed between AD and axon content. Previous work has shown that AD is reduced throughout all of the white matter in EAE mice and correlates with a decrease in SMI312 staining (Budde et al., 2008; Budde et al., 2009; Nathoo et al., 2014a). It is possible that we did not see similar correlations because of this work was done *ex vivo*; *in vivo* work has been shown to be a better indicator of axial diffusivity compared to *ex vivo* work (Zhang et al., 2012b). In studies of MS patients, changes in AD have been variable with some studies reporting a decrease (Tillema et al., 2012), others an increase (Liu et al., 2012), and others showing no alterations (Naismith et al., 2010; Nathoo et al., 2014a) The reason for this inconsistency remains to be explored but could be due to disease duration or the different forms of MS.

A major finding of this thesis was that normalized linear anisotropy (CL) was the only parameter able to detect a statistically significant difference between 7 dpi and 14 dpi lesions. This parameter along with spherical anisotropy (CS) and planar anisotropy (CP) are not as often assessed as FA, RD, AD and MD in DTI studies. Based on this thesis DTI parameter such as CL, CP, and CS should be further explored in animal models of de- and remyelination as well as MS patient studies.

Finally, we found high correlations between FA and the bound pool fraction. As mentioned in Chapter 7 this is contrary to previously published results. This finding is likely due to the higher directional coherence of fibers in the spinal cord compared to the brain, where the previous studies were done. As previously mentioned, a study by Stikov, which looked at the correlation between  $f$  and diffusion anisotropy in different regions of the brain, found that there was a

higher correlation between FA and  $f$  could in areas with high directional coherence (Stikov et al., 2011). In this paper, they suggest that this difference is caused by a greater overlap in the sensitivity of  $f$  and diffusion anisotropy to underlying tissue properties in areas of high directional coherence (Stikov et al., 2011). The results of this thesis are in line with this theory.

Finally, although the bound pool fraction has a higher correlation to myelin we did not see any recovery with remyelination at 14 dpi, whereas the DTI imaging parameters seem to recover at 14 dpi partially. Many of the DTI parameters at 14 dpi are not significantly different from the naïve group, although the 7 dpi groups are. Additionally, the normalized CL is significantly different between 7 and 14 dpi lesions and between 14 and 7 dpi lesions. Thus this parameter appears to be able to differentiate between remyelination and demyelination. These results indicate that even though the bound pool fraction might have a higher specificity to myelin, DTI parameters may be more sensitive to changes in myelin content in the lysolecithin model.

Based on the results of this thesis, in future pre-clinical trials of remyelination promoting therapeutics in the lysolecithin model DTI could provide a useful outcome measure.

Taken together, the findings from this thesis provide a foundation for pursuing future studies with DTI and qMT in the lysolecithin model of MS. Particularly for studying the effects of treatments that inhibit demyelination and promote remyelination in this model.

### **8.3 Limitations of the Study**

The lysolecithin has many advantages, including that it has a well-defined and short timeline for de- and remyelination. Also, it is a model in which many potential therapies that promote remyelination for the treatment of MS are currently being tested (Keough et al., 2015; Keough et al., 2016). These reasons

are why this model was used to investigate the ability of DTI and qMT parameters to distinguish between naïve, demyelination and remyelination. However, it is important to remember that lysolecithin is a relatively simple model that does not mimic MS. MS has a much more complicated underlying pathophysiology and thus more potential confounding factors can influence MRI parameters in MS than in the lysolecithin model. A fact that should be kept in mind when considering the transferability of our results to clinical research.

Additionally, we did not investigate the ability of qMT and DTI to detect changes to tissue pathology in different areas of the CNS. MS lesions are not restricted to the spinal cord but occur throughout the CNS (Compston and Coles, 2002). It is well known that diffusion parameters, in particular, are affected by the degree of fiber coherence (Stikov et al., 2011). Therefore, the diffusion results obtained are unlikely to be generalizable to different areas of the CNS.

Another obvious limitation of this work is that the MRI data was acquired *ex vivo*. The process of chemical fixation does change tissue MRI properties. Fixation can cause a decrease in  $T_1$  that is greater in gray matter than in white matter (Tovi and Ericsson, 1992; D'Arceuil et al., 2007). These changes to  $T_1$  result in a minimal white matter contrast and would likely affect the correlations found between  $T_1$  and myelin in this study. Additionally, formalin fixation has been shown to cause a 50% increase in the  $f$  (Schmierer et al., 2008). Regarding diffusion, the apparent diffusion coefficient (ADC) values are substantially decreased in *ex vivo* imaging compared to *in vivo* values, with a greater change in white matter than in gray matter (D'Arceuil et al., 2007). A large part of this reduction in ADC and other diffusion parameters is due to brain death and changes in temperature. However, fixation has no effect on anisotropic measures (D'Arceuil et al., 2007). The length of time between fixation and imaging could have contributed to some of the variability seen in the MRI data.

Despite the attempts to increase SNR by using the cryoprobe and doing this research *ex vivo* we still saw high variability in our MRI parameters. The

standard deviation of  $T_1$  for all groups was between 0.013-0.13s. The standard deviation of the  $T_1$  calculated by controls by Thiessen et al., 2013 is much lower (0.007s) than that seen here. This difference in standard deviation is likely, in part, because the Thiessen paper used a resolution of  $98 \times 98 \times 750 \mu\text{m}^3$  whereas the data acquired here used a resolution of  $98 \times 98 \times 500 \mu\text{m}^3$ . This increase in resolution decreases the amount of tissue signal contributing to each voxel, and this would reduce the amount of signal per voxel and the overall signal to noise causing greater variability in data. Additionally, the Thiessen paper was able to average all voxels covering the corpus callosum whereas the data presented here averages approximately ten voxels per region of interest due to the small lysolecithin lesions. The lower number of voxels used to average would help explain the greater variability between the two sets of data. A paper looking at the feasibility of *in vivo* MRI on mouse spinal cord at 9.4T had a higher standard deviation within control white matter (0.19s) than is seen here (Bilgen et al., 2005), indicating that the variability in  $T_1$  seen here is not abnormal for mouse spinal cord MRI.

The standard deviation of the bound pool fraction for all groups was between 0.017-0.037. The standard deviation of  $f$  for controls in the Thiessen paper was much lower (0.003). The higher variability seen in this study could be for the same reasons as the greater variability in  $T_1$  mentioned above. To the best of my knowledge qMT has not previously been performed on mouse spinal cord and therefore there is no literature data for comparison. However, data on  $f$  reported for rat spinal cord does have a higher standard deviation (0.01-0.02) (Dula et al., 2010) than that seen in the Thiessen et al., 2013 supporting the idea that the increased variability is due to the decreased size of the tissue being imaged.

Although the variability in this study is high, it does not appear to be abnormally high for mouse spinal cord imaging.

## 8.4 Significance of Findings

The main significance of this study is that it demonstrates that DTI parameters can be used as an outcome measure in pre-clinical and clinical trials of therapies that inhibit demyelination and promote remyelination.

Significant advances are taking place in the development of therapeutics for MS. In particular therapies are moving past the traditional immunomodulators and towards medications aimed at promoting remyelination or neuroprotection (Nathoo et al., 2014b). MRI is frequently used as a primary outcome measure in clinical trials (Filippi and Rocca, 2011; Nathoo et al., 2014a) and new therapeutics are tested in animal models first. Thus it is logical that MRI, such as qMT and DTI be incorporated into preclinical studies assessing these therapies. Doing so will help determine what types of changes can be expected of MRI parameters in clinical trials as these treatments begin to be tested at a clinical level.

Additionally, diffusion tensor imaging and magnetization transfer are currently being used as outcomes measures in clinical trials of MS therapies and to study the development of MS pathology (Levesque et al., 2010b; Temel et al., 2013; Mallik et al., 2014). To fully and correctly interpret the results from these experiments we require analyses that assess the correlation between qMT and DTI and pathology. This thesis is one such experiment that adds to our knowledge and understanding of the correlation between DTI and qMT parameters and pathology. It does so by using a model that has not previously been used to study these parameters. Also, it adds to our understanding of how these parameters, particularly DTI parameters, may have differential sensitivity to pathology depending on the location of CNS being assessed.

Thus, knowledge created from this thesis may help guide future studies of MS therapeutics at both a pre-clinical and clinical level.

## Chapter Nine: Conclusions and Future Directions

### 9.1 Future Directions

This work demonstrates that MRI can be used to detect differences in the myelin content of lysolecithin lesions. To build on the work done in this thesis multiple future studies can and should be conducted. First, this data demonstrated that qMT and DTI parameters could detect lysolecithin lesions in perfusion fixed tissue. The next step would be to compare these sequences between unfixed tissue and fixed tissue imaged post-mortem. Such an experiment would provide a better understanding of how fixation affected the data presented in this thesis. Although some work along this line has been done previously (D'Arceuil et al., 2007; Kim et al., 2007; Schmierer et al., 2008), such a study has not been done in the lysolecithin model.

Following this, another area for investigation could be to determine if these sequences can be run in the lysolecithin model *in vivo*. Doing so would involve overcoming numerous technical challenges. One such problem comes from the location of the lysolecithin lesion. The thoracic spinal cord is close to the lungs and heart which produce lots of motion making *in vivo* MRI imaging of this area difficult. Lysolecithin lesions can, however, be produced in different CNS regions including, but not limited to, the lumbar spinal cord and the corpus callosum (Keough et al., 2015). Although these locations involve a more invasive procedure, they would make *in vivo* MRI imaging more feasible.

Additionally, the sequences would have to be shortened for *in vivo* imaging. It is highly unlikely both DTI and qMT could be done using the current protocol within a reasonable imaging time. *In vivo* imaging is best kept under 2 hours in order to minimize stress to the animal. The current combined time of DTI and qMT imaging for this thesis was 3 hours and 35 minutes with the cryoprobe. It is possible that the DTI and qMT data acquisition times could be shortened by decreasing the number of directions acquired and the number of off-resonance images required, respectively. It would also be necessary to

ensure that such changes did not result in sampling bias or poor fitting which would in turn result in errors in the quantitative MRI. We would need to modify the cryoprobe such that it could be installed “upside down”. The current geometry would have the mouse dorsal side up, which results in significant motion in the cord—degrading the images. Without such a modification, we would need to use a volume coil which has much lower SNR compared with the cryoprobe. Thus there would be a need for an increase in averages, again making it difficult to achieve this imaging *in vivo*. Therefore, two studies would have to be done, one for each sequence, or rapid acquisition protocols would need to be developed.

To the best of my knowledge, only two studies have been performed where qMT was done *in vivo* in animal models (Rausch et al., 2009; Turati et al., 2015). The lack of studies is likely due to the large number of images required to calculate magnetization transfer accurately. A large number of images results in a long sequence acquisition time which makes *in vivo* imaging difficult to perform. However, these studies demonstrate that it is possible to image mouse CNS *in vivo* using qMT imaging.

Although *in vivo* diffusion tensor imaging of mouse spinal cord is difficult, due to the size of the cord and sensitivity of DTI to motion noise, it is not impossible (Tu et al., 2014). Like qMT, for an *in vivo* study of DTI correlations to myelin and axon content of lysolecithin lesions the lesions themselves would have to be produced in a different location. In the case of DTI, it would be possible to run a correlation study where lysolecithin lesions are produced in the lumbar spinal cord of mice.

Finally, studies could be done, where DTI and/or qMT imaging parameters are used as outcome measures for remyelinating treatment tested in the lysolecithin model. Such therapies include but are not limited to exercise (Jensen and Yong, 2016), oxygen therapy (Desai et al., 2016) and inhibitors of chondroitin sulfate proteoglycan synthesis (Keough et al., 2016). These are

therapeutic avenues currently being explored in the Yong and Dunn labs. Since MRI is the main outcome measure in clinical trials, the inclusion of the MRI parameters evaluated in this thesis as outcome measures in pre-clinical studies of MS therapies, will ease the transition of these therapies from the pre-clinical to the clinical setting.

## **9.2 Conclusions**

In summary, we characterized the DTI and qMT phenotypes in a mouse demyelination and remyelination model. Our results indicate that out of the measured parameters, the MRI parameter with the strongest correlation to myelin is the bound pool fraction and the MRI parameter with the strongest correlation to axons is  $T_1$ . This data matches previously reported results seen in the cuprizone model of MS (Thiessen et al., 2013). Additionally, it appears that DTI parameters are sensitive to remyelination in the lysolecithin model while qMT did not seem to detect remyelination. This thesis emphasizes the need to fully understand the specificity of different quantitative MRI measures to myelin and highlights the need for further work on diffusion MRI for spinal cord imaging. There is a high potential for quantitative MRI parameters to be used as outcome measures in pre-clinical and clinical trials of therapeutics promoting remyelination in the CNS.

## References

- (1998) Burden of illness of multiple sclerosis: Part I: Cost of illness. The Canadian Burden of Illness Study Group. *The Canadian journal of neurological sciences Le journal canadien des sciences neurologiques* 25:23-30.
- Adams RD, Kubik CS (1952) The morbid anatomy of the demyelinating disease. *The American journal of medicine* 12:510-546.
- Agrawal SM, Silva C, Tourtellotte WW, Yong VW (2011) EMMPRIN: a novel regulator of leukocyte transmigration into the CNS in multiple sclerosis and experimental autoimmune encephalomyelitis. *The Journal of neuroscience : the official journal of the Society for Neuroscience* 31:669-677.
- Antel J, Antel S, Caramanos Z, Arnold DL, Kuhlmann T (2012) Primary progressive multiple sclerosis: part of the MS disease spectrum or separate disease entity? *Acta neuropathologica* 123:627-638.
- Azin M, Mirnajafi-Zadeh J, Javan M (2015) Fibroblast Growth Factor-2 Enhanced The Recruitment of Progenitor Cells and Myelin Repair in Experimental Demyelination of Rat Hippocampal Formations. *Cell journal* 17:540-456.
- Bagnato F, Jeffries N, Richert ND, Stone RD, Ohayon JM, McFarland HF, Frank JA (2003) Evolution of T1 black holes in patients with multiple sclerosis imaged monthly for 4 years. *Brain : a journal of neurology* 126:1782-1789.
- Bammer R, Augustin M, Strasser-Fuchs S, Seifert T, Kapeller P, Stollberger R, Ebner F, Hartung HP, Fazekas F (2000) Magnetic resonance diffusion tensor imaging for characterizing diffuse and focal white matter abnormalities in multiple sclerosis. *Magnetic resonance in medicine* 44:583-591.
- Barkhof F, Scheltens P, Frequin ST, Nauta JJ, Tas MW, Valk J, Hommes OR (1992) Relapsing-remitting multiple sclerosis: sequential enhanced MR imaging vs clinical findings in determining disease activity. *AJR American journal of roentgenology* 159:1041-1047.
- Barnett MH, Prineas JW (2004) Relapsing and remitting multiple sclerosis: pathology of the newly forming lesion. *Annals of neurology* 55:458-468.
- Basser PJ (1993) Cable equation for a myelinated axon derived from its microstructure. *Medical & biological engineering & computing* 31 Suppl:92.
- Basser PJ, Jones DK (2002) Diffusion tensor MRI: theory, experimental design and data analysis—a technical review. *Diffusion tensor MRI: theory, experimental design and data analysis—a technical review*.
- Basser PJ, Mattiello J, LeBihan DC (1994a) MR diffusion tensor spectroscopy and imaging. *Biophysical journal* 66:259-267.
- Basser PJ, Mattiello J, LeBihan D (1994b) Estimation of the effective self-diffusion tensor from the NMR spin echo. *Journal of magnetic resonance Series B* 103:247-254.

- Batoulis H, Recks MS, Addicks K, Kuerten S (2011) Experimental autoimmune encephalomyelitis--achievements and prospective advances. *APMIS : acta pathologica, microbiologica, et immunologica Scandinavica* 119:819-830.
- Baxter AG (2007) The origin and application of experimental autoimmune encephalomyelitis. *Nature reviews Immunology* 7:904-912.
- Beaulieu C (2002) The basis of anisotropic water diffusion in the nervous system " a technical review. *NMR in Biomedicine* 15:435-455.
- Beck CA, Metz LM, Svenson LW, Patten SB (2005) Regional variation of multiple sclerosis prevalence in Canada. *Multiple sclerosis (Houndmills, Basingstoke, England)* 11:516-519.
- Bellin M-FF, Van Der Molen AJ (2008) Extracellular gadolinium-based contrast media: an overview. *European journal of radiology* 66:160-167.
- Berard JL, Wolak K, Fournier S, David S (2010) Characterization of relapsing-remitting and chronic forms of experimental autoimmune encephalomyelitis in C57BL/6 mice. *Glia* 58:434-445.
- Bieber AJ, Kerr S, Rodriguez M (2003) Efficient central nervous system remyelination requires T cells. *Annals of neurology*.
- Bilgen M, Al-Hafez B, Berman NE, Festoff BW (2005) Magnetic resonance imaging of mouse spinal cord. *Magnetic resonance in medicine* 54:1226-1231.
- Bitsch A, Schuchardt J, Bunkowski S, Kuhlmann T, Brück W (2000) Acute axonal injury in multiple sclerosis. Correlation with demyelination and inflammation. *Brain : a journal of neurology* 123 ( Pt 6):1174-1183.
- Bjartmar C, Wujek JR, Trapp BD (2003) Axonal loss in the pathology of MS: consequences for understanding the progressive phase of the disease. *Journal of the neurological sciences* 206:165-171.
- Blakemore WF, Franklin RJ (2008) Remyelination in experimental models of toxin-induced demyelination. *Current topics in microbiology and immunology* 318:193-212.
- Bloch F (1946) Nuclear induction. *Physical review*.
- Bo L, Geurts JJ, van der Valk P, Polman C, Barkhof F (2007) Lack of correlation between cortical demyelination and white matter pathologic changes in multiple sclerosis. *Archives of neurology* 64:76-80.
- Bodini B, Louapre C, Stankoff B (2015) Advanced imaging tools to investigate multiple sclerosis pathology. *Presse medicale (Paris, France : 1983)* 44:67.
- Bramow S, Frischer JM, Lassmann H, Koch-Henriksen N, Lucchinetti CF, Sorensen PS, Laursen H (2010) Demyelination versus remyelination in progressive multiple sclerosis. *Brain : a journal of neurology* 133:2983-2998.
- Brochet B, Dousset V (1999) Pathological correlates of magnetization transfer imaging abnormalities in animal models and humans with multiple sclerosis. *Neurology* 53:7.

- Brownell B, Hughes JC (1962) The distribution of plaques in the cerebrum in multiple sclerosis. *Journal of neurology, neurosurgery, and psychiatry* 25:315-320.
- Buck D, Hemmer B (2011) Treatment of multiple sclerosis: current concepts and future perspectives. *Journal of neurology* 258:1747-1762.
- Budde MD, Xie M, Cross AH, Song S-KKC (2009) Axial diffusivity is the primary correlate of axonal injury in the experimental autoimmune encephalomyelitis spinal cord: a quantitative pixelwise analysis. *The Journal of neuroscience : the official journal of the Society for Neuroscience* 29:2805-2813.
- Budde MD, Kim JH, Liang H-FF, Russell JH, Cross AH, Song S-KKC (2008) Axonal injury detected by in vivo diffusion tensor imaging correlates with neurological disability in a mouse model of multiple sclerosis. *NMR in Biomedicine* 21:589-597.
- Cercignani M, Inglese M, Pagani E, Comi G, Filippi M (2001) Mean diffusivity and fractional anisotropy histograms of patients with multiple sclerosis. *AJNR American journal of neuroradiology* 22:952-958.
- Cercignani M, Symms MR, Schmierer K, Boulby PA, Tozer DJ, Ron M, Tofts PS, Barker GJ (2005) Three-dimensional quantitative magnetisation transfer imaging of the human brain. *NeuroImage* 27:436-441.
- Chen JT, Collins DL, Atkins HL, Freedman MS, Arnold DL, Group C (2008) Magnetization transfer ratio evolution with demyelination and remyelination in multiple sclerosis lesions. *Annals of neurology* 63:254-262.
- Compston A, Coles A (2002) Multiple sclerosis. *Lancet (London, England)* 359:1221-1231.
- Cotton F, Weiner HL, Jolesz FA, Guttmann CR (2003) MRI contrast uptake in new lesions in relapsing-remitting MS followed at weekly intervals. *Neurology* 60:640-646.
- D'Arceuil HE, Westmoreland S, de Crespigny AJ (2007) An approach to high resolution diffusion tensor imaging in fixed primate brain. *NeuroImage* 35:553-565.
- Dal Canto MC, Kim BS, Miller SD, Melvold RW (1996) Theiler's Murine Encephalomyelitis Virus (TMEV)-Induced Demyelination: A Model for Human Multiple Sclerosis. *Methods (San Diego, Calif)* 10:453-461.
- Dalton CM, Brex PA, Miszkiewicz KA (2002) Application of the new McDonald criteria to patients with clinically isolated syndromes suggestive of multiple sclerosis. *Annals of Neurology*.
- DeBoy CA, Zhang J, Dike S, Shats I, Jones M, Reich DS, Mori S, Nguyen T, Rothstein B, Miller RH, Griffin JT, Kerr DA, Calabresi PA (2007) High resolution diffusion tensor imaging of axonal damage in focal inflammatory and demyelinating lesions in rat spinal cord. *Brain : a journal of neurology* 130:2199-2210.

- Deloire-Grassin MS, Brochet B, Quesson B, Delalande C, Dousset V, Canioni P, Petry KG (2000) In vivo evaluation of remyelination in rat brain by magnetization transfer imaging. *Journal of the neurological sciences* 178:10-16.
- Dendrou CA, Fugger L, Friese MA (2015) Immunopathology of multiple sclerosis. *Nature reviews Immunology* 15:545-558.
- Denic A, Johnson AJ, Bieber AJ, Warrington AE, Rodriguez M, Pirko I (2011) The relevance of animal models in multiple sclerosis research. *Pathophysiology : the official journal of the International Society for Pathophysiology / ISP* 18:21-29.
- Desai RA, Davies AL, Tachrount M, Kasti M (2016) Cause and prevention of demyelination in a model multiple sclerosis lesion. *Annals of*
- Dousset V, Brochet B, Vital A, Gross C, Benazzouz A, Boullerne A, Bidabe AM, Gin AM, Caille JM (1995) Lysolecithin-induced demyelination in primates: preliminary in vivo study with MR and magnetization transfer. *AJNR American journal of neuroradiology* 16:225-231.
- Dula AN, Gochberg DF, Valentine HL, Valentine WM, Does MD (2010) Multiexponential T2, magnetization transfer, and quantitative histology in white matter tracts of rat spinal cord. *Magnetic resonance in medicine* 63:902-909.
- Duncan ID, Brower A, Kondo Y, Curlee JF, Schultz RD (2009) Extensive remyelination of the CNS leads to functional recovery. *Proceedings of the National Academy of Sciences of the United States of America* 106:6832-6836.
- Dutta R, Trapp BD (2011) Mechanisms of neuronal dysfunction and degeneration in multiple sclerosis. *Progress in neurobiology* 93:1-12.
- Ebers GC (2004) Natural history of primary progressive multiple sclerosis. *Multiple sclerosis (Houndmills, Basingstoke, England)* 10 Suppl 1.
- Elliott C, Lindner M, Arthur A, Brennan K, Jarius S, Hussey J, Chan A, Stroet A, Olsson T, Willison H, Barnett SC, Meinl E, Linington CC (2012) Functional identification of pathogenic autoantibody responses in patients with multiple sclerosis. *Brain : a journal of neurology* 135:1819-1833.
- Fazekas F, Ropele S, Enzinger C, Seifert T, Strasser-Fuchs S (2002) Quantitative magnetization transfer imaging of pre-lesional white-matter changes in multiple sclerosis. *Multiple sclerosis (Houndmills, Basingstoke, England)* 8:479-484.
- Fazekas F, Barkhof F, Filippi M, Grossman RI, Li DK, McDonald WI, McFarland HF, Paty DW, Simon JH, Wolinsky JS, Miller DH (1999) The contribution of magnetic resonance imaging to the diagnosis of multiple sclerosis. *Neurology* 53:448-456.
- Filippi M (2000) The role of magnetization transfer and diffusion-weighted MRI in the understanding of multiple sclerosis evolution. *Neurological sciences* :

- official journal of the Italian Neurological Society and of the Italian Society of Clinical Neurophysiology 21:81.
- Filippi M, Inglese M (2001) Overview of diffusion-weighted magnetic resonance studies in multiple sclerosis. *Journal of the neurological sciences* 186 Suppl 1:43.
- Filippi M, Rocca MA (2011) MR imaging of multiple sclerosis. *Radiology* 259:659-681.
- Filippi M, Rocca MA (2012) The neurologist's dilemma: MS is a grey matter disease that standard clinical and MRI measures cannot assess adequately--no. *Multiple sclerosis (Houndmills, Basingstoke, England)* 18:557-558.
- Filippi M, Cercignani M, Inglese M, Horsfield MA, Comi G (2001) Diffusion tensor magnetic resonance imaging in multiple sclerosis. *Neurology* 56:304-311.
- Fischer MT, Sharma R, Lim JL, Haider L, Frischer JM, Drexhage J, Mahad D, Bradl M, van Horssen J, Lassmann HC (2012) NADPH oxidase expression in active multiple sclerosis lesions in relation to oxidative tissue damage and mitochondrial injury. *Brain : a journal of neurology* 135:886-899.
- Fischer MT, Wimmer I, Häftberger R, Gerlach S, Haider L, Zrzavy T, Hametner S, Mahad D, Binder CJ, Krumbholz M, Bauer J, Bradl M, Lassmann HC (2013) Disease-specific molecular events in cortical multiple sclerosis lesions. *Brain : a journal of neurology* 136:1799-1815.
- Freund J, McDermott K (1942) Sensitization to horse serum by means of adjuvants. *Experimental Biology and Medicine* 49:548-553.
- Fujinami RS, Oldstone MB (1985) Amino acid homology between the encephalitogenic site of myelin basic protein and virus: mechanism for autoimmunity. *Science (New York, NY)* 230:1043-1045.
- Gareau PJ, Rutt BK, Karlik SJ, Mitchell JR (2000) Magnetization transfer and multicomponent T2 relaxation measurements with histopathologic correlation in an experimental model of MS. *Journal of magnetic resonance imaging : JMRI* 11:586-595.
- Ge Y (2006) Multiple sclerosis: the role of MR imaging. *AJNR American journal of neuroradiology* 27:1165-1176.
- Genain CP, Cannella B, Hauser SL, Raine CS (1999) Identification of autoantibodies associated with myelin damage in multiple sclerosis. *Nature medicine* 5:170-175.
- Geurts JJ, Calabrese M, Fisher E, Rudick RA (2013) Measurement and clinical effect of grey matter pathology in multiple sclerosis. *The Lancet Neurology* 11:1082-1092.
- Giacomini PS, Levesque IR, Ribeiro L, Narayanan S, Francis SJ, Pike GB, Arnold DL (2009) Measuring demyelination and remyelination in acute multiple sclerosis lesion voxels. *Archives of neurology* 66:375-381.
- Goldenberg MM (2012) Multiple sclerosis review. *P T* 37:175-184.

- Goodin DS, Frohman EM, Garmany GP, Halper J, Likosky WH, Lublin FD, Silberberg DH, Stuart WH, van den Noort S, and of the o, the for Guidelines T (2002) Disease modifying therapies in multiple sclerosis: report of the Therapeutics and Technology Assessment Subcommittee of the American Academy of Neurology and the MS Council for Clinical Practice Guidelines. *Neurology* 58:169-178.
- Gouw AA, Seewann A, Vrenken H, van der Flier WM, Rozemuller JM, Barkhof F, Scheltens P, Geurts JJ (2008) Heterogeneity of white matter hyperintensities in Alzheimer's disease: post-mortem quantitative MRI and neuropathology. *Brain : a journal of neurology* 131:3286-3298.
- Graca DL, Blakemore WF (1986) Delayed remyelination in rat spinal cord following ethidium bromide injection. *Neuropathology and applied neurobiology* 12:593-605.
- Graham SJ, Henkelman RM (1999) Pulsed magnetization transfer imaging: evaluation of technique. *Radiology* 212:903-910.
- Grossman RI, Barkhof F, Filippi M (2000) Assessment of spinal cord damage in MS using MRI. *Journal of the neurological sciences* 172 Suppl 1:9.
- Guo AC, Jewells VL, Provenzale JM (2001) Analysis of normal-appearing white matter in multiple sclerosis: comparison of diffusion tensor MR imaging and magnetization transfer imaging. *AJNR American journal of neuroradiology* 22:1893-1900.
- Hagemeyer K, Bruck W, Kuhlmann T (2012) Multiple sclerosis - remyelination failure as a cause of disease progression. *Histology and histopathology* 27:277-287.
- Hall SM (1972) The effect of injections of lysophosphatidyl choline into white matter of the adult mouse spinal cord. *Journal of Cell Science* 10:535-546.
- Hauser SL, Oksenberg JR (2006) The neurobiology of multiple sclerosis: genes, inflammation, and neurodegeneration. *Neuron* 52:61-76.
- Hemm RD, Carlton WW, Welser JR (1971) Ultrastructural changes of cuprizone encephalopathy in mice. *Toxicology and applied pharmacology* 18:869-882.
- Hemmer B, Nessler S, Zhou D, Kieseier B, Hartung H-PP (2006) Immunopathogenesis and immunotherapy of multiple sclerosis. *Nature clinical practice Neurology* 2:201-211.
- Henderson AP, Barnett MH, Parratt JD, Prineas JW (2009) Multiple sclerosis: distribution of inflammatory cells in newly forming lesions. *Annals of neurology* 66:739-753.
- Henkelman RM, Huang X, Xiang QS, Stanisz GJ, Swanson SD, Bronskill MJ (1993) Quantitative interpretation of magnetization transfer. *Magnetic resonance in medicine* 29:759-766.
- Hofman FM, Hinton DR, Johnson K, Merrill JC (1989) Tumor necrosis factor identified in multiple sclerosis brain. *The Journal of experimental medicine* 170:607-612.

- Hornak JP (1996) The Basics of MRI.
- Huang BQ, Yeung EC (2015) Chemical and Physical Fixation of Cells and Tissues: An Overview. *Plant Microtechniques and Protocols*.
- Irvine KA, Blakemore WF (2008) Remyelination protects axons from demyelination-associated axon degeneration. *Brain : a journal of neurology* 131:1464-1477.
- Janve VA, Zu Z, Yao S-YY, Li K, Zhang FL, Wilson KJ, Ou X, Does MD, Subramaniam S, Gochberg DFC (2013) The radial diffusivity and magnetization transfer pool size ratio are sensitive markers for demyelination in a rat model of type III multiple sclerosis (MS) lesions. *NeuroImage* 74:298-305.
- Jelescu IO, Zurek M, Winters KV, Veraart J, Rajaratnam A, Kim NS, Babb JS, Shepherd TM, Novikov DS, Kim SG, Fieremans EC (2016) In vivo quantification of demyelination and recovery using compartment-specific diffusion MRI metrics validated by electron microscopy. *NeuroImage* 132:104-114.
- Jensen SK, Yong VW (2016) Activity-Dependent and Experience-Driven Myelination Provide New Directions for the Management of Multiple Sclerosis. *Trends in neurosciences*.
- Joanna P, Inga G, Dagmara M-GG, Anna Co (2015) Evolution of diagnostic criteria for multiple sclerosis. *Neurologia i neurochirurgia polska* 49:313-321.
- Jonkman LE, Soriano AL, Amor S, Barkhof F, van der Valk P, Vrenken H, Geurts JJC (2015) Can MS lesion stages be distinguished with MRI? A postmortem MRI and histopathology study. *Journal of neurology* 262:1074-1080.
- Julian LJ, Vella L, Vollmer T, Hadjimichael O, Mohr DC (2008) Employment in multiple sclerosis. Exiting and re-entering the work force. *J Neurol* 255:1354-1360.
- Keough MB, Yong VC (2013) Remyelination therapy for multiple sclerosis. *Neurotherapeutics : the journal of the American Society for Experimental NeuroTherapeutics* 10:44-54.
- Keough MB, Jensen SK, Yong VW (2015) Experimental demyelination and remyelination of murine spinal cord by focal injection of lysolecithin. *J Vis Exp*.
- Keough MB, Rogers JA, Zhang P, Jensen SK, Stephenson EL, Chen T, Hurlbert MG, Lau LW, Rawji KS, Plemel JR, Koch M, Ling C-CC, Yong VC (2016) An inhibitor of chondroitin sulfate proteoglycan synthesis promotes central nervous system remyelination. *Nature communications* 7:11312.
- Kiernan JA (2000) Formaldehyde, formalin, paraformaldehyde and glutaraldehyde: what they are and what they do. *Microscopy today*.

- Kim J, Trinkaus K, Ozcan A, Budde MD, Song S (2007) Postmortem delay does not change regional diffusion anisotropy characteristics in mouse spinal cord white matter. *NMR in Biomedicine* 20:352-359.
- Klawiter EC, Piccio L, Lyons J-AA, Mikesell R, O'Connor KC, Cross AHC (2010) Elevated intrathecal myelin oligodendrocyte glycoprotein antibodies in multiple sclerosis. *Archives of neurology* 67:1102-1108.
- Klawiter EC, Schmidt RE, Trinkaus K, Liang H-FF, Budde MD, Naismith RT, Song S-KK, Cross AH, Benzinger TLC (2011) Radial diffusivity predicts demyelination in ex vivo multiple sclerosis spinal cords. *NeuroImage* 55:1454-1460.
- Klawiter ECC (2013) Current and new directions in MRI in multiple sclerosis. *Continuum (Minneapolis, Minn)* 19:1058-1073.
- Kolasinski J, Stagg CJ, Chance SA, Deluca GC, Esiri MM, Chang E-HH, Palace JA, McNab JA, Jenkinson M, Miller KL, Johansen-Berg HC (2012) A combined post-mortem magnetic resonance imaging and quantitative histological study of multiple sclerosis pathology. *Brain : a journal of neurology* 135:2938-2951.
- Komoly S, Jeyasingham MD, Pratt OE, Lantos PL (1987) Decrease in oligodendrocyte carbonic anhydrase activity preceding myelin degeneration in cuprizone induced demyelination. *Journal of the neurological sciences* 79:141-148.
- Kornblith AB, La Rocca NG, Baum HM (1986) Employment in individuals with multiple sclerosis. *Int J Rehabil Res* 9:155-165.
- Kornek B, Lassmann H (1999) Axonal pathology in multiple sclerosis. A historical note. *Brain pathology (Zurich, Switzerland)* 9:651-656.
- Kuhlmann T, Lingfeld G, Bitsch A, Schuchardt J, Brück W (2002) Acute axonal damage in multiple sclerosis is most extensive in early disease stages and decreases over time. *Brain : a journal of neurology* 125:2202-2212.
- Kumar M, Nasrallah IM, Kim S, Ittyerah R, Pickup S, Li J, Parente MK, Wolfe JH, Poptani HC (2014) High-resolution magnetic resonance microscopy and diffusion tensor imaging to assess brain structural abnormalities in the murine mucopolysaccharidosis VII model. *Journal of neuropathology and experimental neurology* 73:39-49.
- Kumar R, Nguyen HD, Macey PM, Woo MA, Harper RMC (2012) Regional brain axial and radial diffusivity changes during development. *Journal of neuroscience research* 90:346-355.
- Lampasona V, Franciotta D, Furlan R, Zanaboni S, Fazio R, Bonifacio E, Comi G, Martino G (2004) Similar low frequency of anti-MOG IgG and IgM in MS patients and healthy subjects. *Neurology* 62:2092-2094.
- LaRocca N, Kalb R, Kendall P, Scheinberg L (1982) The role of disease and demographic factors in the employment of patients with multiple sclerosis. *Arch Neurol* 39:256.

- Lassmann H (2003) Axonal injury in multiple sclerosis. *Journal of neurology, neurosurgery, and psychiatry* 74:695-697.
- Lassmann H (2013) Pathology and disease mechanisms in different stages of multiple sclerosis. *Journal of the neurological sciences* 333:1-4.
- Laule C, Vavasour IM, Kolind SH, Li DK, Traboulsee TL, Moore GR, MacKay AL (2007) Magnetic resonance imaging of myelin. *Neurotherapeutics : the journal of the American Society for Experimental NeuroTherapeutics* 4:460-484.
- Le Bihan D, Mangin JF, Poupon C (2001) Diffusion tensor imaging: concepts and applications. *MRI resonance imaging*.
- Levesque IR, Sled JG, Narayanan S, Giacomini PS, Ribeiro LT, Arnold DL, Pike GB (2010a) Reproducibility of quantitative magnetization-transfer imaging parameters from repeated measurements. *Magnetic resonance in medicine* 64:391-400.
- Levesque IR, Giacomini PS, Narayanan S, Ribeiro LT, Sled JG, Arnold DL, Pike GB (2010b) Quantitative magnetization transfer and myelin water imaging of the evolution of acute multiple sclerosis lesions. *Magnetic resonance in medicine* 63:633-640.
- Li K, Dortch RD, Welch EB, Bryant ND, Buck AK, Towse TF, Gochberg DF, Does MD, Damon BM, Park JHC (2014) Multi-parametric MRI characterization of healthy human thigh muscles at 3.0 T - relaxation, magnetization transfer, fat/water, and diffusion tensor imaging. *NMR in Biomedicine* 27:1070-1084.
- Libbey JE, McCoy LL, Fujinami RS (2007) Molecular mimicry in multiple sclerosis. *International review of neurobiology* 79:127-147.
- Liu Y, Duan Y, He Y, Yu C, Wang J, Huang J, Ye J, Parizel PM, Li K, Shu N (2012) Whole brain white matter changes revealed by multiple diffusion metrics in multiple sclerosis: a TBSS study. *European journal of radiology* 81:2826-2832.
- Lobel U, Sedlacik J, Gullmar D, Kaiser WA, Reichenbach JrRR, Mentzel H-JJ (2009) Diffusion tensor imaging: the normal evolution of ADC, RA, FA, and eigenvalues studied in multiple anatomical regions of the brain. *Neuroradiology* 51:253-263.
- Lucchinetti C, Brück W, Parisi J, Scheithauer B, Rodriguez M, Lassmann H (2000) Heterogeneity of multiple sclerosis lesions: implications for the pathogenesis of demyelination. *Annals of neurology* 47:707-717.
- Lucchinetti CF, Brück W, Rodriguez M, Lassmann H (1996) Distinct patterns of multiple sclerosis pathology indicates heterogeneity on pathogenesis. *Brain pathology (Zurich, Switzerland)* 6:259-274.
- Ludwin SK, Maitland M (1984) Long-term remyelination fails to reconstitute normal thickness of central myelin sheaths. *Journal of the neurological sciences* 64:193-198.

- Lukas C, Minneboo A, Groot DV, Moraal B (2010) Early central atrophy rate predicts 5 year clinical outcome in multiple sclerosis. *Journal of neurology*.
- Lycklama G, Thompson A, Filippi M, Miller D, Polman C, Fazekas F, Barkhof F (2003) Spinal-cord MRI in multiple sclerosis. *The Lancet Neurology* 2:555-562.
- Mahad D, Lassmann H, Turnbull DC (2008a) Review: Mitochondria and disease progression in multiple sclerosis. *Neuropathology and applied neurobiology* 34:577-589.
- Mahad D, Ziabreva I, Lassmann H, Turnbull DC (2008b) Mitochondrial defects in acute multiple sclerosis lesions. *Brain : a journal of neurology* 131:1722-1735.
- Mallik S, Samson RS, Wheeler-Kingshott CA, Miller DHC (2014) Imaging outcomes for trials of remyelination in multiple sclerosis. *Journal of neurology, neurosurgery, and psychiatry* 85:1396-1404.
- Mallucci G, Peruzzotti-Jametti L, Bernstock JD, Pluchino SC (2015) The role of immune cells, glia and neurons in white and gray matter pathology in multiple sclerosis. *Progress in neurobiology* 127-128:1-22.
- Matsushima GK, Morell P (2001) The neurotoxicant, cuprizone, as a model to study demyelination and remyelination in the central nervous system. *Brain pathology (Zurich, Switzerland)* 11:107-116.
- McCreary CR, Bjarnason TA, Skihar V, Mitchell JR, Yong VW, Dunn JF (2009) Multiexponential T2 and magnetization transfer MRI of demyelination and remyelination in murine spinal cord. *NeuroImage* 45:1173-1182.
- McDonald WI, Compston A, Edan G, Goodkin D, Hartung HP, Lublin FD, McFarland HF, Paty DW, Polman CH, Reingold SC, Sandberg-Wollheim M, Sibley W, Thompson A, van den Noort S, Weinshenker BY, Wolinsky JS (2001) Recommended diagnostic criteria for multiple sclerosis: guidelines from the International Panel on the diagnosis of multiple sclerosis. *Annals of neurology* 50:121-127.
- McMahon EJ, Bailey SL, Castenada CV, Waldner H, Miller SD (2005) Epitope spreading initiates in the CNS in two mouse models of multiple sclerosis. *Nature medicine* 11:335-339.
- McRae BL, Kennedy MK, Tan LJ, Dal Canto MC, Picha KS, Miller SD (1992) Induction of active and adoptive relapsing experimental autoimmune encephalomyelitis (EAE) using an encephalitogenic epitope of proteolipid protein. *Journal of neuroimmunology* 38:229-240.
- Merrill JE (2009) In vitro and in vivo pharmacological models to assess demyelination and remyelination. *Neuropsychopharmacology : official publication of the American College of Neuropsychopharmacology* 34:55-73.
- Miller D, Barkhof F, Montalban X, Thompson A, Filippi M (2005) Clinically isolated syndromes suggestive of multiple sclerosis, part I: natural history, pathogenesis, diagnosis, and prognosis. *The Lancet Neurology* 4:281-288.

- Miron VE, Franklin RJ (2014) Macrophages and CNS remyelination. *Journal of neurochemistry* 130:165-171.
- Morrison C, Henkelman RM (1995) A model for magnetization transfer in tissues. *Magnetic resonance in medicine* 33:475-482.
- Munoz JJ, Mackay IR (1984) Production of experimental allergic encephalomyelitis with the aid of pertussigen in mouse strains considered genetically resistant. *Journal of neuroimmunology* 7:91-96.
- Munz C, Lunemann JD, Getts MT, Miller SDC (2009) Antiviral immune responses: triggers of or triggered by autoimmunity? *Nature reviews Immunology* 9:246-258.
- Murray T (2004) *Multiple sclerosis: the history of a disease*: Demos Medical Publishing.
- Murtie JC, Zhou Y-XX, Le TQ, Vana AC, Armstrong RC (2005) PDGF and FGF2 pathways regulate distinct oligodendrocyte lineage responses in experimental demyelination with spontaneous remyelination. *Neurobiology of disease* 19:171-182.
- Nair G, Tanahashi Y, Low HP, Billings-Gagliardi S, Schwartz WJ, Duong TQC (2005) Myelination and long diffusion times alter diffusion-tensor-imaging contrast in myelin-deficient shiverer mice. *NeuroImage* 28:165-174.
- Naismith RT, Xu J, Tutlam NT, Scully PT, Trinkaus K, Snyder AZ, Song SKK, Cross AC (2010) Increased diffusivity in acute multiple sclerosis lesions predicts risk of black hole. *Neurology* 74:1694-1701.
- Naismith RT, Xu J, Klawiter EC, Lancia S, Tutlam NT, Wagner JM, Qian P, Trinkaus K, Song S-KK, Cross AHC (2013) Spinal cord tract diffusion tensor imaging reveals disability substrate in demyelinating disease. *Neurology* 80:2201-2209.
- Nathoo N, Yong VW, Dunn JF (2014a) Understanding disease processes in multiple sclerosis through magnetic resonance imaging studies in animal models. *Neuroimage Clin* 4:743-756.
- Nathoo N, Yong VW, Dunn JF (2014b) Using magnetic resonance imaging in animal models to guide drug development in multiple sclerosis. *Mult Scler* 20:3-11.
- Neil JJ (2008) Diffusion imaging concepts for clinicians. *Diffusion imaging concepts for clinicians*.
- Odrobina EE, Lam TY, Pun T, Midha R, Staniszc GJ (2005) MR properties of excised neural tissue following experimentally induced demyelination. *NMR in Biomedicine* 18:277-284.
- Ontaneda D, Hyland M, Cohen JA (2012) Multiple sclerosis: new insights in pathogenesis and novel therapeutics. *Annual review of medicine* 63:389-404.
- Ou X, Sun S-WW, Liang H-FF, Song S-KK, Gochberg DFC (2009a) Quantitative magnetization transfer measured pool-size ratio reflects optic nerve myelin content in ex vivo mice. *Magnetic resonance in medicine* 61:364-371.

- Ou X, Sun S-WW, Liang H-FF, Song S-KK, Gochberg DFC (2009b) The MT pool size ratio and the DTI radial diffusivity may reflect the myelination in shiverer and control mice. *NMR in Biomedicine* 22:480-487.
- Owens GP, Gilden D, Burgoon MP, Yu X, Bennett JLC (2011) Viruses and multiple sclerosis. *The Neuroscientist : a review journal bringing neurobiology, neurology and psychiatry* 17:659-676.
- Owens T (2006) Animal models for multiple sclerosis. *Advances in neurology* 98:77-89.
- Pagani E, Bizzi A, Salle F, Stefano N, Filippi M (2008) Basic concepts of advanced MRI techniques. *Neurological Sciences* 29:290-295.
- Patrikios P, Stadelmann C, Kutzelnigg A, Rauschka H, Schmidbauer M, Laursen H, Sorensen PS, Brück W, Lucchinetti C, Lassmann H (2006) Remyelination is extensive in a subset of multiple sclerosis patients. *Brain : a journal of neurology* 129:3165-3172.
- Patwardhan MB, Matchar DB, Samsa GP, McCrory DC, Williams RG, Li TT (2005) Cost of multiple sclerosis by level of disability: a review of literature. *Multiple sclerosis (Houndmills, Basingstoke, England)* 11:232-239.
- Pierpaoli C, Barnett A, Pajevic S, Chen R, Penix LR, Virta A, Basser P (2001) Water diffusion changes in Wallerian degeneration and their dependence on white matter architecture. *NeuroImage* 13:1174-1185.
- Plewes DB, Kucharczyk W (2012) Physics of MRI: a primer. *Journal of magnetic resonance imaging : JMRI* 35:1038-1054.
- Polman CH, Reingold SC, Banwell B, Clanet M, Cohen JA, Filippi M, Fujihara K, Havrdova E, Hutchinson M, Kappos L, Lublin FD, Montalban X, O'Connor P, Sandberg-Wollheim M, Thompson AJ, Waubant E, Weinshenker B, Wolinsky JSC (2011) Diagnostic criteria for multiple sclerosis: 2010 revisions to the McDonald criteria. *Annals of neurology* 69:292-302.
- Procaccini C, De Rosa V, Pucino V, Formisano L, Matarese G (2015) Animal models of Multiple Sclerosis. *European journal of pharmacology* 759:182-191.
- Purcell EM, Torrey HC, Pound RV (1946) Resonance absorption by nuclear magnetic moments in a solid. *Physical review* 69:37.
- Quesson B, Thiébaud E, Delalande C, Dousset V, Chateil JF, Canioni P (1997) Magnetization transfer imaging in vivo of the rat brain at 4.7 T: interpretation using a binary spin-bath model with a super-Lorentzian lineshape. *Magnetic resonance in medicine* 38:974-980.
- Ramani A, Dalton C, Miller DH, Tofts PS, Barker GJ (2002) Precise estimate of fundamental in-vivo MT parameters in human brain in clinically feasible times. *Magnetic resonance imaging* 20:721-731.
- Ransohoff RM (2012) Animal models of multiple sclerosis: the good, the bad and the bottom line. *Nature neuroscience* 15:1074-1077.
- Rausch M, Tofts P, Lervik P, Walmsley A, Mir A, Schubart A, Seabrook T (2009) Characterization of white matter damage in animal models of multiple

- sclerosis by magnetization transfer ratio and quantitative mapping of the apparent bound proton fraction f. *Multiple sclerosis* (Houndmills, Basingstoke, England) 15:16-27.
- Reindl M, Linington C, Brehm U, Egg R, Dilitz E, Deisenhammer F, Poewe W, Berger T (1999) Antibodies against the myelin oligodendrocyte glycoprotein and the myelin basic protein in multiple sclerosis and other neurological diseases: a comparative study. *Brain : a journal of neurology* 122 ( Pt 11):2047-2056.
- Rivers TM, Sprunt DH, Berry GC (1933) OBSERVATIONS ON ATTEMPTS TO PRODUCE ACUTE DISSEMINATED ENCEPHALOMYELITIS IN MONKEYS. *The Journal of experimental medicine* 58:39-53.
- Samsonov A, Alexander AL, Mossahebi P, Wu Y-CC, Duncan ID, Field ASC (2012) Quantitative MR imaging of two-pool magnetization transfer model parameters in myelin mutant shaking pup. *NeuroImage* 62:1390-1398.
- Sardanelli F, Iozzelli A, Losacco C, Murialdo A, Filippi M (2003) Three subsequent single doses of gadolinium chelate for brain MR imaging in multiple sclerosis. *AJNR American journal of neuroradiology* 24:658-662.
- Scalfari A, Neuhaus A, Daumer M, Muraro PA, Ebers GC (2012) Onset of secondary progressive phase and long-term evolution of multiple sclerosis. *Journal of neurology, neurosurgery, and psychiatry* 85:67-75.
- Schmierer K, Scaravilli F, Altmann DR, Barker GJ, Miller DH (2004) Magnetization transfer ratio and myelin in postmortem multiple sclerosis brain. *Annals of neurology* 56:407-415.
- Schmierer K, Tozer DJ, Scaravilli F, Altmann DR, Barker GJ, Tofts PS, Miller DHC (2007a) Quantitative magnetization transfer imaging in postmortem multiple sclerosis brain. *Journal of magnetic resonance imaging : JMIR* 26:41-51.
- Schmierer K, Wheeler-Kingshott CA, Boulby PA, Scaravilli F, Altmann DR, Barker GJ, Tofts PS, Miller DHC (2007b) Diffusion tensor imaging of post mortem multiple sclerosis brain. *NeuroImage* 35:467-477.
- Schmierer K, Wheeler-Kingshott CA, Tozer DJ, Boulby PA, Parkes HG, Yousry TA, Scaravilli F, Barker GJ, Tofts PS, Miller DHC (2008) Quantitative magnetic resonance of postmortem multiple sclerosis brain before and after fixation. *Magnetic resonance in medicine* 59:268-277.
- Selmaj K, Raine CS, Cross AH (1991) Anti-tumor necrosis factor therapy abrogates autoimmune demyelination. *Annals of neurology* 30:694-700.
- Skipuletz T, Lindner M, Kotsiari A, Garde N, Fokuhl J, Linsmeier F, Trebst C, Stangel MC (2008) Cortical demyelination is prominent in the murine cuprizone model and is strain-dependent. *The American journal of pathology* 172:1053-1061.
- Sled JG, Pike GB (2001) Quantitative imaging of magnetization transfer exchange and relaxation properties in vivo using MRI. *Magnetic resonance in medicine* 46:923-931.

- Smith KJ (2007) Sodium channels and multiple sclerosis: roles in symptom production, damage and therapy. *Brain pathology (Zurich, Switzerland)* 17:230-242.
- Smith KJ, Blakemore WF, McDonald WI (1981) The restoration of conduction by central remyelination. *Brain : a journal of neurology* 104:383-404.
- Soares JM, Marques P, Alves V, Sousa N (2013) A hitchhiker's guide to diffusion tensor imaging. *Frontiers in Neuroscience* 7.
- Song S-KK, Sun S-WWW, Ramsbottom MJ, Chang C, Russell J, Cross AH (2002) Demyelination revealed through MRI as increased radial (but unchanged axial) diffusion of water. *NeuroImage* 17:1429-1436.
- Song S-KK, Yoshino J, Le TQ, Lin S-JJ, Sun S-WWW, Cross AH, Armstrong RC (2005) Demyelination increases radial diffusivity in corpus callosum of mouse brain. *NeuroImage* 26:132-140.
- Sospedra M, Martin R (2005a) Immunology of multiple sclerosis. *Annual review of immunology* 23:683-747.
- Sospedra M, Martin R (2005b) Antigen-specific therapies in multiple sclerosis. *International reviews of immunology* 24:393-413.
- Steinman L, Zamvil SS (2005) Virtues and pitfalls of EAE for the development of therapies for multiple sclerosis. *Trends in immunology* 26:565-571.
- Stern JN, Yaari G, Vander Heiden JA, Church G, Donahue WF, Hintzen RQ, Huttner AJ, Laman JD, Nagra RM, Nylander A, Pitt D, Ramanan S, Siddiqui BA, Vigneault F, Kleinstein SH, Hafler DA, O'Connor KCC (2013) B cells populating the multiple sclerosis brain mature in the draining cervical lymph nodes. *Science translational medicine* 6.
- Stikov N, Perry LM, Mezer A, Rykhlevskaia E, Wandell BA, Pauly JM, Dougherty RFC (2011) Bound pool fractions complement diffusion measures to describe white matter micro and macrostructure. *NeuroImage* 54:1112-1121.
- Strober LB, Arnett PA (2015) Unemployment among women with multiple sclerosis: the role of coping and perceived stress and support in the workplace. *Psychology, health & medicine*:1-9.
- Stys PK, Zamponi GW, van Minnen J, Geurts JJ (2012) Will the real multiple sclerosis please stand up? *Nature reviews Neuroscience* 13:507-514.
- Sun S-WWW, Liang H-FF, Le TQ, Armstrong RC, Cross AH, Song S-KK (2006) Differential sensitivity of in vivo and ex vivo diffusion tensor imaging to evolving optic nerve injury in mice with retinal ischemia. *NeuroImage* 32:1195-1204.
- Suzuki K (1969) Giant hepatic mitochondria: production in mice fed with cuprizone. *Science (New York, NY)* 163:81-82.
- Talbott JF, Nout-Lomas YS, Wendland MF, Mukherjee P, Huie JR, Hess CP, Mabray MC, Bresnahan JC, Beattie MS (2016) Diffusion-Weighted Magnetic Resonance Imaging Characterization of White Matter Injury

- Produced by Axon-Sparing Demyelination and Severe Contusion Spinal Cord Injury in Rats. *Journal of neurotrauma* 33:929-942.
- Temel S, KeklikoÄylu HD, KekliÄykoÄylu HD, Vural G, Deniz O, Ercan K (2013) Diffusion tensor magnetic resonance imaging in patients with multiple sclerosis and its relationship with disability. *The neuroradiology journal* 26:3-17.
- Thiessen JD, Zhang Y, Zhang H, Wang L, Buist R, Bigio MR, Kong J, Li XM, Martin M (2013) Quantitative MRI and ultrastructural examination of the cuprizone mouse model of demyelination. *NMR in Biomedicine* 26:1562-1581.
- Tillema JM, Leach J, Pirko I (2012) Non-lesional white matter changes in pediatric multiple sclerosis and monophasic demyelinating disorders. *Multiple sclerosis (Houndmills, Basingstoke, England)* 18:1754-1759.
- Tompkins SM, Padilla J, Dal Canto MC, Ting JP, Van Kaer L, Miller SD (2002) De novo central nervous system processing of myelin antigen is required for the initiation of experimental autoimmune encephalomyelitis. *Journal of immunology (Baltimore, Md : 1950)* 168:4173-4183.
- Tovi M, Ericsson A (1992) Measurements of T1 and T2 over time in formalin-fixed human whole-brain specimens. *Acta Radiologica*.
- Trapp BD, Nave K-AA (2008) Multiple sclerosis: an immune or neurodegenerative disorder? *Annual review of neuroscience* 31:247-269.
- Trapp BD, Stys PK (2009) Virtual hypoxia and chronic necrosis of demyelinated axons in multiple sclerosis. *The Lancet Neurology* 8:280-291.
- Truyen L, van Waesberghe JH, van Walderveen MA, van Oosten BW, Polman CH, Hommes OR, AdÄ`r HJ, Barkhof F (1996) Accumulation of hypointense lesions ("black holes") on T1 spin-echo MRI correlates with disease progression in multiple sclerosis. *Neurology* 47:1469-1476.
- Tsunoda I, Fujinami RSC (2010) Neuropathogenesis of Theiler's murine encephalomyelitis virus infection, an animal model for multiple sclerosis. *Journal of neuroimmune pharmacology : the official journal of the Society on NeuroImmune Pharmacology* 5:355-369.
- Tu TW, Budde MD, Xie M, Chen YJ, Wang Q (2014) Phase-aligned multiple spin-echo averaging: a simple way to improve signal-to-noise ratio of in vivo mouse spinal cord diffusion tensor image. *Magnetic resonance â€¦*.
- Tuohy VK, Lu Z, Sobel RA, Laursen RA (1989) Identification of an encephalitogenic determinant of myelin proteolipid protein for SJL mice. *The Journal of â€¦*.
- Tur C, Thompson AJ (2015) Early accurate diagnosis crucial in multiple sclerosis. *The Practitioner* 259:21.
- Turati L, Moscatelli M, Mastropietro A, Dowell NG, Zucca I, Erbetta A, Cordiglieri C, Brenna G, Bianchi B, Mantegazza R, Cercignani M, Baggi F, Minati L (2015) In vivo quantitative magnetization transfer imaging correlates with

- histology during de- and remyelination in cuprizone-treated mice. *NMR in Biomedicine* 28:327-337.
- Ulfig N, Nickel J, Bohl J (1998) Monoclonal antibodies SMI 311 and SMI 312 as tools to investigate the maturation of nerve cells and axonal patterns in human fetal brain. *Cell and tissue research*.
- van Walderveen MA, Kamphorst W, Scheltens P, van Waesberghe JH, Ravid R, Valk J, Polman CH, Barkhof F (1998) Histopathologic correlate of hypointense lesions on T1-weighted spin-echo MRI in multiple sclerosis. *Neurology* 50:1282-1288.
- Vavasour IM, Laule C, Li DK, Traboulsee AL, MacKay AL (2011) Is the magnetization transfer ratio a marker for myelin in multiple sclerosis? *Journal of magnetic resonance imaging : JMRI* 33:713-718.
- Vilanova A, Zhang S, Kindlmann G, Laidlaw D (2006) An introduction to visualization of diffusion tensor imaging and its applications: Springer.
- Wang X, Brieland JK, Kim JH, Chen Y-JJ, O'Neal J, O'Neil SP, Tu T-WW, Trinkaus K, Song S-KKC (2013) Diffusion tensor imaging detects treatment effects of FTY720 in experimental autoimmune encephalomyelitis mice. *NMR in Biomedicine* 26:1742-1750.
- Wang Y, Wang Q, Haldar JP, Yeh F-CC, Xie M, Sun P, Tu T-WW, Trinkaus K, Klein RS, Cross AH, Song S-KKC (2011) Quantification of increased cellularity during inflammatory demyelination. *Brain : a journal of neurology* 134:3590-3601.
- Waring MJ (1965) Complex formation between ethidium bromide and nucleic acids. *Journal of molecular biology* 13:269-282.
- Waxman SG (2006) Axonal conduction and injury in multiple sclerosis: the role of sodium channels. *Nature reviews Neuroscience* 7:932-941.
- Waxman SG, Ritchie JM (1993) Molecular dissection of the myelinated axon. *Annals of neurology* 33:121-136.
- Weaver A, da Silva AG, Nuttall RK, Edwards DR (2005) An elevated matrix metalloproteinase (MMP) in an animal model of multiple sclerosis is protective by affecting Th1/Th2 polarization. *The FASEB journal*.
- Werring DJ, Clark CA, Barker GJ, Thompson AJ, Miller DH (1999) Diffusion tensor imaging of lesions and normal-appearing white matter in multiple sclerosis. *Neurology* 52:1626-1632.
- Westbrook (2015) *MRI at a Glance*. John Wiley & Sons, Ltd. : Second Edition.
- Westin CF, Maier SE, Khidhir B, Everett P (1999) Image processing for diffusion tensor magnetic resonance imaging. *Proceedings of the International Conference on Medical Image Computing and Computer-Assisted Intervention*.
- Wheeler-Kingshott CA, Cercignani M (2009) About "axial" and "radial" diffusivities. *Magnetic resonance in medicine* 61:1255-1260.
- Willison HJ, Lington C (2012) Antibodies to MOG in NMO: a seasoned veteran finds a new role. *Neurology* 79:1198-1199.
- Wolansky LJ, Bardini JA, Cook SD, Zimmer AE, Sheffert A, Lee HJ (1994) Triple-dose versus single-dose gadoteridol in multiple sclerosis patients. *Journal*

- of neuroimaging : official journal of the American Society of Neuroimaging 4:141-145.
- Woodruff RH, Franklin RJ (1999) Demyelination and remyelination of the caudal cerebellar peduncle of adult rats following stereotaxic injections of lysolecithin, ethidium bromide, and complement/anti-galactocerebroside: a comparative study. *Glia* 25:216-228.
- Wucherpfennig KW, Strominger JL (1995) Molecular mimicry in T cell-mediated autoimmunity: viral peptides activate human T cell clones specific for myelin basic protein. *Cell* 80:695-705.
- Xie M, Tobin JE, Budde MD, Chen C-II, Trinkaus K, Cross AH, McDaniel DP, Song S-KK, Armstrong RCC (2010) Rostrocaudal analysis of corpus callosum demyelination and axon damage across disease stages refines diffusion tensor imaging correlations with pathological features. *Journal of neuropathology and experimental neurology* 69:704-716.
- Young IR, Hall AS, Pallis CA, Bydder GM, Legg NJ, Steiner RE (1981) Nuclear magnetic resonance imaging of the brain in multiple sclerosis. *The Lancet* 318:1063-1066.
- Zaaraoui W, Deloire M, Merle M, Girard CI, Raffard Gr, Biran M, Inglese M, Petry KG, Gonen O, Brochet B, Franconi J-MM, Dousset VC (2008) Monitoring demyelination and remyelination by magnetization transfer imaging in the mouse brain at 9.4 T. *Magma (New York, NY)* 21:357-362.
- Zhang H, Schneider T, Wheeler-Kingshott CA, Alexander DC (2012a) NODDI: Practical in vivo neurite orientation dispersion and density imaging of the human brain. *NeuroImage* 61:1000-1016.
- Zhang J, Jones MV, McMahon MT, Mori S, Calabresi PAC (2012b) In vivo and ex vivo diffusion tensor imaging of cuprizone-induced demyelination in the mouse corpus callosum. *Magnetic resonance in medicine* 67:750-759.
- Ziabreva I, Campbell G, Rist J, Zambonin J, Rorbach J, Wydro MM, Lassmann H, Franklin RJ, Mahad DC (2010) Injury and differentiation following inhibition of mitochondrial respiratory chain complex IV in rat oligodendrocytes. *Glia* 58:1827-1837.

## Appendix A: Copyright Permissions

### JOHN WILEY AND SONS LICENSE TERMS AND CONDITIONS

Feb 03, 2017

This Agreement between Raveena Dhaliwal ("You") and John Wiley and Sons ("John Wiley and Sons") consists of your license details and the terms and conditions provided by John Wiley and Sons and Copyright Clearance Center.

License Number	4038900869264
License date	Jan 30, 2017
Licensed Content Publisher	John Wiley and Sons
Licensed Content Publication	Journal of Magnetic Resonance Imaging
Licensed Content Title	Diffusion imaging concepts for clinicians
Licensed Content Author	Jeffrey J. Neil
Licensed Content Date	Nov 29, 2007
Licensed Content Pages	7
Type of use	Dissertation/Thesis
Requestor type	University/Academic
Format	Print and electronic
Portion	Figure/table
Number of figures/tables	2
Original Wiley figure/table number(s)	Figure 2, Figure 3
Will you be translating?	No
Title of your thesis / dissertation	Magnetic Resonance Imaging of Demyelination and Remyelination in the Lysolecithin Model of Multiple Sclerosis
Expected completion date	Feb 2017
Expected size (number of pages)	150
Requestor Location	Raveena Dhaliwal [REDACTED]
	[REDACTED]
	Attn: Raveena Dhaliwal
Publisher Tax ID	EU826007151
Billing Type	Invoice

Billing Address

Raveena Dhaliwal  
[REDACTED]  
[REDACTED]  
Canada  
Attn: Raveena Dhaliwal

Total

0.00 CAD

Terms and Conditions

TERMS AND CONDITIONS

This copyrighted material is owned by or exclusively licensed to John Wiley & Sons, Inc. or one of its group companies (each a "Wiley Company") or handled on behalf of a society with which a Wiley Company has exclusive publishing rights in relation to a particular work (collectively "WILEY"). By clicking "accept" in connection with completing this licensing transaction, you agree that the following terms and conditions apply to this transaction (along with the billing and payment terms and conditions established by the Copyright Clearance Center Inc., ("CCC's Billing and Payment terms and conditions"), at the time that you opened your RightsLink account (these are available at any time at <http://myaccount.copyright.com>).

Terms and Conditions

- The materials you have requested permission to reproduce or reuse (the "Wiley Materials") are protected by copyright.
- You are hereby granted a personal, non-exclusive, non-sub licensable (on a standalone basis), non-transferable, worldwide, limited license to reproduce the Wiley Materials for the purpose specified in the licensing process. This license, and any CONTENT (PDF or image file) purchased as part of your order, is for a one-time use only and limited to any maximum distribution number specified in the license. The first instance of republication or reuse granted by this license must be completed within two years of the date of the grant of this license (although copies prepared before the end date may be distributed thereafter). The Wiley Materials shall not be used in any other manner or for any other purpose, beyond what is granted in the license. Permission is granted subject to an appropriate acknowledgement given to the author, title of the material/book/journal and the publisher. You shall also duplicate the copyright notice that appears in the Wiley publication in your use of the Wiley Material. Permission is also granted on the understanding that nowhere in the text is a previously published source acknowledged for all or part of this Wiley Material. Any third party content is expressly excluded from this permission.
- With respect to the Wiley Materials, all rights are reserved. Except as expressly granted by the terms of the license, no part of the Wiley Materials may be copied, modified, adapted (except for minor reformatting required by the new Publication), translated, reproduced, transferred or distributed, in any form or by any means, and

no derivative works may be made based on the Wiley Materials without the prior permission of the respective copyright owner. For STM Signatory Publishers clearing permission under the terms of the [STM Permissions Guidelines](#) only, the terms of the license are extended to include subsequent editions and for editions in other languages, provided such editions are for the work as a whole in situ and does not involve the separate exploitation of the permitted figures or extracts, You may not alter, remove or suppress in any manner any copyright, trademark or other notices displayed by the Wiley Materials. You may not license, rent, sell, loan, lease, pledge, offer as security, transfer or assign the Wiley Materials on a stand-alone basis, or any of the rights granted to you hereunder to any other person.

- The Wiley Materials and all of the intellectual property rights therein shall at all times remain the exclusive property of John Wiley & Sons Inc, the Wiley Companies, or their respective licensors, and your interest therein is only that of having possession of and the right to reproduce the Wiley Materials pursuant to Section 2 herein during the continuance of this Agreement. You agree that you own no right, title or interest in or to the Wiley Materials or any of the intellectual property rights therein. You shall have no rights hereunder other than the license as provided for above in Section 2. No right, license or interest to any trademark, trade name, service mark or other branding ("Marks") of WILEY or its licensors is granted hereunder, and you agree that you shall not assert any such right, license or interest with respect thereto
- NEITHER WILEY NOR ITS LICENSORS MAKES ANY WARRANTY OR REPRESENTATION OF ANY KIND TO YOU OR ANY THIRD PARTY, EXPRESS, IMPLIED OR STATUTORY, WITH RESPECT TO THE MATERIALS OR THE ACCURACY OF ANY INFORMATION CONTAINED IN THE MATERIALS, INCLUDING, WITHOUT LIMITATION, ANY IMPLIED WARRANTY OF MERCHANTABILITY, ACCURACY, SATISFACTORY QUALITY, FITNESS FOR A PARTICULAR PURPOSE, USABILITY, INTEGRATION OR NON-INFRINGEMENT AND ALL SUCH WARRANTIES ARE HEREBY EXCLUDED BY WILEY AND ITS LICENSORS AND WAIVED BY YOU.
- WILEY shall have the right to terminate this Agreement immediately upon breach of this Agreement by you.
- You shall indemnify, defend and hold harmless WILEY, its Licensors and their respective directors, officers, agents and employees, from and against any actual or threatened claims, demands, causes of action or proceedings arising from any breach of this Agreement by you.
- IN NO EVENT SHALL WILEY OR ITS LICENSORS BE LIABLE TO YOU OR

ANY OTHER PARTY OR ANY OTHER PERSON OR ENTITY FOR ANY SPECIAL, CONSEQUENTIAL, INCIDENTAL, INDIRECT, EXEMPLARY OR PUNITIVE DAMAGES, HOWEVER CAUSED, ARISING OUT OF OR IN CONNECTION WITH THE DOWNLOADING, PROVISIONING, VIEWING OR USE OF THE MATERIALS REGARDLESS OF THE FORM OF ACTION, WHETHER FOR BREACH OF CONTRACT, BREACH OF WARRANTY, TORT, NEGLIGENCE, INFRINGEMENT OR OTHERWISE (INCLUDING, WITHOUT LIMITATION, DAMAGES BASED ON LOSS OF PROFITS, DATA, FILES, USE, BUSINESS OPPORTUNITY OR CLAIMS OF THIRD PARTIES), AND WHETHER OR NOT THE PARTY HAS BEEN ADVISED OF THE POSSIBILITY OF SUCH DAMAGES. THIS LIMITATION SHALL APPLY NOTWITHSTANDING ANY FAILURE OF ESSENTIAL PURPOSE OF ANY LIMITED REMEDY PROVIDED HEREIN.

- Should any provision of this Agreement be held by a court of competent jurisdiction to be illegal, invalid, or unenforceable, that provision shall be deemed amended to achieve as nearly as possible the same economic effect as the original provision, and the legality, validity and enforceability of the remaining provisions of this Agreement shall not be affected or impaired thereby.
- The failure of either party to enforce any term or condition of this Agreement shall not constitute a waiver of either party's right to enforce each and every term and condition of this Agreement. No breach under this agreement shall be deemed waived or excused by either party unless such waiver or consent is in writing signed by the party granting such waiver or consent. The waiver by or consent of a party to a breach of any provision of this Agreement shall not operate or be construed as a waiver of or consent to any other or subsequent breach by such other party.
- This Agreement may not be assigned (including by operation of law or otherwise) by you without WILEY's prior written consent.
- Any fee required for this permission shall be non-refundable after thirty (30) days from receipt by the CCC.
- These terms and conditions together with CCC's Billing and Payment terms and conditions (which are incorporated herein) form the entire agreement between you and WILEY concerning this licensing transaction and (in the absence of fraud) supersedes all prior agreements and representations of the parties, oral or written. This Agreement may not be amended except in writing signed by both parties. This

Agreement shall be binding upon and inure to the benefit of the parties' successors, legal representatives, and authorized assigns.

- In the event of any conflict between your obligations established by these terms and conditions and those established by CCC's Billing and Payment terms and conditions, these terms and conditions shall prevail.
- WILEY expressly reserves all rights not specifically granted in the combination of (i) the license details provided by you and accepted in the course of this licensing transaction, (ii) these terms and conditions and (iii) CCC's Billing and Payment terms and conditions.
- This Agreement will be void if the Type of Use, Format, Circulation, or Requestor Type was misrepresented during the licensing process.
- This Agreement shall be governed by and construed in accordance with the laws of the State of New York, USA, without regards to such state's conflict of law rules. Any legal action, suit or proceeding arising out of or relating to these Terms and Conditions or the breach thereof shall be instituted in a court of competent jurisdiction in New York County in the State of New York in the United States of America and each party hereby consents and submits to the personal jurisdiction of such court, waives any objection to venue in such court and consents to service of process by registered or certified mail, return receipt requested, at the last known address of such party.

## WILEY OPEN ACCESS TERMS AND CONDITIONS

Wiley Publishes Open Access Articles in fully Open Access Journals and in Subscription journals offering Online Open. Although most of the fully Open Access journals publish open access articles under the terms of the Creative Commons Attribution (CC BY) License only, the subscription journals and a few of the Open Access Journals offer a choice of Creative Commons Licenses. The license type is clearly identified on the article.

The Creative Commons Attribution License

The [Creative Commons Attribution License \(CC-BY\)](#) allows users to copy, distribute and transmit an article, adapt the article and make commercial use of the article. The CC-BY license permits commercial and non-

Creative Commons Attribution Non-Commercial License

The [Creative Commons Attribution Non-Commercial \(CC-BY-NC\)License](#) permits use, distribution and reproduction in any medium, provided the original work is properly cited and is not used for commercial purposes.(see below)

Creative Commons Attribution-Non-Commercial-NoDerivs License

The [Creative Commons Attribution Non-Commercial-NoDerivs License](#) (CC-BY-NC-ND) permits use, distribution and reproduction in any medium, provided

the original work is properly cited, is not used for commercial purposes and no modifications or adaptations are made. (see below)  
Use by commercial "for-profit" organizations  
Use of Wiley Open Access articles for commercial, promotional, or marketing purposes requires further explicit permission from Wiley and will be subject to a fee. Further details can be found on Wiley Online Library

<http://olabout.wiley.com/WileyCDA/Section/id-410895.html> Other Terms and

Conditions: v1.10 Last updated September 2015

Questions? [customercare@copyright.com](mailto:customercare@copyright.com) or +1-855-239-3415 (toll free in the US) or +1-978-646-2777.

---

---

JOHN WILEY AND SONS LICENSE  
TERMS AND CONDITIONS

Feb 03, 2017

---

---

This Agreement between Raveena Dhaliwal ("You") and John Wiley and Sons ("John Wiley and Sons") consists of your license details and the terms and conditions provided by John Wiley and Sons and Copyright Clearance Center.

License Number	4038900545475
License date	Jan 30, 2017
Licensed Content Publisher	John Wiley and Sons
Licensed Content Publication	Magnetic Resonance in Medicine
Licensed Content Title	Quantitative interpretation of magnetization transfer
Licensed Content Author	R. Mark Henkelman, Xuemei Huang, Qing-San Xiang, G. J. Stanisz, Scott D. Swanson, Michael J. Bronskill
Licensed Content Date	Jun 1, 1993
Licensed Content Pages	8
Type of use	Dissertation/Thesis
Requestor type	University/Academic
Format	Print and electronic
Portion	Figure/table
Number of figures/tables	1

Original Wiley figure/table number(s)	Figure 3
Will you be translating?	No
Title of your thesis / dissertation	Magnetic Resonance Imaging of Demyelination and Remyelination in the Lysolecithin Model of Multiple Sclerosis
Expected completion date	Feb 2017
Expected size (number of pages)	150
Requestor Location	Raveena Dhaliwal [REDACTED] [REDACTED] Canada Attn: Raveena Dhaliwal
Publisher Tax ID	EU826007151
Billing Type	Invoice
Billing Address	Raveena Dhaliwal [REDACTED] [REDACTED] Canada Attn: Raveena Dhaliwal
Total	0.00 CAD
Terms and Conditions	

#### TERMS AND CONDITIONS

This copyrighted material is owned by or exclusively licensed to John Wiley & Sons, Inc. or one of its group companies (each a "Wiley Company") or handled on behalf of a society with which a Wiley Company has exclusive publishing rights in relation to a particular work (collectively "WILEY"). By clicking "accept" in connection with completing this licensing transaction, you agree that the following terms and conditions apply to this transaction (along with the billing and payment terms and conditions established by the Copyright Clearance Center Inc., ("CCC's Billing and Payment terms and conditions"), at the time that you opened your RightsLink account (these are available at any time at <http://myaccount.copyright.com>).

#### Terms and Conditions

- The materials you have requested permission to reproduce or reuse (the "Wiley Materials") are protected by copyright.
- You are hereby granted a personal, non-exclusive, non-sub licensable (on a standalone basis), non-transferable, worldwide, limited license to reproduce the Wiley Materials for the purpose specified in the licensing process. This license, and

any CONTENT (PDF or image file) purchased as part of your order, is for a one-time use only and limited to any maximum distribution number specified in the license. The first instance of republication or reuse granted by this license must be completed within two years of the date of the grant of this license (although copies prepared before the end date may be distributed thereafter). The Wiley Materials shall not be used in any other manner or for any other purpose, beyond what is granted in the license. Permission is granted subject to an appropriate acknowledgement given to the author, title of the material/book/journal and the publisher. You shall also duplicate the copyright notice that appears in the Wiley publication in your use of the Wiley Material. Permission is also granted on the understanding that nowhere in the text is a previously published source acknowledged for all or part of this Wiley Material. Any third party content is expressly excluded from this permission.

- With respect to the Wiley Materials, all rights are reserved. Except as expressly granted by the terms of the license, no part of the Wiley Materials may be copied, modified, adapted (except for minor reformatting required by the new Publication), translated, reproduced, transferred or distributed, in any form or by any means, and no derivative works may be made based on the Wiley Materials without the prior permission of the respective copyright owner. For STM Signatory Publishers clearing permission under the terms of the [STM Permissions Guidelines](#) only, the terms of the license are extended to include subsequent editions and for editions in other languages, provided such editions are for the work as a whole in situ and does not involve the separate exploitation of the permitted figures or extracts, You may not alter, remove or suppress in any manner any copyright, trademark or other notices displayed by the Wiley Materials. You may not license, rent, sell, loan, lease, pledge, offer as security, transfer or assign the Wiley Materials on a stand-alone basis, or any of the rights granted to you hereunder to any other person.
- The Wiley Materials and all of the intellectual property rights therein shall at all times remain the exclusive property of John Wiley & Sons Inc, the Wiley Companies, or their respective licensors, and your interest therein is only that of having possession of and the right to reproduce the Wiley Materials pursuant to Section 2 herein during the continuance of this Agreement. You agree that you own no right, title or interest in or to the Wiley Materials or any of the intellectual property rights therein. You shall have no rights hereunder other than the license as provided for above in Section 2. No right, license or interest to any trademark, trade name, service mark or other branding ("Marks") of WILEY or its licensors is granted hereunder, and you agree that you shall not assert any such right, license or interest with respect thereto
- **NEITHER WILEY NOR ITS LICENSORS MAKES ANY WARRANTY OR REPRESENTATION OF ANY KIND TO YOU OR ANY THIRD PARTY, EXPRESS, IMPLIED OR STATUTORY, WITH RESPECT TO THE MATERIALS OR THE ACCURACY OF ANY INFORMATION CONTAINED IN THE**

MATERIALS, INCLUDING, WITHOUT LIMITATION, ANY IMPLIED WARRANTY OF MERCHANTABILITY, ACCURACY, SATISFACTORY QUALITY, FITNESS FOR A PARTICULAR PURPOSE, USABILITY, INTEGRATION OR NON-INFRINGEMENT AND ALL SUCH WARRANTIES ARE HEREBY EXCLUDED BY WILEY AND ITS LICENSORS AND WAIVED BY YOU.

- WILEY shall have the right to terminate this Agreement immediately upon breach of this Agreement by you.
- You shall indemnify, defend and hold harmless WILEY, its Licensors and their respective directors, officers, agents and employees, from and against any actual or threatened claims, demands, causes of action or proceedings arising from any breach of this Agreement by you.
- IN NO EVENT SHALL WILEY OR ITS LICENSORS BE LIABLE TO YOU OR ANY OTHER PARTY OR ANY OTHER PERSON OR ENTITY FOR ANY SPECIAL, CONSEQUENTIAL, INCIDENTAL, INDIRECT, EXEMPLARY OR PUNITIVE DAMAGES, HOWEVER CAUSED, ARISING OUT OF OR IN CONNECTION WITH THE DOWNLOADING, PROVISIONING, VIEWING OR USE OF THE MATERIALS REGARDLESS OF THE FORM OF ACTION, WHETHER FOR BREACH OF CONTRACT, BREACH OF WARRANTY, TORT, NEGLIGENCE, INFRINGEMENT OR OTHERWISE (INCLUDING, WITHOUT LIMITATION, DAMAGES BASED ON LOSS OF PROFITS, DATA, FILES, USE, BUSINESS OPPORTUNITY OR CLAIMS OF THIRD PARTIES), AND WHETHER OR NOT THE PARTY HAS BEEN ADVISED OF THE POSSIBILITY OF SUCH DAMAGES. THIS LIMITATION SHALL APPLY NOTWITHSTANDING ANY FAILURE OF ESSENTIAL PURPOSE OF ANY LIMITED REMEDY PROVIDED HEREIN.
- Should any provision of this Agreement be held by a court of competent jurisdiction to be illegal, invalid, or unenforceable, that provision shall be deemed amended to achieve as nearly as possible the same economic effect as the original provision, and the legality, validity and enforceability of the remaining provisions of this Agreement shall not be affected or impaired thereby.
- The failure of either party to enforce any term or condition of this Agreement shall not constitute a waiver of either party's right to enforce each and every term and condition of this Agreement. No breach under this agreement shall be deemed waived or excused by either party unless such waiver or consent is in writing signed by the party granting such waiver or consent. The waiver by or consent of a party to a breach of any provision of this Agreement shall not operate or be

construed as a waiver of or consent to any other or subsequent breach by such other party.

- This Agreement may not be assigned (including by operation of law or otherwise) by you without WILEY's prior written consent.
- Any fee required for this permission shall be non-refundable after thirty (30) days from receipt by the CCC.
- These terms and conditions together with CCC's Billing and Payment terms and conditions (which are incorporated herein) form the entire agreement between you and WILEY concerning this licensing transaction and (in the absence of fraud) supersedes all prior agreements and representations of the parties, oral or written. This Agreement may not be amended except in writing signed by both parties. This Agreement shall be binding upon and inure to the benefit of the parties' successors, legal representatives, and authorized assigns.
- In the event of any conflict between your obligations established by these terms and conditions and those established by CCC's Billing and Payment terms and conditions, these terms and conditions shall prevail.
- WILEY expressly reserves all rights not specifically granted in the combination of (i) the license details provided by you and accepted in the course of this licensing transaction, (ii) these terms and conditions and (iii) CCC's Billing and Payment terms and conditions.
- This Agreement will be void if the Type of Use, Format, Circulation, or Requestor Type was misrepresented during the licensing process.
- This Agreement shall be governed by and construed in accordance with the laws of the State of New York, USA, without regards to such state's conflict of law rules. Any legal action, suit or proceeding arising out of or relating to these Terms and Conditions or the breach thereof shall be instituted in a court of competent jurisdiction in New York County in the State of New York in the United States of America and each party hereby consents and submits to the personal jurisdiction of such court, waives any objection to venue in such court and consents to service of process by registered or certified mail, return receipt requested, at the last known address of such party.

## WILEY OPEN ACCESS TERMS AND CONDITIONS

Wiley Publishes Open Access Articles in fully Open Access Journals and in Subscription journals offering Online Open. Although most of the fully Open Access journals publish open access articles under the terms of the Creative Commons Attribution (CC BY) License only, the subscription journals and a few of the Open Access Journals offer a choice of Creative Commons Licenses. The license type is clearly identified on the article.

The Creative Commons Attribution License

The [Creative Commons Attribution License \(CC-BY\)](#) allows users to copy, distribute and transmit an article, adapt the article and make commercial use of the article. The CC-BY license permits commercial and non-

Creative Commons Attribution Non-Commercial License

The [Creative Commons Attribution Non-Commercial \(CC-BY-NC\)License](#) permits use, distribution and reproduction in any medium, provided the original work is properly cited and is not used for commercial purposes.(see below)

Creative Commons Attribution-Non-Commercial-NoDerivs License

The [Creative Commons Attribution Non-Commercial-NoDerivs License](#) (CC-BY-NC-ND) permits use, distribution and reproduction in any medium, provided the original work is properly cited, is not used for commercial purposes and no modifications or adaptations are made. (see below)

Use by commercial "for-profit" organizations

Use of Wiley Open Access articles for commercial, promotional, or marketing

purposes requires further explicit permission from Wiley and will be subject to a

fee. Further details can be found on Wiley Online Library

<http://olabout.wiley.com/WileyCDA/Section/id-410895.html> Other Terms and

Conditions: v1.10 Last updated September 2015

Questions? [customercare@copyright.com](mailto:customercare@copyright.com) or +1-855-239-3415 (toll free in the US) or +1-978-646-2777.